

NORTHWESTERN UNIVERSITY

Shape, Thermodynamics, Kinetics and Growth Mechanisms of Metal and Bimetallic  
Nanoparticles

A DISSERTATION

SUBMITTED TO THE GRADUATE SCHOOL  
IN PARTIAL FULFILLMENT OF THE REQUIREMENTS

for the degree

DOCTOR OF PHILOSOPHY

Field of Materials Science and Engineering

By

Lingxuan Peng

EVANSTON, ILLINOIS

June 2017

© Copyright by Lingxuan Peng 2017

All Rights Reserved

## ABSTRACT

### Shape, Thermodynamics, Kinetics and Growth Mechanisms of Metal and Bimetallic Nanoparticles

Lingxuan Peng

Metal and bimetallic nanoparticles are of interest and are widely used in various applications because of their unique optical, electronic, and catalytic properties, which differ from those of their bulk counterparts. Better understanding of the thermodynamic and kinetic properties of nanoparticles and their underlying growth mechanisms can serve as a basis for improving reproducibility and rational design of nanoparticle syntheses. The primary objective of this dissertation was to study the structural-related thermodynamic and kinetic properties of nanoparticles via the combination of experimental and theoretical techniques and to further unravel their underlying growth mechanisms.

In this dissertation, the structure and elemental distribution of colloiddally-synthesized bimetallic nanoparticles were characterized via scanning/transmission electron microscopy (S/TEM) and energy dispersive X-ray spectroscopy (EDX). In colloiddally-synthesized bimetallic Pt/Pd nanoparticles, smooth composition gradients from the particle centers to their surfaces and corner enrichment of Pt were observed experimentally. A growth model was developed to demonstrate that the smooth composition gradients within the particles were the result of the difference in the deposition rate constants of Pd and Pt, causing Pd to deposit faster than Pt. The deposition rate constant ratio between Pd and Pt increased with total Pd and Pt precursor concentration. The corner Pt enrichment was a result of local thermodynamic control at the corners. At the nanoparticle corner, a Lyapunov stable solution could be achieved when the chemical

potential at the corner equals the external chemical potential in the solution. This stable solution leads to size-independent corner rounding in colloidal synthesized nanoparticles.

Strain-induced segregation in bimetallic multiply twinned particles, namely decahedral (Dh) and icosahedral (Ic) particles, was analyzed by an analytic first-order expansion within a continuum model. The results indicated that there was a noticeable segregation of larger atoms to the external surface and the smaller ones to the core, despite a small change in free energy due to segregation. Segregation was found to be more significant in Ic particles compared to Dh particles and at lower temperatures.

The formation of symmetric versus asymmetric particles was also studied to compare their thermodynamic stability. Asymmetric re-entrant decahedral (Dh) particles with mirror planes were synthesized under different conditions. The thermodynamic stability of these particles was analyzed by calculating the total energy of Dh particles at different sizes, and results showed that the nanoparticle size could influence the thermodynamic stable shapes, and the five-fold symmetric Dh shape was no longer the thermodynamic stable structure at bigger sizes.

Beyond electron microscopy, a wide-field dark-field optical microscope was used to measure the diffusion and growth of single plasmonic nanoparticles. The LSPR spectra and diffusion trajectories of particles were obtained simultaneously via an ultra-thin liquid cell. This cell was designed to confine particle movements in 2-D within the depth of field of the objective lens during growth. Being able to monitor changes in both the spectra and diffusion coefficients *in situ* during reaction will open a new avenue for understanding the nanoparticle growth mechanisms.

Approved by

Professor Laurence D. Marks

Department of Materials Science and Engineering

Northwestern University, Evanston, IL 60208, U.S.A

## Acknowledgement

First of all, I would like to thank my advisors, Laurence Marks and Richard Van Duyne. Without their support, guidance and encouragement throughout the years, this dissertation would not be possible. I want to thank Laurie, always being curious and rigorous, for sharing a tremendous amount of knowledge with me. He also taught me that “*the scientist is not a person who gives the right answers, he’s the one who asks the right questions*”, by constantly asking me the right questions, and pushing me to think through the hard problems. He has also been very patient and supportive, and provided me so much freedom to propose and work on the projects I am interested in. I want to thank Rick, being so knowledgeable and approachable, for significantly broadening my vision in science. With Rick’s help, I not only look at problems on the materials science point of view, I also have become a chemist. I also would like to thank my thesis defense committees, Professor Justin Notestein, Professor Kenneth Poepplmeier and Professor Peter Voorhees, and my qualifier committee, Professor Monica Olvera de la Cruz for their valuable time and discussions.

I am very grateful to my collaborators for their help in my Ph.D studies. First, I would like to thank my mentor Dr. Emilie Ringe for teaching me how to do colloidal synthesis and being patient to answer my questions about nanoparticles and plasmonics. I also want to thank Dr. Fernanda Cardinal for working with me on the WF2 projects in the past five years and teaching me so much about nanoparticle synthesis. I would like to thank Jennifer Park for working with me on the *in situ* Au nanorods project during the last few months of my Ph.D. I would also like to thank Jon for his “magic” hands to fix the femto-second laser or any related problems with the optical set-up. I need to thank Alan for teaching me how to use the aberration-corrected STEM at

UIC. I also want to thank Dr. Sicelo Masango for providing all his Ag ALD samples to me for structure characterization and sharing a great amount of knowledge about ALD with me.

I cannot forget the wonderful personnel at the NUANCE center, especially Dr. Jinsong Wu and Dr. Shuyou Li. They provided me the first hands-on lessons on how to use TEM. I appreciate them for their time and help whenever I had questions or problems about using TEM. Particularly, I would like to thank Shuyou for being so patient to pick up all my Saturday morning phone calls about TEM in my first year. I would also like to thank Ben Myers and Karl Hagglund's help on using the FIB, and Eric Roth for teaching me how to do the negative staining of biological samples. I also need to acknowledge the staff at the Department of Materials Science and Engineering, especially to Jeannine and Gail, who were always willing to help.

I must also thank all the previous and current members from Marks and Van Duyne group, for their friendship, interesting discussions and countless crazy food parties. Special thanks go to: Emilie for being my mentor in my first year; Yuyuan for giving me the first hands-on lesson on HREM and coma-free alignment; Fernanda for constant help on WF2 and nanoparticle synthesis; Ahmet for showing me how to use the ARM properly, and for so many interesting discussions about science, history, and soccer; Yifeng, Chuandao, Pratik, Lawrence, Tiffany, Chris for listening and sharing, and being great fun.

I am also thankful for the many friends who have helped me through this: Lin, Yi, Nari, Xiaomi, Sicelo, Fer, Xueying, Li, Jian, Tiffany, Victor, Yujin, Ankun, Zixuan, Ze, Jennifer, Xiaohan, Ting, Sean and everyone else who I have left out. With you guys, the good times are better, and the bad times aren't so bad.

At the end, I need to thank my parents for all their support throughout the years. They are always caring, listening, and encouraging me to do whatever I find meaningful in my life.

## List of Abbreviations

ABF	Annular Bright Field
ADF	Annular Dark Field
ALD	Atomic Layer Deposition
BF	Bright Field
BSPP	Bis(p-sulfonatophenyl) phenylphosphine dehydrate dipotassium salt
DF	Dark Field
EDX	Energy Dispersive X-ray Spectroscopy
FCC	Face-centered Cubic
FIB	Focused Ion Beam
HAADF	High-angle Annular Dark Field
HREM	High Resolution Electron Microscopy
ITO	Indium Tin Oxide
LAADF	Low-angle Annular Dark Field
LSPR	Localized Surface Plasmon Resonance
MPS	3-Mercaptopropyltrimethoxysilane
MTP	Multiply Twinned Particle
NA	Numerical Aperture
PVP	poly(vinyl pyrrolidone)
SEM	Scanning Electron Microscope/Microscopy
SRPM	Super Resolution Plasmon Microscopy
STEM	Scanning Transmission Electron Microscope/Microscopy

TEM            Transmission Electron Microscope/Microscopy

WF            Wide-field

## Table of Contents

<b>ABSTRACT</b> .....	3
<b>Acknowledgement</b> .....	6
<b>List of Abbreviations</b> .....	9
<b>List of Figures</b> .....	16
<b>Chapter 1: Introduction</b> .....	24
1.1 Motivation .....	25
1.2 Organization .....	28
<b>Chapter 2: Background</b> .....	30
2.1 Thermodynamic and Kinetic Shapes .....	31
2.2 Minimum Energy Solutions .....	34
2.2.1 Wulff Construction for Single Crystals .....	34
2.2.2 Winterbottom Construction .....	35
2.2.3 Modified Wulff Construction for Multiply Twinned Particles .....	36
2.3 Kinetic Shapes .....	39
2.3.1 Kinetic Wulff Construction .....	43
2.3.2 Kinetic Enhancement at Certain Sites .....	44

	12
2.3.3 Convex Shapes .....	45
2.3.4 Symmetry Breaking, Corner Rounding and Relationship with Segregation .....	46
2.4 Mixed Growth .....	47
2.5 Strain Relaxation in MTPs .....	48
2.6 Segregation in Bimetallic Nanoparticles .....	51
2.6.1 Analytical Models.....	52
2.6.2 Numerical Methods .....	54
2.6.3 Thermodynamics vs. Kinetics .....	55
<b>Chapter 3: Experimental Methods.....</b>	<b>56</b>
3.1 Introduction .....	57
3.2 Synthesis of Metal and Bimetallic Nanoparticles .....	57
3.3 Electron Microscopy .....	58
3.3.1 TEM Basics .....	58
3.3.2 Energy Dispersive X-ray Spectroscopy.....	61
3.3.3 Nanoparticle TEM Sample Preparation.....	62
3.4 UV-vis Spectroscopy.....	63
3.5 Wide-field Dark Field Optical Microscopy .....	64
3.5.1 <i>In situ</i> Monitoring of Diffusional Particle Growth.....	69
3.5.2 <i>In situ</i> Monitoring of Stationary Particle Growth.....	71

## **Chapter 4: Compositional Gradient and Corner Enrichment of Pt in Pt/Pd**

<b>Bimetallic Nanoparticles .....</b>	<b>73</b>
4.1 Introduction .....	74
4.2 Methods .....	75
4.3 Results .....	76
4.3.1 Model for Radial Concentration Change .....	79
4.3.2 Corner Rounding .....	87
4.3.3 Model for Pt Enhancement at the Corners.....	96
4.4 Discussion .....	98
4.5 Conclusion.....	100

## **Chapter 5: Thermodynamic Stability of Asymmetric Decahedral**

<b>Nanoparticles.....</b>	<b>101</b>
5.1 Introduction .....	102
5.2 Methods .....	104
5.2.1 Synthesis of Pt/Pd Bimetallic Nanoparticles .....	104
5.2.2 Synthesis of Pd Dh Nanoparticle .....	105
5.2.3 Finite Element Analysis.....	106
5.3 Determination of Re-entrant levels .....	106
5.4 Bulk-surface Energy Balance.....	108

	14
5.5 Finite Element Methods .....	109
5.6 Results .....	111
5.7 Conclusion.....	115
5.8 Future Work .....	115
<b>Chapter 6: Strain-induced Segregation in Bimetallic Multiply Twinned</b>	
<b>Particles .....</b>	<b>117</b>
6.1 Introduction .....	118
6.2 Derivation of Strain-induced Segregation.....	119
6.2.1 Inhomogeneous Strains in Decahedra and Icosahedra .....	119
6.2.2 Change in Energy .....	120
6.2.3 Derivation of Composition Distribution.....	122
6.3 Temperature-dependent Segregation.....	125
6.4 Degree of Segregation.....	129
6.5 Discussion .....	130
6.6 Conclusion.....	132
<b>Chapter 7: Wide-field Super Resolution Plasmon Microscopy.....</b>	
7.1 Introduction .....	134
7.2 Methods.....	136
7.2.1 Synthesis of Ag Nanoprism.....	136

	15
7.2.2 Synthesis of Au Nanorod.....	136
7.2.3 Ultra-thin Liquid Cell.....	137
7.2.4 SEM-correlated Study of Ag nanoprism growth.....	138
7.3 Experimental Results.....	139
7.3.1 Spectra and Diffusion Trajectories of Au nanospheres .....	139
7.3.2 Time-dependent Study of Au Nanorod Growth .....	140
7.3.3 Time-dependent Study of Ag Nanoprism Growth .....	143
7.3.4 Morphology Change from AgO Reduction .....	148
7.4 Different Light Source .....	150
7.5 Future Work .....	151
7.6 Video Captions.....	154
<b>Chapter 8: Conclusions and Future Directions .....</b>	<b>155</b>
8.1 Conclusions .....	156
8.2 Future Work .....	159
<b>Reference.....</b>	<b>164</b>
<b>Appendix A .....</b>	<b>179</b>

## List of Figures

- Figure 1.1 Histogram of number of publications per year, which contain only ‘nanoparticle’ as a key word are labeled in blue, and the ones also have ‘shape’ as a keyword is shown in yellow and the ones that also have ‘thermodynamics’ as a keyword are in red. .... 26
- Figure 1.2 Most commonly observed nanoparticle shapes are divided into two cases, ones which can occur from thermodynamic control and ones which are only from kinetic control. They are split into the three broad categories of Single Crystals, Lamellar Twinned particles and Multiply Twinned Particles. Every thermodynamic shape can also arise from kinetics, but the converse is not true. The facets are color coded, yellow for {111}, green for {100} blue for {110} and red for higher index..... 27
- Figure 2.1 Illustration of the equimolar cut for surfaces in terms of the Wigner-Seitz unit cells 32
- Figure 2.2 Schematic of the variation in shape of a nanoparticle, here with a (100) epitaxy on the substrate, as a function of the interfacial free energy. From left to right is the analogue of dewetting to wetting for a solid single crystal particle ..... 35
- Figure 2.3 Illustration of the modified Wulff construction. For the three-dimensional Wulff shape shown on the left in (a) the region between two twin planes (red) is extracted. Five of these joined at the twin boundaries leads to the Dh shape shown on the right in (b), with the re-entrant {111} surfaces in yellow. {100} faces are green in both (a) and (b)..... 36
- Figure 2.4 Schematics and TEM images of MTPs. (a) – (c) Schematics for (a) LTP with two parallel twin boundaries (b) Marks decahedral MTP and (c) Icosahedral MTP. (d) – (f) TEM images for (d) LTP with multiple parallel twin boundaries, (e) Marks Dh and (f) Ic. .... 38
- Figure 2.5 Different cases for Dh in three columns (a)-(c) with different ratios of the {111} and {100} surface energies. Shown at the top is the single segment, below the particle down the common [011] direction and below from the side. Experimental images are shown below ..... 39

Figure 2.6 Schematic of the relevant regions for kinetic growth. Region III contains a nucleating terrace, Region II atoms that can diffuse to the terrace and Region I external atoms. Atoms are represented by cubes which are color coded by region, with the substrate yellow, and ligands near the surface are illustrated .....	40
Figure 2.7 Energy versus size for a growing terrace, the blue curves corresponds to a full two-dimensional terrace as a circular disc and the orange curve corresponds to a half disc at a re-entrant twin boundary. The activation energy barrier at a re-entrant twin boundary is substantially lower than that of the flat surface case .....	43
Figure 2.8 Explanation of enhanced growth at a re-entrant twin. The atoms in a terrace that terminates at the twin place can bond to those on the other side, so the effective line energy is almost zero .....	45
Figure 2.9 Relative populations of different MTPs indicating a transition from perfect Dh to Marks Dh from decreasing the PVP concentration.....	48
Figure 3.1 Schematic of the electron-specimen interaction.....	59
Figure 3.2 Applications of transmission electron microscopy (TEM): (a) Conventional TEM image of Ag nanoprisms (b) HRTEM image of GaAlAs/GaAs nanowires (c) HR-HAADF-STEM image of anatase TiO <sub>2</sub> supported Ta single atom catalyst (d) HAADF image of mesoporous SiO <sub>2</sub> supported Ag nanoparticles (e) electron diffraction pattern of a penta-twinned Au nanowire (f) secondary electron image of Pt/Pd bimetallic multiply twinned particles .....	61
Figure 3.3 (a) Dark field microscopy setup. The transmitted light does go into the objective lens, but is blocked by the aperture. The yellow light in the diagram is exaggerated, but it emphasizes that only the scattered light is collected by the objective, and (b) picture of the apparatus. ....	65
Figure 3.4 (a) Diagram of the WF set-up. An inverted microscope coupled with a colored CCD and EMCCD. A set of acousto-optical tunable filters are installed to allow one wavelength to reach the EMCCD at a time. (b) picture of the apparatus.....	66

- Figure 3.5 The GUI window made by the MATLAB code. (a) The input parameters include the starting wavelength, wavelength step and the time step of the data, and (b) shows the procedure of particle spectra generation ..... 68
- Figure 3.6 (a) One sample frame out of the 100 frames acquired by EMCCD. (b) LSPR spectra of three particles labeled in (a), and (c) the corresponding mean square displacements of these three particles ..... 69
- Figure 3.7 Schematic of the thin liquid cell ..... 70
- Figure 3.8 (a) Design of the liquid flow cell and (b) the picture of the assembled cell. Photo courtesy by Meaghan Bruening ..... 72
- Figure 4.1 TEM and HAADF images of Pt/Pd multiply twinned particles made by 1:1 molar ratio of Pd and Pt precursors ..... 77
- Figure 4.2 Measured composition profiles and calculated 2D projections as a function of distance from the center to the surface of particles. (a) The composition profile of a Dh fitted with different  $r_{Pd}(T)/r_{Pt}(T)$  ratios; (a) and (b) are composition profiles of a particle synthesized with a 1:1 molar ratio of Pd and Pt precursors. (b) Composition profile of a particle synthesized with a double amount of Pd. (e) Composition profile of a particle synthesized with a double amount of Pt. The composition profiles of particles in (b) and (e) have the same  $r_{Pd}(T)/r_{Pt}(T)$  ratio. (c) Composition profile of a particle synthesized with half of the amount of Pd. (f) Composition profile of a particle synthesized with half of the amount of Pt. The composition profiles of particles in (c) and (f) have the same  $r_{Pd}(T)/r_{Pt}(T)$  ratio..... 78
- Figure 4.3 EDX measurements showing the surface and corner enrichment of Pt in Pt/Pd bimetallic nanoparticles. (a) The EDX elemental maps of the Pd/Pt multiply twinned particles. (b) A EDX line scan from the corner to the center of a particle (c) A EDX line scan between two corners of the sample particle. .... 78

Figure 4.4 Schematics of nanoparticle formation. (a) The regions for kinetic growth. Region I contains external Pt and Pd atoms that are reduced by PVP. Region II is the region where Pt and Pd atoms diffuse to the terrace and region III is a nucleating terrace. (b) Schematic explaining the origin of the concentration gradient. The Pd atoms attach to the surface faster than that of Pt atoms. As growth proceeds, Pd atoms are consumed faster than Pt atoms and more Pd is deposited near the surface of the particles. .... 81

Figure 4.5  $r_{Pd}(T)/r_{Pt}(T)$  as a function of the total amount of Pd and Pt precursor concentration.. 85

Figure 4.6 Pt concentration profiles as a function of distance from the center to the surface (0 represents the center of the particle, and 1 represents the surface of the particle), calculated with different incubation steps ..... 86

Figure 4.7 Pt concentration profiles as a function of distance from the center to the surface (0 represents the center of the particle, and 1 represents the surface of the particle) calculated with different ratios between deposition and reduction rate constant  $r_{Pd}/k_{Pd}$ ..... 87

Figure 4.8 (a) Illustration of truncation of a (001) facet for different numbers of planes (N) to take account of atomicity, with the corresponding equimolar surfaces and facet length shown.  $L_i$  is the distance normal to the facet from the Wulff center to the apex, while  $h_i$  is the distance from the Wulff center to the facet shown for  $N=2$ . (b) The chemical potential in eV/atom vs.  $1/N$ , calculated using DFT. .... 89

Figure 4.9 Transmission electron microscope images of different Dh (top) and BTd (bottom), with scale bars of 50 nm. .... 90

Figure 4.10 In a) measurements of Dh and BTd particles from a synthesis using 2 g PVP, and in b) measurements for Dh particles synthesized using different concentrations of PVP. .... 91

Figure 4.11 Three surface slabs used to calculate the energy associated with terminating an extra layer at a twin boundary..... 93

Figure 4.12 The geometry of the rounded corners when they are estimated as circular cones. ... 96

Figure 4.13(a) The corner concentration of Pt as functions of Pd and Pt external chemical potential. (b) A zoomed in Pt corner concentration map showing how Pt corner concentration changes with Pt and Pd precursor concentrations..... 98

Figure 5.1 TEM images of asymmetric Dh particles that have been previously observed. (a) Asymmetric Dh particle with two small segments, and (b) asymmetric Dh particle with one small segment. .... 103

Figure 5.2 Schematics showing the two cases when the disclination migrates out of the Dh MTP ..... 104

Figure 5.3 (a) As-synthesized particles synthesized with 50% PVP, (b) An asymmetric Dh particle synthesized with 110% PVP, and (c) An asymmetric Dh particle synthesized with 100% PVP ..... 105

Figure 5.4 As-synthesized particles synthesized with 75% PVP..... 106

Figure 5.5 TEM image of (a) – (h) asymmetric Dh particles synthesized using different amount of PVP, and the mirror symmetry is present in all syntheses conditions, and (i) a typical asymmetric Dh with geometric parameters a, b and c being labeled..... 107

Figure 5.6 (a) The re-entrant level of asymmetric Dh as a function of twin length, and (b) the histogram of the re-entrant level of 359 asymmetric Dh particles..... 108

Figure 5.7 Von Mises stress concentration in asymmetric Dh particles with geometric parameters: (a)  $L = 1, h = 1, a = 0.102, b = 0.578, c = 0.34$ , (b)  $L = 1, h = 1, a = 0.306, b = 0.374, c = 0.34$ , and (c)  $L = 1, h = 1, a = 0.612, b = 0.068, c = 0.34$ . .... 110

Figure 5.8 (a) Strain energy density of Dh with different geometric parameters,  $a = [0.102, 0.204, 0.306, 0.408, 0.51, 0.612]$ ,  $b = [0.578, 0.476, 0.374, 0.272, 0.17, 0.068]$ , and  $c = 0.34$  (b) The dimensionless surface energy parameter at the corresponding geometric parameters. .... 110

Figure 5.9 (a) Illustration of one segment in the asymmetric Dh. The gray facet corresponds to 111 facets, and the rest of the facets are 111. (b) Schematic of an asymmetric Dh with geometric parameters a, b and c.....	111
Figure 5.10 Free energy of asymmetric Dh as a function of a, with c and re-reentrant level fixed at 0.34 and 1.7, respectively, at different sizes.....	113
Figure 5.11 Calculated a values at free energy minima as a function of Dh particle size.....	114
Figure 6.1 (a) Poisson's ratio of a Au/Ag alloy as a function of Au volume fraction (homogeneous concentration). (b) Bulk modulus of a Au/Ag alloy as a function of Au volume fraction.....	126
Figure 6.2 Change in energy of a Dh (5 nm in radius, 3 nm in thickness) as a function of homogeneous (initial) Au concentration at 300K and 1000K.....	127
Figure 6.3 Temperature-dependent segregation inside Dh and Ic bimetallic nanoparticles. The local Au concentration is plotted as a function of particle radius, where $r = 0$ represents the center of the particle. Dh particles (5 nm in radius with 3 nm thickness) are estimated as elastic cylinders with only plane strain. Ic particles (5 nm in radius) are estimated as elastic spheres that have radial strains.....	128
Figure 6.4 Chemical potential of Au as a function of homogeneous Au concentration at 300K and 1000K.....	129
Figure 6.5 Degree of segregation of Dh and Ic particles as a function of Au homogeneous concentration at different temperature. The degree of segregation is linearly related to the total change in energy in a particle. Ic particles have higher inhomogeneous strain, resulting in a higher degree of segregation.....	130
Figure 7.1 The schematic of the wide-field LSPR set-up.....	135

- Figure 7.2 (a) normalized LSPR spectra of two single Au nanospheres, and (b) their corresponding mean square displacements ..... 139
- Figure 7.3 (a) LSPR spectra of three single Ag prisms, and (b) their corresponding mean square displacements ..... 140
- Figure 7.4 Four frames (551 nm, 593 nm, 722 nm, 782 nm) from the 100 frame image stack, which were taken at 1 hr, 2 hr, and 3 hr after the beginning of the reaction, respectively. The flakes appeared in 2 hr images were CTAB. (Video 1-3)..... 141
- Figure 7.5 TEM images of Au nanorods. Au nanorods reaction solution were diluted 100 times in (a) water, (b) 1M glucose and (c) 40% Glycerol aqueous solution, respectively. .... 142
- Figure 7.6 TEM images of Au nanorods synthesized with different dilution. (a) 2 times diluted seed solution was added in undiluted growth solution; (b) 10 times diluted seed solution was added in undiluted growth solution; (c) 100 times diluted seed solution was added in undiluted growth solution, and (d) 100 times diluted seed solution was added in 5 times diluted growth solution..... 143
- Figure 7.7 (a) Time series images of Ag nanoparticles in solution for the photo-mediated synthesis, and (b) UV-Vis spectra at different reaction time ..... 144
- Figure 7.8 (a) UV-Vis spectrum of Ag nanosphere with a diameter around 15 nm, (b) The tiff image acquired by the EMCCD at 450 nm, (c) - (e) Single particle spectra of the corresponding particle labeled in (b) ..... 145
- Figure 7.9 (a) The molecular structure of 3-Mercaptopropyltrimethoxysilane (MPS), and (b) SEM image showing the Ag nanoprisms synthesized in the liquid flow cell after illuminated with 550nm light for 5 hr ..... 146
- Figure 7.10 Illustration of SEM-correlation single nanoparticle LSPR measurements. The Ag seed particles were immobilized on the ITO surface and a distinct patten was etch on the ITO

surface to facilitate identification. The area under the etched line was characterized via STEM after the growth. The time-resolved single particle spectra of two Ag nanoparticles were present and both of them underwent a blue shift..... 147

Figure 7.11 (a) A HREM image of a polyparticle. (b) Morphology distribution of Ag seed particles at different period of oxidation time..... 149

Figure 7.12 (a) Morphologies of the as-synthesized Ag seeds. The majority of the seed particles had single-crystalline structure. (b) and (c) shows the morphologies of the Ag seed particles after O<sub>2</sub> plasma treatment, and all of them appeared to be polycrystals. .... 149

Figure 7.13 Typical lamp profiles of (a) Halogen lamp, (b) Xe lamp, and (c) super-continuum white light source ..... 150

Figure 7.14 TEM images of Ag nanoparticles synthesized using different amount of Ag seed solutions. The yield of Ag nanorods increases with decreasing amount of Ag seeds added. The aspect ratio of synthesized Ag rods increases with decreasing amount of Ag seeds added ..... 152

Figure 8.1 Pd Dh particles does not have {111} re-entrant facets..... 159

Figure 8.2 HADDF/TEM images of Ta/TiO<sub>2</sub> and Ta/SiO<sub>2</sub>, before and after electron beam irradiation ..... 162

## CHAPTER 1

### **Introduction**

## 1.1 Motivation

Metal nanoparticles, typically 1 to 100nm, have been intensely studied in recent years. Owing to their unique optical, electronic and catalytic properties, which are different from their bulk counterparts, they are widely used in a variety of applications. [1-5] Metal nanoparticles have been used without notice since medieval time, and for instance, they could be found in a 4<sup>th</sup> century AD Lycurgus cup or medieval stained glasses. The early theoretical work including Wulff construction and many other extended forms have been focused on the shape and growth of nanoparticles.[6-11] The development of transmission electron microscopy in the 20<sup>th</sup> century made the imaging of these particles possible, and there were enormous amount of efforts on experimental studies of nanoparticles' structure, morphology, and surfaces.[12-25] Now they could be found everywhere, from heterogeneous catalysts, solar cells, drug delivery, to sensors for single molecule detection. [26-29]

There are increased amount of efforts put into the methods of synthesizing and utilization of nanoparticles in the past decade. As shown in Figure 1.1, the number of scientific papers with the keyword 'nanoparticle' has increased linearly from 2005 to 2014. [30] Only about one in thirteen papers which have 'nanoparticle' as a key word also includes 'shape' as a key word, and only one in two hundred has 'thermodynamics' as a keyword. However, 'shape' is crucial in determining the properties of nanoparticles when used in different applications. To understand the thermodynamics and kinetics of nanoparticles is the key for more controllable and reproducible synthesis methods.

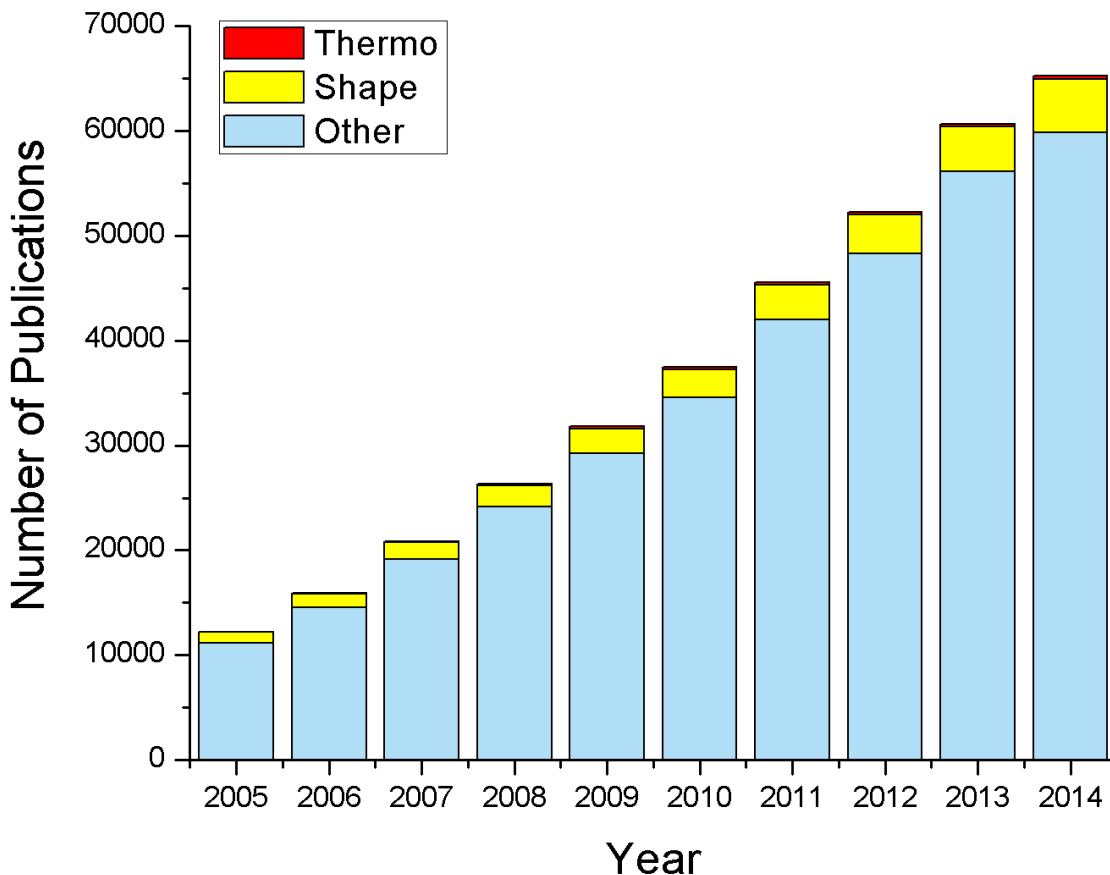


Figure 1.1 Histogram of number of publications per year, which contain only ‘nanoparticle’ as a key word are labeled in blue, and the ones also have ‘shape’ as a keyword is shown in yellow and the ones that also have ‘thermodynamics’ as a keyword are in red.

The chemical and physical properties of anisotropic noble metal nanoparticles are correlated to their structures. [31-33] Wulff construction is the simplest model in terms of determining the equilibrium shape of free standing particles. There are number of extensions, which take twinning, introduction of substrates and kinetics into consideration. According to Wulff construction,[6] the equilibrium shape of a single-crystalline FCC metal nanoparticle will be truncated octahedron in vacuum. However, for solution-based synthesized particles, there are numerous anisotropic shapes which deviate from the equilibrium Wulff polyhedron. There are a

number of reasons for the appearance of the anisotropic shapes, such as, the kinetically-controlled growth in solution; the capping agents, solvents, or impurity effects on surface energies of different facets, which make it differ from the vacuum case. In Figure 1.2, many shapes of interests are given and they are divided into thermodynamic and kinetic controlled shapes. In the last decade, a lot of solution-based syntheses of anisotropic metal nanoparticles with various sizes and morphologies have been developed, but they still lack of good control.[34]

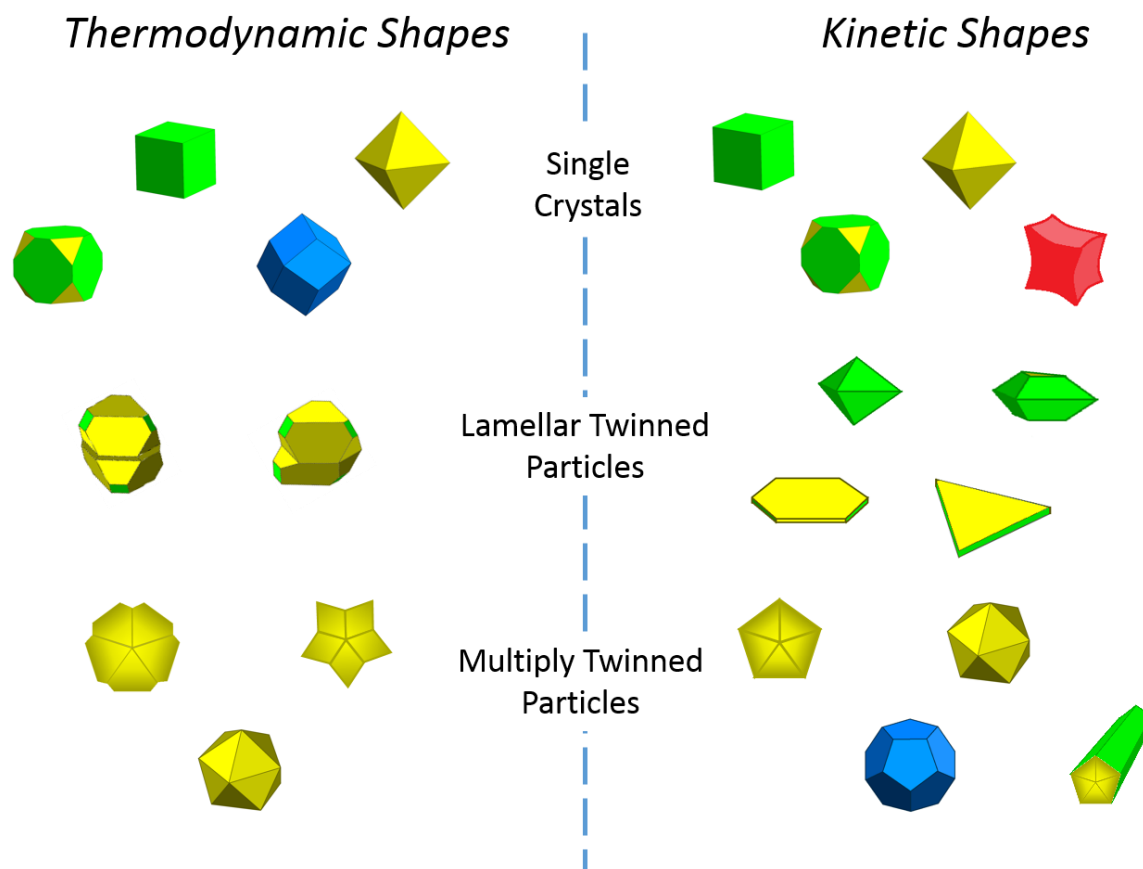


Figure 1.2 Most commonly observed nanoparticle shapes are divided into two cases, ones which can occur from thermodynamic control and ones which are only from kinetic control. They are split into the three broad categories of Single Crystals, Lamellar Twinned particles and Multiply Twinned Particles. Every thermodynamic shape can also arise from kinetics, but the converse is not true. The facets are color coded, yellow for {111}, green for {100} blue for {110} and red for higher index.

Bimetallic nanoparticles are of interest due to their physical and chemical properties, which differ from their monometallic counterparts, and are dependent on their size, composition and structure. Their unique chemical and physical properties make them useful in many optical, electronic and catalytic applications. One composition tunable attribute is the localized surface plasmon resonance (LSPR) in the UV-visible-NIR wavelength range. [35, 36] Noble metals such as Ag, Au or Cu are known to have unique optical properties, such as localized surface plasmon resonance [37], and both theoretical and experimental works have shown that the LSPR energy varies with the composition as well as the morphology of the alloy nanoparticles. [35, 36] A second property of interest is the catalytic behavior. [38-42] Bimetallic nanoparticles have been widely used in many reactions such as CO and alcohol oxidation, nitrogen oxide and organic molecule reductions, dehydrogenization reactions [38, 41] and show enhanced selectivity compared to their monometallic counterparts. [39, 43] It is established that the surface composition and surface segregation, i.e. deviation of the surface composition from the bulk, changes the chemical properties of the surface and the catalytic performances. [44-48] Compositional variations can also change which facets are exposed, which can be significant as different facets can have different catalytic activities and selectivity. [49-51]

My thesis focuses on unraveling the structural related thermodynamic and kinetic properties of metal and bimetallic nanoparticles, aiming to provide methods to predict the nanoparticle growth, rather than a purely synthetic or descriptive approach.

## **1.2 Organization**

This dissertation is presented as follows: chapter 2 provides a brief overview of how thermodynamics and kinetics affect nanoparticle size, shape, structure and elemental distribution.

Chapter 3 illustrates the experimental methods utilized in this work. This thesis addresses problems in two main research areas. Chapter 4 to 6 cover the studies of the structural-related thermodynamic and kinetic properties of metal and bimetallic nanoparticles. Chapter 4 provides the experimental evidence of smooth composition gradient and corner enrichment of Pt in Pt/Pd bimetallic nanoparticles. A growth model is presented to explain the formation of smooth composition gradient and corner enhancement of Pt within the Pt/Pd particles. A thermodynamic model explaining the origin of corner rounding in nanoparticle shapes is also discussed. Chapter 5 presents the experimental observation of asymmetric decahedral (Dh) nanoparticles, and analyzes the thermodynamic stability of asymmetric Dh particles based on the energy contribution from both bulk strain energy and surface free energy. Chapter 6 discusses the strain-induced segregation in bimetallic nanoparticles. The second area of research is to understand the growth mechanism of metal nanoparticles *in situ* via dark-field optical microscopy. Chapter 7 illustrates the super resolution plasmon microscopy, and presents the *in situ* investigation of noble metal nanoparticle growth mechanism via this set-up. Future work are also suggested. Finally, chapter 8 summaries the work presented in this thesis and discusses some possible future directions.

## CHAPTER 2

### **Background:**

**Shape, Thermodynamics and Kinetics of Metal and Bimetallic Nanoparticles**

## 2.1 Thermodynamic and Kinetic Shapes

The objective of my studies is to understand the thermodynamic and kinetic properties as a function of size, shape, stress and external environment, and further reveal the nanoparticle growth mechanisms. In order to understand how thermodynamics and kinetics contribute to the final size, morphology and compositions of nanoparticles, the basic energetics should be introduced.

In an atomistic description, the total energy of an ordered, crystalline nanoparticle can be written as,

$$E = \sum_{i,j,k} a_{ijk} n_i n_j n_k + \sum_{i,j} b_{ij} n_i n_j + \sum_i c_i n_i + d + \sum_i e_i / n_i + \sum_{ij} f_{ij} / n_i n_j \dots \quad (2.1)$$

where  $n_i$  are positive integers indicating the number of atoms along particular directions. The terms with inverse powers are included to account for atomicity.

By assuming the nanoparticles have convex shapes for all single crystalline regions,  $n_i$  could be replaced with a vector  $\underline{h} = (h_1, h_2 \dots h_k)$  for  $k$  facets, which is a vector with normal distance for each facet from a common origin. All  $h_i$  are real but not necessarily positive. The energy can now be written as,

$$E = \sum_{i,j,k} A_{ijk} h_i h_j h_k + \sum_{i,j} B_{ij} h_i h_j + \sum_i C_i h_i + D + \sum_j F_j / h_j \dots \quad (2.2)$$

As illustrated in Figure 2.1, each  $h_i$  is the sum of a geometric distance from the origin to the outermost plane and a ‘‘Gibbs distance’’ outside the surface. The ‘‘Gibbs distance’’ is needed to properly achieve the transition from atomistic to continuum models. [52, 53] This is called the Gibbs equimolar partition for the surface. For a bulk surface, the relevant distance is half that to

the first atomic plane that being removed to create the surface, effectively using a Wigner-Seitz unit cell around each atom or basis of atoms in the unit cell. When the size of the particles is large, the first term is proportional to the volume and the number of atoms. For particles with relatively small sizes, there is a non-linear relationship between  $h_i$  and the number of atoms along specific directions, and it has been discussed by Hamilton.[53]

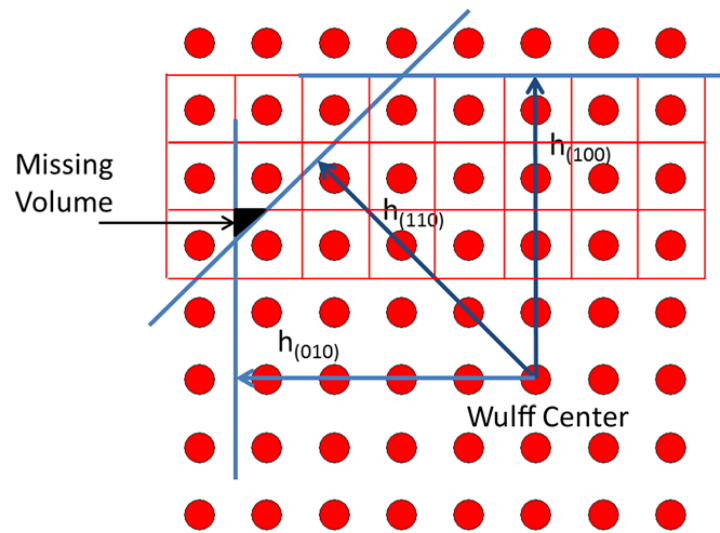


Figure 2.1 Illustration of the equimolar cut for surfaces in terms of the Wigner-Seitz unit cells

The continuum shape is defined as a set of planes, normal to  $h_i$ , and all continuum quantities are defined via partial derivatives or integrals, in order to take care of non-linearity properly. The “Gibbs Volume” ( $V_G$ ) is the volume within the defined shape, and the “Gibbs Surface Area” ( $A_G$ ) is the external surface area, both in conventional units. Therefore, for continuum models, the energy terms  $O(h^3)$  corresponds to the bulk cohesive energy and strain energy;  $O(h^2)$  corresponds to the total surface free energy and surface stress energy;  $O(h)$  corresponds to edge energy terms including counting correction and  $O(h^0)$  are corner energy terms including counting correction. (e.g. to make sure it is correct for the limit of a single atom) In general,

$\Delta$  surface energy  $\approx \Delta$  strain energy  $> \Delta$  surface stress energy  $> \Delta$  twin boundary energy  $\approx \Delta$  lattice parameter  $\approx \Delta$  counting corrections

To convert Equation 2.2 to a continuum model, the first term can be written as,

$$\sum_{i,j,k} A_{ijk} h_i h_j h_k = V_G \left( \frac{\mu^B}{v_0} + W_D \right) \quad (2.3)$$

where  $\mu^B$  is the bulk chemical potential per atom in a strain free condition;  $v_0$  is the volume per atom, and  $W_D$  is the bulk strain energy density, which could be size-dependent. The bulk energy term could be temperature dependent when more than one component is included in this system, because entropy of mixing will play an important role. It will be discussed in detail in Chapter 6.

Similarly, the second term in Equation 2.2 can be expressed as,

$$\sum_{i,j} B_{ij} h_i h_j = V_G^{2/3} (\gamma_{111} \varepsilon_w + \langle g_{ij} e_{ij} \rangle \varepsilon_g) \quad (2.4)$$

where  $V_G^{2/3} \gamma_{111} \varepsilon_w$  is the strain-free surface energy term and  $V_G^{2/3} \langle g_{ij} e_{ij} \rangle \varepsilon_g$  is the surface stress energy.  $g_{ij}$  is the surface stress tensor and  $e_{ij}$  is the surface strain.  $\varepsilon_w$  is a dimensionless energy parameter and it can be expressed as,

$$\varepsilon_w = (\gamma_{111})^{-1} \left( \int \gamma dS \right) \left\{ \int dV \right\}^{-2/3} \quad (2.5)$$

This  $\varepsilon_w$  is also a function of surface anisotropy ratio  $\alpha$ , which is the ratio between (100) surface energy and the surface energy of (111) facets.

Therefore, Equation 2.2 can be now written as sum of bulk, surface, corner and edge energies,

$$E = V \left( \frac{\mu^B}{v_0} + W_D \right) + V^{\frac{2}{3}} (\gamma_{111} \varepsilon_w + \langle g_{ij} e_{ij} \rangle \varepsilon_g) + O(h) \quad (2.6)$$

where  $O(h)$  here includes edge and corner energies as well as any remaining counting effects, and the terms with inverse powers in Equation 2.1 and 2.2 have been ignored.

## 2.2 Minimum Energy Solutions

### 2.2.1 Wulff Construction for Single Crystals

The minimum energy shape is obtained by minimizing the total energy of the particle at a constant volume. If the bulk strain and surface stress terms are ignored, it is equivalent to minimize the dimensionless parameter  $\varepsilon_w$ . Also, it could be solved by the method of Lagrangian multipliers. For a single crystal, the minimum energy shape is the thermodynamic Wulff construction, and the shape  $S_w$  is given by, [54]

$$S_w = \{x : x \cdot \hat{n} \leq \lambda \gamma(\hat{n}) \text{ for all unit vectors } \hat{n}\} \quad (2.7)$$

This shape contains all the points  $x$  within  $x \cdot \hat{n} \leq \lambda \gamma(\hat{n})$ , where  $\hat{n}$  is a unit vector defined by the crystallographic orientation of a facet  $(hkl)$ ;  $\gamma(\hat{n})$  is the orientation-dependent surface free energy, and  $\lambda$  is a constant (Lagrangian Multiplier) that is related to the volume of the particle. Another common way to define the Wulff shape is that it is the inner envelope of free energy as a function of crystallographic orientation, which was first proved by Von Laue [7] and Dinghas,[55]

$$\gamma_i = h_i / \lambda \quad (2.8)$$

where  $h_i$  is the normal distance from the center of the particle to a crystallographic facet  $i$ , and  $\gamma_i$  is the orientation-dependent surface free energy of the facet. The Wulff shape applies to free-standing single crystal particles, and the shape is determined by the surface energies, which depends upon the external environment, but nothing else.

### 2.2.2 Winterbottom Construction

The minimum energy shape can be achieved when a flat substrate is introduced. The minimum energy solution is given by Winterbottom.[56] In this case, if the surface free energy of the metal particle is  $\gamma_i$ , there will be an additional free energy term  $\gamma_A$  for the adhesion when the exposed surface of the nanoparticle is replaced by an interface, which leads to an effective interfacial energy term of  $\gamma_{Int}$ , where  $\gamma_{Int} = \gamma_i + \gamma_A$ . This should be used instead of  $\gamma_i$  when determining the minimum energy shapes. The interfacial free energy term can be either positive or negative depending upon the chemical bonding between the nanoparticle and the substrate, which depends upon the chemical species, the misfit between the nanoparticle and the substrate, as well as details of the interfacial structure. The interfacial properties also have an effect on segregation.[57] As illustrated in Figure 2.2, if  $\gamma_A$  is positive, the Winterbottom shape is equivalent to a dewetting shape of a nanoparticle. If  $\gamma_A$  is negative, it is the equivalent of wetting with a full range in between the complete dewetting and the complete wetting. This construction can be extended to the case with two or more interfaces, which is called SummerTop construction,[58] although this is rather rare in real physical systems.

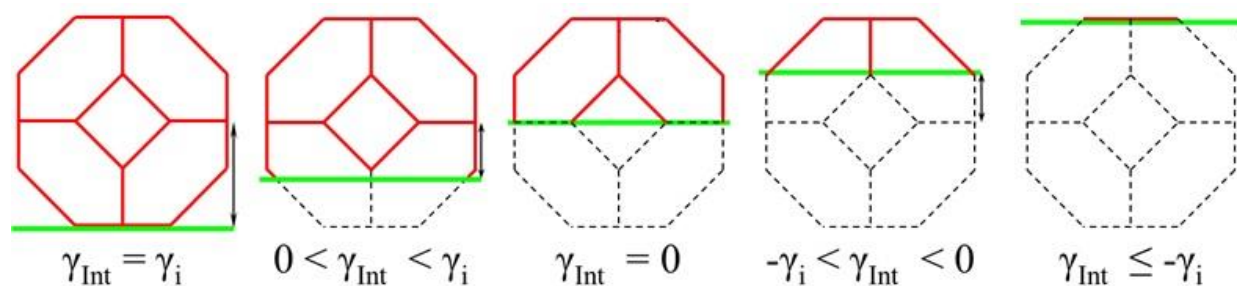


Figure 2.2 Schematic of the variation in shape of a nanoparticle, here with a (100) epitaxy on the substrate, as a function of the interfacial free energy. From left to right is the analogue of dewetting to wetting for a solid single crystal particle

### 2.2.3 Modified Wulff Construction for Multiply Twinned Particles

Instead of the existence of a boundary to an external support, there can be internal boundaries within nanoparticles, most commonly twin boundaries. Similarly, the approach is to find the minimum energy shape for each single crystal subunits with the twin boundaries taken into account. The composite particle was then assembled from these subunits, shown in Figure 2.3. Similar to the Winterbottom construction, an additional free energy  $\gamma_T$  is associated with each twin boundary. Then  $\gamma_T$  is partitioned to the two sides and generate a variant of the Wulff construction for each single crystal subunit. Finally the subunits are assembled to create the multiply twinned nanoparticle. This is called the “modified Wulff construction”. [11, 59] Each individual single crystal subunit must be convex, but the overall assembled particle does not have to be convex.

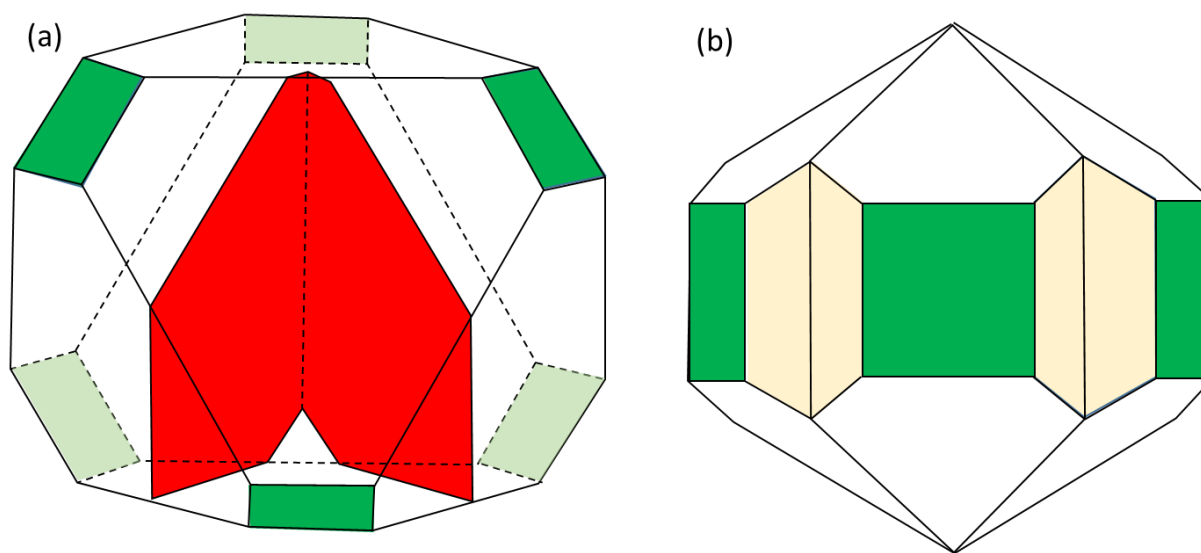


Figure 2.3 Illustration of the modified Wulff construction. For the three-dimensional Wulff shape shown on the left in (a) the region between two twin planes (red) is extracted. Five of these joined at the twin boundaries leads to the Dh shape shown on the right in (b), with the re-entrant  $\{111\}$  surfaces in yellow.  $\{100\}$  faces are green in both (a) and (b)

In modified Wulff construction, the final shape of the particle is the superset of the Wulff

shapes of individual single crystal subunit. The single crystal subunits are separated by twin boundaries and the twin boundary can be partitioned into  $\alpha\gamma_t$  (element A) and  $(1 - \alpha)\gamma_t$  (element B). There will be discrete values of  $\alpha$  which will give local minima of the total surface energy, because of the symmetry constraint.

For the simplest case,  $\alpha$  equals to  $\frac{1}{2}$ , and the two segments have the same volume. Also, this model can have a number of parallel twin boundaries, and this type of particles is called lamellar-twinned particles (LTPs). LTPs have closely packed  $\{111\}$  twin boundaries near the middle of the particles. For particles containing five single crystal segments and joint with 5  $\{111\}$  twins, they are called decahedral MTPs (Dh). The five single crystal segments are joint along a disclination along (110) direction. Twenty segments bounded by three non-parallel boundaries give an Icosahedral MTP (Ic). Examples of LTP, Dh and Ic particles are shown in Figure 2.4. If a particular structure is (at certain sizes) the lowest possible energy configuration, we will refer to it as a *globally thermodynamic* structure. If, however, it is only a local minimum when all the twin segments are the same, we will use the term *constrained thermodynamic* structure.

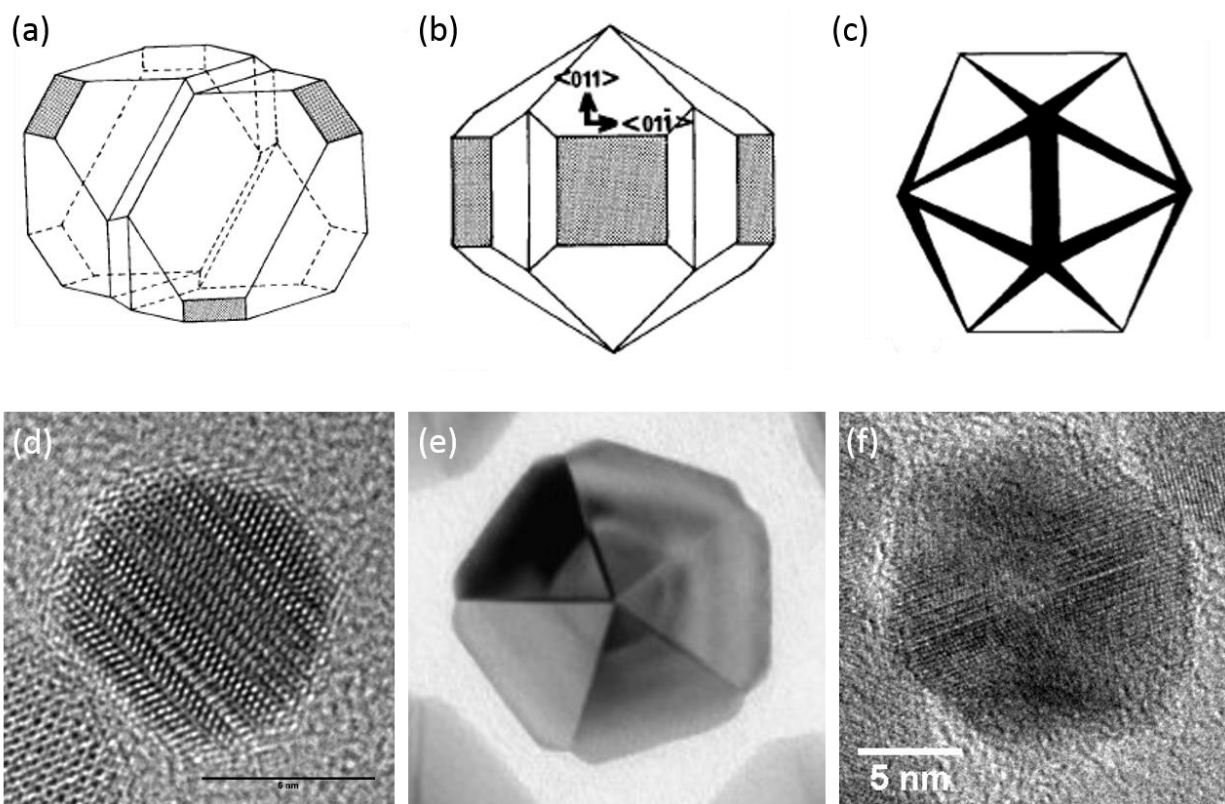


Figure 2.4 Schematics and TEM images of MTPs. (a) – (c) Schematics for (a) LTP with two parallel twin boundaries (b) Marks decahedral MTP and (c) Icosahedral MTP. (d) – (f) TEM images for (d) LTP with multiple parallel twin boundaries, (e) Marks Dh and (f) Ic.

Depending on the surface energy ratio  $\gamma_{111}/\gamma_{100}$ , the Dh can have different shapes. It is demonstrated in Figure 2.5. The one with re-entrant facets are commonly called Marks Dh. When  $\gamma_{111}/\gamma_{100} > 2/\sqrt{3}$ , the re-entrant notches will disappear, and the particles will form a rod-like shape, similar to that first investigated by Ino. [14, 17, 18] This is a constrained thermodynamic structure, not a global minimum. If  $\gamma_{111}/\gamma_{100} \ll 1$ , the (100) facets no longer appear in final shapes, and the Dh has a star like shape. This is a plausible global thermodynamic structure. The possibilities are more limited for Ic particles.

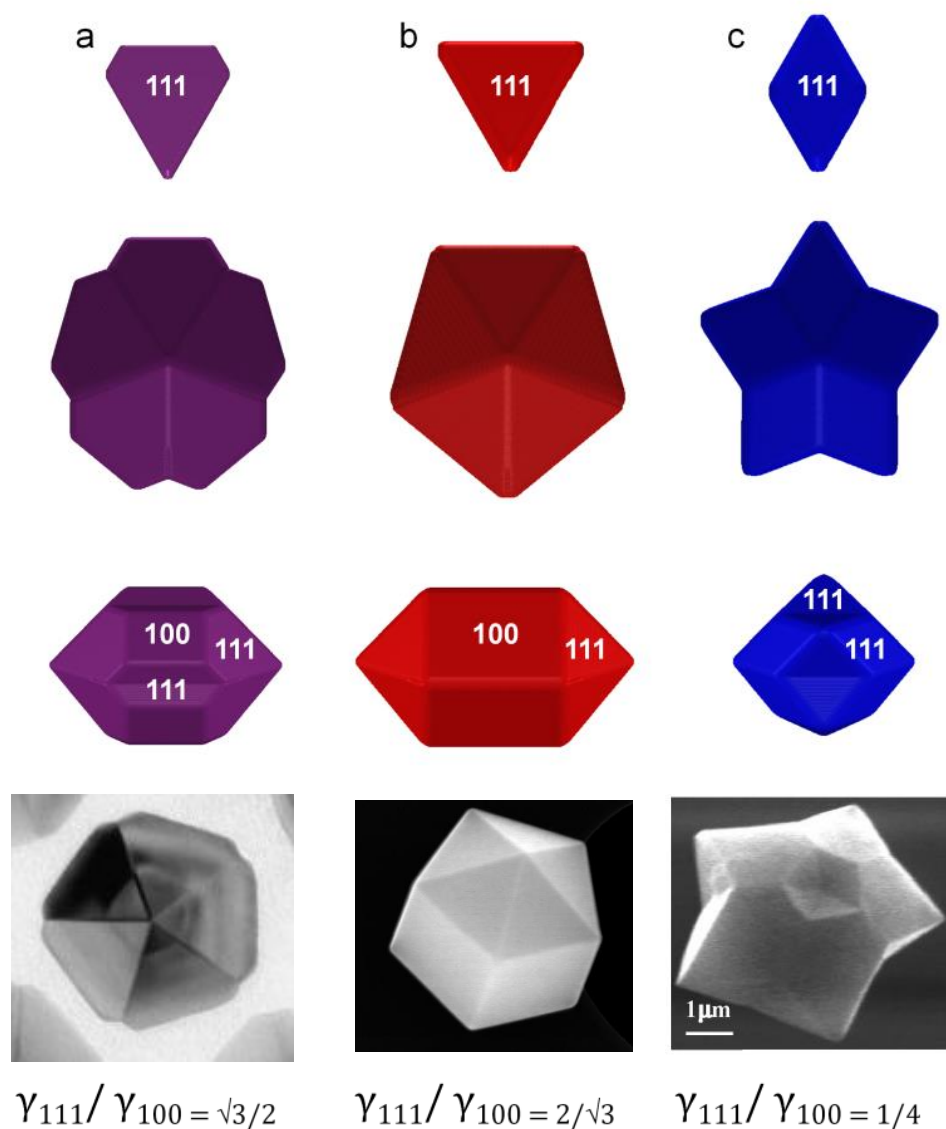


Figure 2.5 Different cases for Dh in three columns (a)-(c) with different ratios of the  $\{111\}$  and  $\{100\}$  surface energies. Shown at the top is the single segment, below the particle down the common  $[011]$  direction and below from the side. Experimental images are shown below

### 2.3 Kinetic Shapes

The various Wulff constructions correspond to the equilibrium shape. However, it is not clear that many experimental nanoparticles are synthesized or post-treated in the way that they can

reach their equilibrium shapes.

In order to understand how these shapes form, it is necessary to break down the processes taking place during growth by considering three regions as illustrated in Figure 2.6. Far from the particle, Region I contains some concentration of the relevant materials, dictated by the environment. There is Region II, around the particle, which includes atoms that directly interact with the growing nanoparticle. Lastly, there is Region III composed of monatomic terraces on the surface of the nanoparticle which grow by the attachment of atoms from Region II. Therefore, there will be a net flux of atoms from Region I  $\rightarrow$  Region II  $\rightarrow$  Region III.

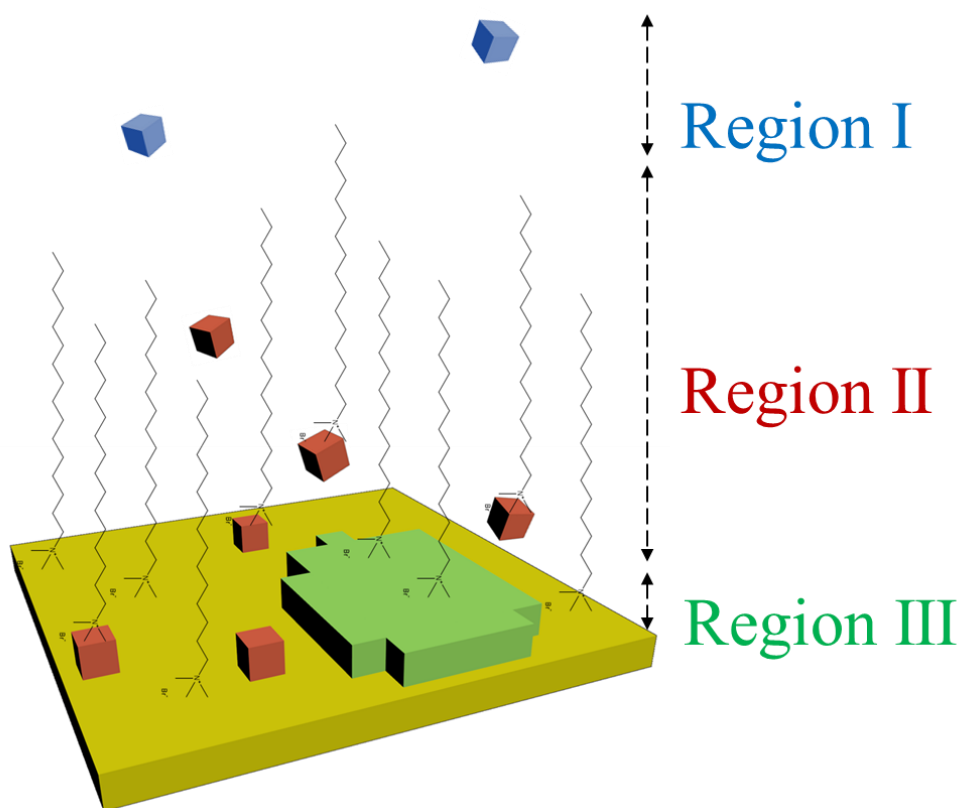


Figure 2.6 Schematic of the relevant regions for kinetic growth. Region III contains a nucleating terrace, Region II atoms that can diffuse to the terrace and Region I external atoms. Atoms are represented by cubes which are color coded by region, with the substrate yellow, and ligands near the surface are illustrated

For diffusion controlled growth, the rate limited step is the diffusion of materials from Region I to Region II, which is much slower than the attachment of atoms from Region II to Region III. This type of growth will likely lead to dendritic structures.

Interface controlled growth is often the case for shape controlled particles. The rate of growth is limited by the rate of atoms moving from Region II to Region III. There are monatomic terraces nucleated on an existing flat surface, followed by the growth of this terrace across the facet. The growth of the nanoparticle follows a layer by layer fashion. As the atoms added to the clusters are flexible, if the size is small enough, the atom arrangement can be changed. However, when the particle reaches some certain size, the atom rearrangement will not be energetically possible. The particle will act as seed for further growth.

For interface controlled growth, the rate is controlled by the nucleation of a small monatomic terrace on an existing facet and the growth of this terrace across the facet, in Region III. If the nucleation is fast relative to the growth of the terrace across the facet, the surfaces will be rough. On the other hand, slow nucleation leads to flat surfaces. The total energy of a circular single atomic high terrace of radius  $R$  can be written as,

$$E = \pi R^2 \Delta\mu N_S + 2\pi R \gamma_e N_E \quad (2.9)$$

where  $\Delta\mu$  is the chemical potential change per atom (negative for growth) for addition to the nanoparticle versus being in Region II;  $N_S$  is the number of atoms per unit area of the terrace;  $\gamma_e$  is the edge energy per atom and  $N_E$  is the number of atoms per unit length of the step. A classic form of a nucleation barrier is shown in Figure 2.7. The activation energy barrier is dependent on the step energy  $\gamma_e$  and the chemical potential relative to the external environment. According to classical nucleation theory, the rate of formation of a terrace above the critical nucleation size  $R_C$

is,

$$Rate = f_0 \exp\left(\frac{-\Delta E}{k_B T}\right) \quad (2.10)$$

where  $f_0$  is the attempt frequency of an atom to add to the terrace, and  $\Delta E$  is the nucleation barrier.

For a two dimensional terrace, the critical nucleus size is,

$$R_C = -\gamma_e N_E / \Delta\mu N_S \quad (2.11)$$

And the activation energy is,

$$\Delta E = -\pi (N_E \gamma_e)^2 / N_S \Delta\mu \sim -\pi (\gamma_e)^2 / \Delta\mu \quad (2.12)$$

The chemical potential is a function of concentration of atoms in Region II that can be added to the terrace. If the concentration is high, the deposition rate would be fast, and then the critical nucleus may only consists 2-3 atoms. There could be multiple terraces on a given facet which lead to rough surfaces. When the concentration in Region II is low, the deposition of atoms to the terraces is slow and the critical nucleus could be around 1nm in radius. It is unlikely to have multiple terraces present on any facet and the growth will be layer by layer.

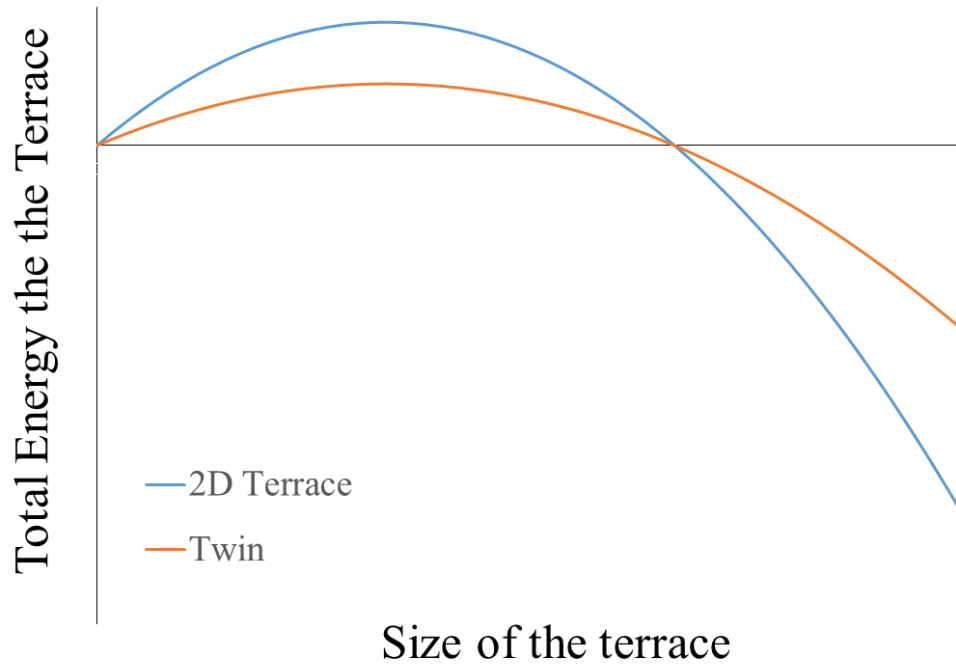


Figure 2.7 Energy versus size for a growing terrace, the blue curves corresponds to a full two-dimensional terrace as a circular disc and the orange curve corresponds to a half disc at a re-entrant twin boundary. The activation energy barrier at a re-entrant twin boundary is substantially lower than that of the flat surface case

### 2.3.1 Kinetic Wulff Construction

Once the terrace is nucleated, the contribution of the bulk free energy will dominate, and the growth of this terrace will be spontaneous, as the free energy of the terrace formation will be negative. The net velocity of nucleation and growth of the terrace on any given facet can be defined as growth velocity  $v_i$ . This growth velocity is independent of the particle size. Fast growing facets will not appear in the final shape, and only the slow growing facets will be present.

This leads to a steady-state or Lyapunov stable solution for a single crystal and the shape  $S_K$  is given by,

$$S_K = \{x: x \cdot \hat{n} \leq \lambda(t)v(\hat{n}) \text{ for all unit vectors } \hat{n}\} \quad (2.13)$$

It can also be written as the inner envelope of growth velocities along different crystallographic orientations,

$$h_i(t) = \lambda(t)v_i \quad (2.14)$$

This is called the “kinetic Wulff construction”. The final shape is controlled by the growth velocity  $v_i$ , rather than the surface energy  $\gamma_i$  of each facet. The kinetic Wulff shapes can be similar to the thermodynamic equilibrium shapes.

### 2.3.2 Kinetic Enhancement at Certain Sites

As mentioned in Section 2.2.3, many particles contain twins and their thermodynamic shapes (modified Wulff construction) have re-entrant surfaces. The nucleation at the twin boundary will be different from the case for flat surfaces. There is an important additional term associated with an enhanced growth at the twin. [12, 60, 61] As illustrated in Figure 2.8, there are more bonds that could be formed at a re-entrant twin boundary, compared to the flat surface. Density functional theory calculations show that the edge energy for a line of atoms at a twin is essentially zero, and it will be discussed in detail in Chapter 4. The energy for nucleating a semicircle at the twin boundary can be written as,

$$E = \frac{1}{2}\pi R^2 \Delta\mu N_S + \pi R \gamma_e N_E \quad (2.15)$$

The nucleus has the same critical radius and half the activation energy barrier, and the energy as a function of size is plotted in Figure 2.7. This leads to an effective enhancement at the re-entrant twin boundaries.

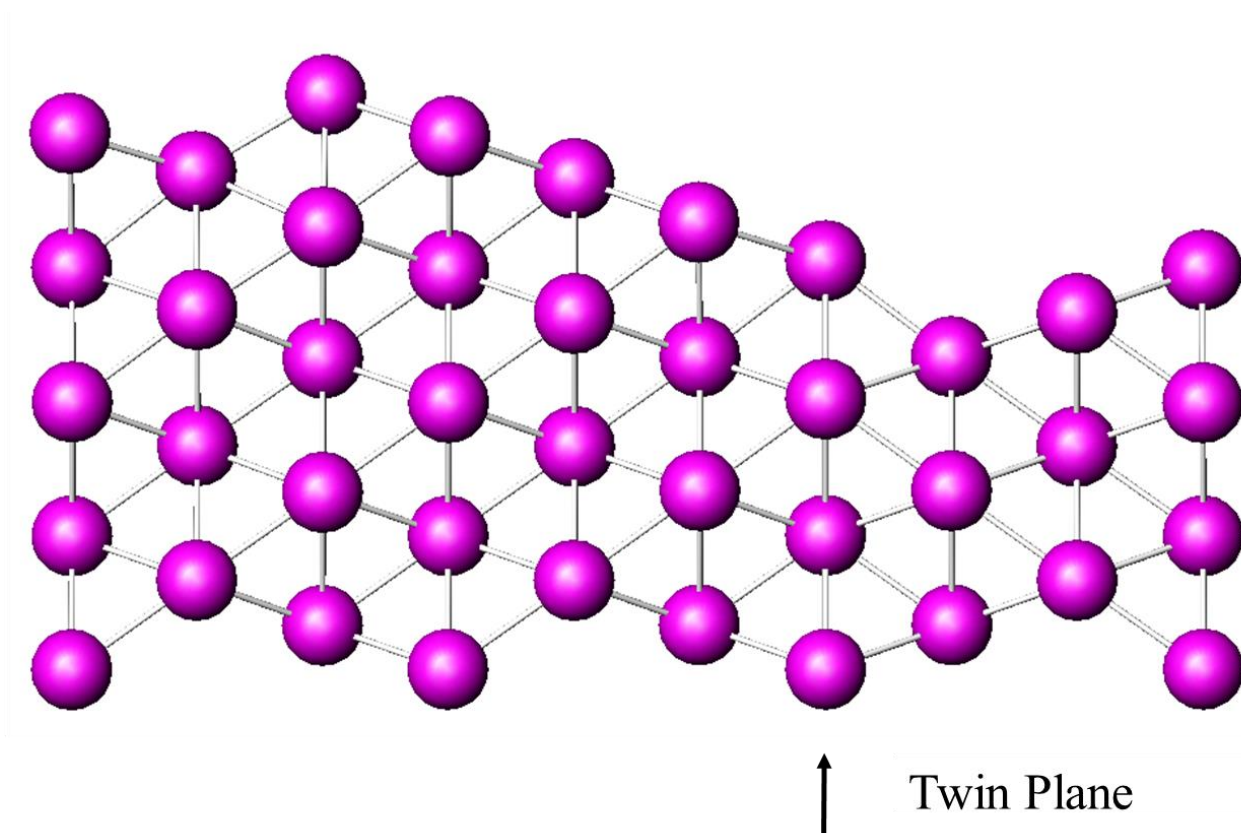


Figure 2.8 Explanation of enhanced growth at a re-entrant twin. The atoms in a terrace that terminates at the twin plane can bond to those on the other side, so the effective line energy is almost zero

For Dh particles, there is a disclination along the five-fold axis. It is well established that there could be faster growth at a screw dislocation. It is definitely possible that the same will occur at the disclination, so that the Dh particles will grow into nanorods or nanowires. Specific calculations are needed to confirm this, but it is a reasonable hypothesis.

### 2.3.3 Convex Shapes

Both thermodynamic and kinetic Wulff constructions lead to convex shapes. However, there are experimental results showing that particles with concave surfaces can be synthesized.

One possible explanation for this is the Berg Effect. [62, 63] The local concentration of the source materials at the corners is higher than that at the center of a facet, which can lead to self-similar shapes that are not convex. It is not very consistent with most experiments, but there may be cases where it can occur. However, it is not expected to be a stable solution, and it could lead to diffusion controlled growth of more complex shapes.

There is another possible explanation. In the kinetic Wulff shapes, the external surface is the slowest growing surfaces, which are moving away from a common Wulff point. During coalescence of nanoparticles and voids, there could be growth towards a Wulff point. The kinetic shape of the void is determined by the fastest growing facet, and the velocity is negative. As a result, the void is convex, and the surface of the crystalline material is concave, and the Wulff point is outside the crystal. Similar to the preferential growth at the re-entrant twins, it will be easier to nucleate a new layer at the concave vertex. Therefore, this type of shape may grow faster than the one with a convex external shape.

#### **2.3.4 Symmetry Breaking, Corner Rounding and Relationship with Segregation**

The Wulff construction in all cases should have the crystallographic symmetry of the materials of interest, however, the nanoparticles does not have to. For example, tetrahedral shapes can be formed even for a crystal with inversion symmetry. Also, modified Wulff construction for decahedral particles has five-fold symmetry. There are experimental results showing that the five-fold symmetry can be broken and the resulting shape has a mirror symmetry. The detailed analysis will be included in Chapter 5.

The chemical potential at the edges and corners can be nominally singular, which will be discussed in Chapter 4 in detail. There are vast amount of experimental results showing that the

nanoparticle corners are not necessarily sharp. In Chapter 4, there are quantitative measurements showing that the corners are rounded with a local radius of curvature which is independent of the nanoparticle size. [64] For sharp corners, the chemical potential at the corner would be greater than that of the atoms in the surrounding media, which is the growth solution for solution based growth. Also, for very small facets, it would not be possible to nucleate a new ledge on a small facet because there isn't sufficient area for nucleation. Therefore, there is a Lyapunov steady-state solution for a shape which already has steps where atoms can add – a locally rounded corner or edge. The radius of curvature would be similar to the critical nucleus size in three dimension. As mentioned previously, towards the end of a solution based synthesis, when the concentration of the source material is low, the critical radius can be large. This local thermodynamic equilibrium could also lead to complex elemental distribution within alloy nanoparticles synthesized under kinetic control. The details will be discussed in Chapter 4.

## **2.4 Mixed Growth**

The thermodynamic and kinetic Wulff constructions are the limits of very fast and very slow atom exchange between different surfaces respectively. Since the exchange of atoms depends upon the difference in the weighted mean curvature, the mixed growth will be achieved when the exchange of atoms is in between the two limits.

These shapes are then a mixture of the two classes of Wulff constructions. One possible example of this is shown in Figure 2.9. Pd nanoparticles were synthesized using citrate acid as a reducing agent, and PVP as surfactants. There is a transition from sharp decahedral bipyramids (kinetic shape) at higher concentrations of PVP to ones with re-entrant surfaces (thermodynamic shape) at lower PVP concentrations. To what extent this is a general phenomenon is unclear. It is

often hard to understand the relative role of kinetics and thermodynamics and couple them to nanoparticle synthesis parameters and reported experimental data – it can be fallen into one of the future directions.

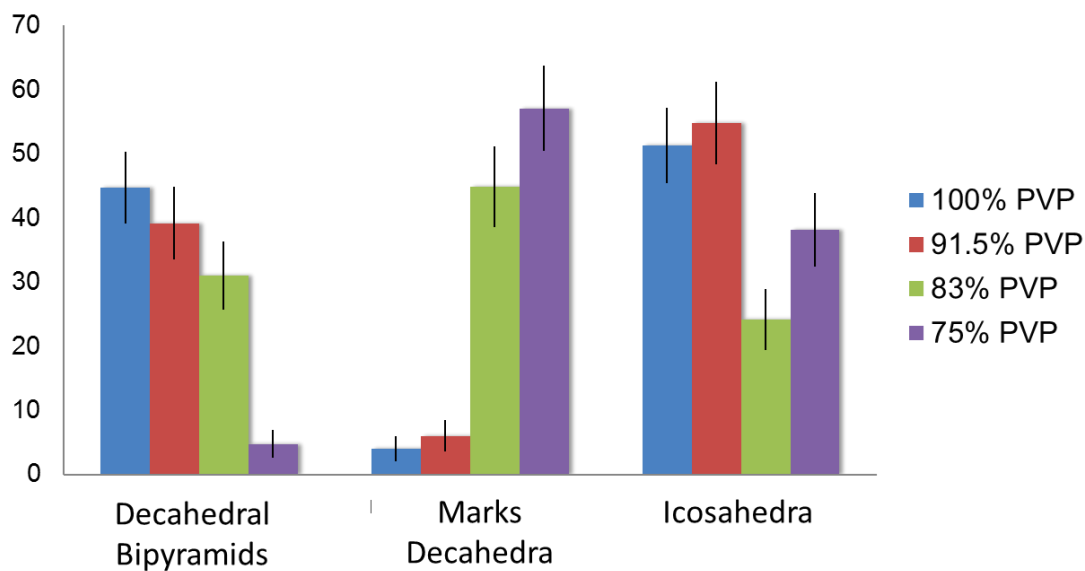


Figure 2.9 Relative populations of different MTPs indicating a transition from perfect Dh to Marks Dh from decreasing the PVP concentration

## 2.5 Strain Relaxation in MTPs

In single crystalline particles, the bulk strain is small and it could be neglected when calculating the total energy of the particles. However, in MTPs, they are not completely space filled and have solid angle deficiency of ~2% and ~6% for Dh and Ic, respectively. The internal strains have been considered in several ways in literature. Bagley[65] and Yang[66] suggested that there was a structure transformation from FCC to body-centered orthorhombic, which was no longer considered to be correct. The homogeneous strain was first analyzed by Ino.[14] De Wit first pointed out that the elastic strain could be formulated via classical Volterra disclinations.[67] The inhomogeneous strain for both Dh and Ic particles has been analyzed and approximated

analytically by Marks, Howie, and Yoffe.[68] More recently, Patala *et al.* have shown nonuniform elastic strain distributions in Dh and Ic particles via finite element analysis (FEA).[69] Zhou *et al.* have observed nonuniform strain in Dh nanowires using large-scale molecular dynamics simulations.[70]

The total strain energy in MTPs scales with the volume. When the particles reach some certain sizes, the total strain energy will become sufficient to nucleate stress-relieving dislocations. Since Dh particles are relatively easy to image, there are multiple experimental analyses regarding the stress relaxation existed in literature. [71] There is a detailed experimental analysis by Iijima for large Si Dh. [72] There are several possibilities, and a few cases have been directly observed, such as the splitting of the disclination via the introduction of stacking faults [73], via a tetrahedral stacking fault [74], or via formation of a grain boundary.[72] Not all the possibilities have been experimentally observed yet, but overall the theoretical models appear to be reasonably well supported by experimental evidences. There were dislocation being observed in Ic particles, [75] and more work is needed to discover the stress relaxation mechanism in Ic particles [75] because it is harder to image the defects via electron microscopes due to the overlap of the different segments along the beam direction.

An alternative stress relief mechanism is via point defects or segregation in alloy nanoparticles. In an alloy nanoparticle, the redistribution of atoms will also act as a stress-relaxation mechanism, which will not happen in their monometallic counterparts. In Chapter 6, a continuum model of strain driven segregation in bimetallic nanoparticle is described and this problem can be mapped to the Cottrell atmosphere, which is the distribution of point defects around a dislocation. The results indicate that while the change in free energy may be small, there will be

a noticeably segregation of larger atoms to the external surface and smaller ones to the core of the disclination. [76] In phase separated bimetallic nanoparticles, a similar process would occur and it has been analyzed in atomistic calculations for much smaller sizes by Ferrando *et al.* [77, 78] In small Ic particles, the phase separation does not have to be symmetric and one phase can be off to one side. The local expansion of the atoms will larger lattice parameter can assist in closing the gaps in Ic particles.

One different stress relaxation mechanism should be mentioned here. As analyzed independently by Ajayan *et al.* [19, 20] and Romanov *et al.* [79-84] The strain energy of a Dh approximated as a cylinder when the dislocation is off center by a fractional distance  $b$  scales as,

$$E = E_{b=0}(1 - b^2)^2 \quad (2.16)$$

When the disclination moves away from the center, there will be a net gain in the strain energy, at the cost of an increased total surface energy as the different segments are no longer symmetric modified Wulff shapes. The change in energy has been calculated at very small sizes by Ajayan *et al.* The calculations indicate that at small sizes, there will be an activation energy barrier for the disclination to move out of the center position because there will be an additional increase in surface energy of moving away from the symmetric case. At larger sizes, there will be no energy barrier as the bulk strain energy will dominate. This can introduce the edge dislocations in to the center as first hypothesized by de Wit, although this needs a fair amount of activation energy, so it would only occur at higher temperatures. An alternative is that the growth becomes asymmetric with a small deviation from symmetry rather than substantial displacement of the disclination. There are experimental evidences showing that this can occur with extensive evidence for asymmetric Dh in both Pd and Pd-Pt alloys. The details will be discussed in Chapter 5.

## 2.6 Segregation in Bimetallic Nanoparticles

Bimetallic nanoparticles are of interest due to their physical and chemical properties, which differ from their monometallic counterparts, and are dependent on their size, composition and structure. Their unique chemical and physical properties make them useful in many optical, electronic and catalytic applications. The addition of the second element makes the structures of bimetallic nanoparticles much more complex than their monometallic counterparts. The two elements can be phase separated such as in core-shell structures [85-87] chemically ordered, [88-90] or Janus structures, [91, 92] or the two species can be randomly mixed with complex segregation. [93-95] The driving force for segregation is always thermodynamics, reduction in the total free energy of the particle. In many cases it is driven by surface and/or interface free energies, with a higher concentration of one element at the outermost surface monolayer or in the selvedge region stretching 1-2nm in from the surface. The reduction in surface free energy may be intrinsic to the element if the particle is in vacuum, or may involve additional energy gain by bonding to chemisorbed gas molecules or ligands. Strain energies can also play a role, and any initial structure produced by designed growth can be important, as will be the kinetics of segregation via diffusion.

Most of these segregation processes are well known at the larger scale, but there is a subtle and important difference at the nanoscale. For a surface of a bulk material, the large bulk volume can act as a semi-infinite source or sink of atoms, so only the changes in surface components matter. In contrast, at the nanoscale the bulk volume is limited and the energy changes associated with changes in the bulk composition matter. This leads to new phenomena where the surface and bulk energy terms compete.

### 2.6.1 Analytical Models

The simplest way to model alloys is to ignore the potential composition differences between the bulk and surface, which is the ‘basic Wulff’ approximation. In this case both the bulk and surface energies are assumed to be equal to that of the homogeneous (initial) composition. It serves as a useful approximation for comparison purposes.

The next refinement of the model allows lowering the energy through surface segregation, while ignoring changes in the bulk concentration. Here, the bulk is treated as an infinite reservoir. The change in bulk energy is neglected and the surface energy is calculated for a surface with an underlying composition equivalent to the homogeneous (initial) composition. Of course, this violates the law of conservation of mass, but it is an acceptable approximation, particularly for large systems.

However, for alloy nanoparticles with a small number of atoms, the infinite reservoir approximation is not valid, as the number of surface atoms can be comparable to the number of bulk atoms. The change in bulk energy that is due to segregation needs to be included. This is called the alloy Wulff construction, developed by Ringe *et al.* [96]

The alloy Wulff construction considers the surface segregation in a small alloy particle at a given temperature. The surface segregation and equilibrium shape also depend upon temperature. To investigate this we will neglect the temperature-dependence of the enthalpy of mixing, assuming its contribution to the free energy is small compared to the entropy of mixing term, which is linear with temperature (T).

A reasonable form for the temperature dependence of surface energy was derived by Kristyan and Giber [97] based on statistical mechanics. The partial derivative of surface energy  $\gamma$  respect to temperature T,  $\frac{\partial\gamma}{\partial T}$  is materials dependent and can be written as,

$$\frac{\partial\gamma}{\partial T} = -R\ln(m) \quad (2.17)$$

where R is the gas constant; m the number of surface layers which is dependent on materials.

This temperature dependence can be expanded for an alloy,

$$\frac{\partial\gamma}{\partial T} = \frac{\partial\gamma_B}{\partial T} + x(A) \left( \frac{\partial\gamma_A}{\partial T} - \frac{\partial\gamma_B}{\partial T} \right) \quad (2.18)$$

and the temperature dependent surface energy is then as follows

$$\gamma(x, T) = \gamma_o(x) - R \left[ \ln m_B + x \ln \left( \frac{m_A}{m_B} \right) \right] T \quad (2.19)$$

where  $\gamma_o(x)$  is the surface energy as a function of surface composition at 0K. Therefore, the change in surface energy at temperature T is

$$\int \left\{ (\gamma_o(x^S) - \gamma_o(x^H)) - RT \left[ (x^S - x^H) \ln \frac{m_A}{m_B} \right] \right\} dS \quad (2.20)$$

while the change in bulk energy is

$$\int RT \left[ x^V \ln x^V + (1 - x^V) \ln(1 - x^V) - (x^H \ln x^H + (1 - x^H) \ln(1 - x^H)) \right] dV \quad (2.21)$$

where  $x^S$  is the surface composition of element A,  $x^H$  is the homogeneous composition of the alloy,  $x^V$  is the bulk composition of element A after segregation.

The contribution to the free energy from the entropy of mixing is minimal at low temperature but will dominate at high temperature with the entropy of mixing driving the particle toward homogeneity. This leads to an unresolved issue: when one tries to compare the experimental results with analytical models or numerical models, to what extent do these predictions represent quenched structures as opposed to the thermodynamic stable ones.

### 2.6.2 Numerical Methods

The analytical alloy Wulff construction gives valuable information as to how size, shape, temperature and composition affect the segregation in bimetallic nanoparticles. However, there are free variables in the model, so it is not always apparent how segregation will occur in specific cases. Here, it can be useful to use numerical approaches to model specifics, with potentials or similar, that represent the details of the system. Most of these use computational methods of finding the global minimum of the potential energy surface (PES), which is the configurational energy of the cluster as a function of the atomic coordinates.[98] They can be divided into two categories, first-principles methods and empirical/semiempirical methods. First-principles methods, also known as *ab initio* methods, are very informative, and they yield relatively accurate energies. However, they are very computationally demanding and thus only can be applied to systems of limited size.[99, 100] Empirical/semiempirical methods involve a system dependent potential[101-106] that can be of various forms. These models allow more efficient calculations thus enable calculations for larger systems. In many cases, the simulations use both DFT and empirical/semiempirical approaches, and apply a global optimization method. There are several recent reviews on global optimization of alloy clusters utilizing different algorithms/methods.[98-100, 107]

### **2.6.3 Thermodynamics vs. Kinetics**

The analytical and numerical models usually give the thermodynamic stable configuration. However, in a lot of solution-based syntheses, the nanoparticles will have complex composition profiles, resulting from the growth kinetics. Also, thermodynamics and kinetics can have a mixed control and can lead to the formation of particles with complex concentration profiles, which could be interesting when these particles are used in catalytic applications.

## CHAPTER 3

### **Experimental Methods**

### **3.1 Introduction**

This chapter first introduces the basics of colloidal synthesis of metal and bimetallic nanoparticles. Then the characterization methods including transmission electron microscopy (TEM), scanning electron microscopy (SEM), UV-vis spectroscopy and wide-field dark field optical microscopy will be introduced.

In order to obtain the structural information of nanoparticles, with accuracy on the atomic scale, transmission electron microscopy has been used as a major experimental tool in this study. The conventional, Bright Field (BF), Dark Field (DF) and High Resolution TEM (HREM) imaging has been used to obtain morphological information of metal and bimetallic nanoparticles in TEM. In scanning transmission electron microscopes (STEM), Annular Dark Field (HAADF and LAADF) and Annular Bright Field (ABF) images were collected at different collection angles, and they offer different contrast and provide valuable information. Energy Dispersive X-ray Spectroscopy (EDX) is a useful tool for determining the elemental distribution in bimetallic nanoparticles.

Noble metal nanoparticles have unique optical properties, known as localized surface plasmon resonance (LSPR) in the UV-visible-NIR wavelength range. The LSPR spectra of noble metal nanoparticles and their locations can be collected simultaneously via a super-resolution wide-field (WF) dark field optical microscopy set-up. This set-up enables direct monitoring of nanoparticle motion and growth.

### **3.2 Synthesis of Metal and Bimetallic Nanoparticles**

The metal and bimetallic nanoparticles used in this study were synthesized via colloidal methods. For colloidal metal nanoparticle synthesis, metal precursors are usually dissolved in

either water or organic solvent. Different type of reducing agents, such as citrate or ascorbic acid, *etc.*, are added to the solution to reduce the metal precursor to the metal<sup>0</sup> form. Surfactants are added to the solution to alter the surface properties of different facets and therefore help form particles with specific shapes. Detailed procedures for specific synthesis will be included in each chapters.

### **3.3 Electron Microscopy**

#### **3.3.1 TEM Basics**

TEM was the primary experimental tool used in this study. TEM can offer structural, morphological, elemental, and also electronic information of materials, by utilizing different types of electrons or characteristic X-ray from electron-specimen interactions. In conventional TEM, electrons will be emitted from the electron source (thermionic, field emission or cold field emission), and the electrons get accelerated and travel through the condenser lens and the condenser aperture. The high energy electron beam (usually 80-300 keV) hits the samples and interacts with the specimen and generates different types of signals. The schematic of electron-specimen interactions is shown in Figure 3.1. The images are formed from collecting transmitted electrons. The transmitted electrons will be focused and form an electron diffraction (ED) pattern at the diffraction plane. The objective aperture can select different type of transmitted electrons to form different types of images. When the direct beam is selected, the bright field (BF) images are formed. If the scattered electrons are chosen, then the dark field (DF) images will be formed. Some of the transmitted electrons will lose energy, and by analyzing the energy loss of the inelastically scattered electrons, the elemental and bonding information of the materials can be revealed. This spectroscopic technique is electron energy loss spectroscopy (EELS). The incident electrons can

also excite an inner-shell electron and an outer-shell electron will fill in to the inner-shell. There will be a radiation energy released and it could be in the form of X-rays. The characteristic X-ray will provide elemental information and this technique is called energy dispersive X-ray spectroscopy (EDX). The EDX detectors are installed above the specimen. The secondary electrons and backscattered electrons can be collected above the sample to form SE image and BSE images, respectively, and the SE and BSE detectors are often found in SEMs. The SE image shows the surface morphologies of the samples and the BSE image can also provide orientation and elemental information. Backscattered electrons are often collected to form orientation maps via electron backscatter diffraction. (EBSD)

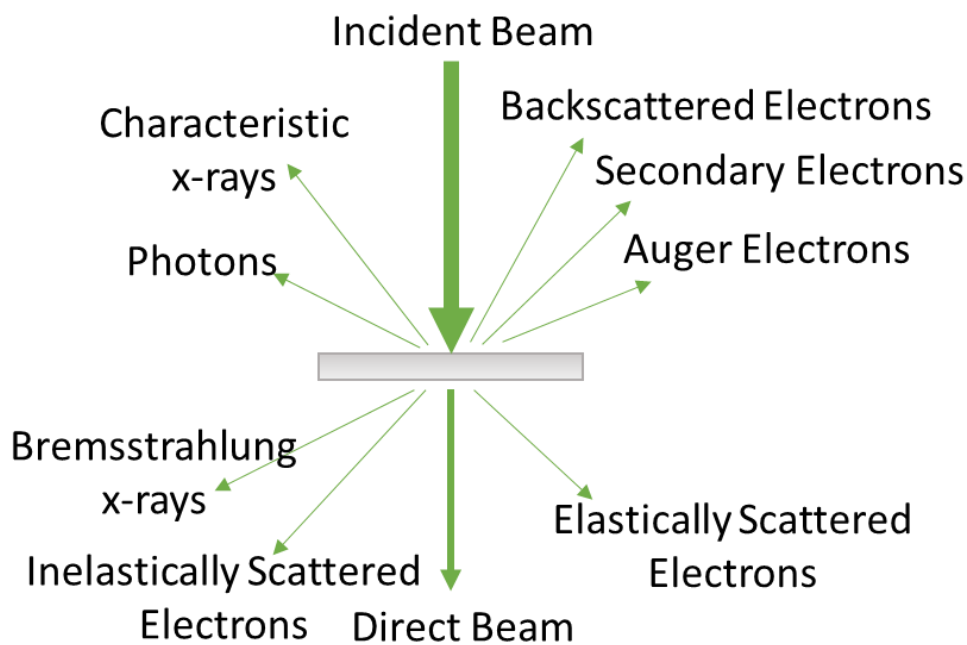


Figure 3.1 Schematic of the electron-specimen interaction

STEM is another major tool used in this study. In contrast to the parallel beam used in TEM mode, in STEM mode, the electron beam is converged to a probe (usually on the Angstrom scale for non-corrected STEM, and on the sub-Angstrom scale for probe-corrected STEM), and

scans across the sample. The transmitted electrons are scattered to different angles, and are collected by annular detectors. The high-angle incoherently elastically scattered electrons are collected by the annular dark field detector and form images with z-contrast. This type of imaging is called high-angle annular dark field (HAADF) imaging, and sometimes it is referred to z-contrast imaging. The contrast in HAADF imaging is directly related to  $Z^\alpha$ , where  $Z$  is the atomic number and  $\alpha$  is a constant ranging from 1.5 to 2, depending on the collection angle.  $\alpha$  approaches 2 when the collection angle is high and most of the Bragg reflections are avoided. When the collection angle is not large enough, diffraction contrast starts to appear. The term z-contrast imaging could be very misleading if the collection angle is not specified. The collection angle could be tuned by changing the projective lens current. The electrons at very low angles can be collected by the BF detector, and by blocking the direct electrons, annular bright field (ABF) images are formed.

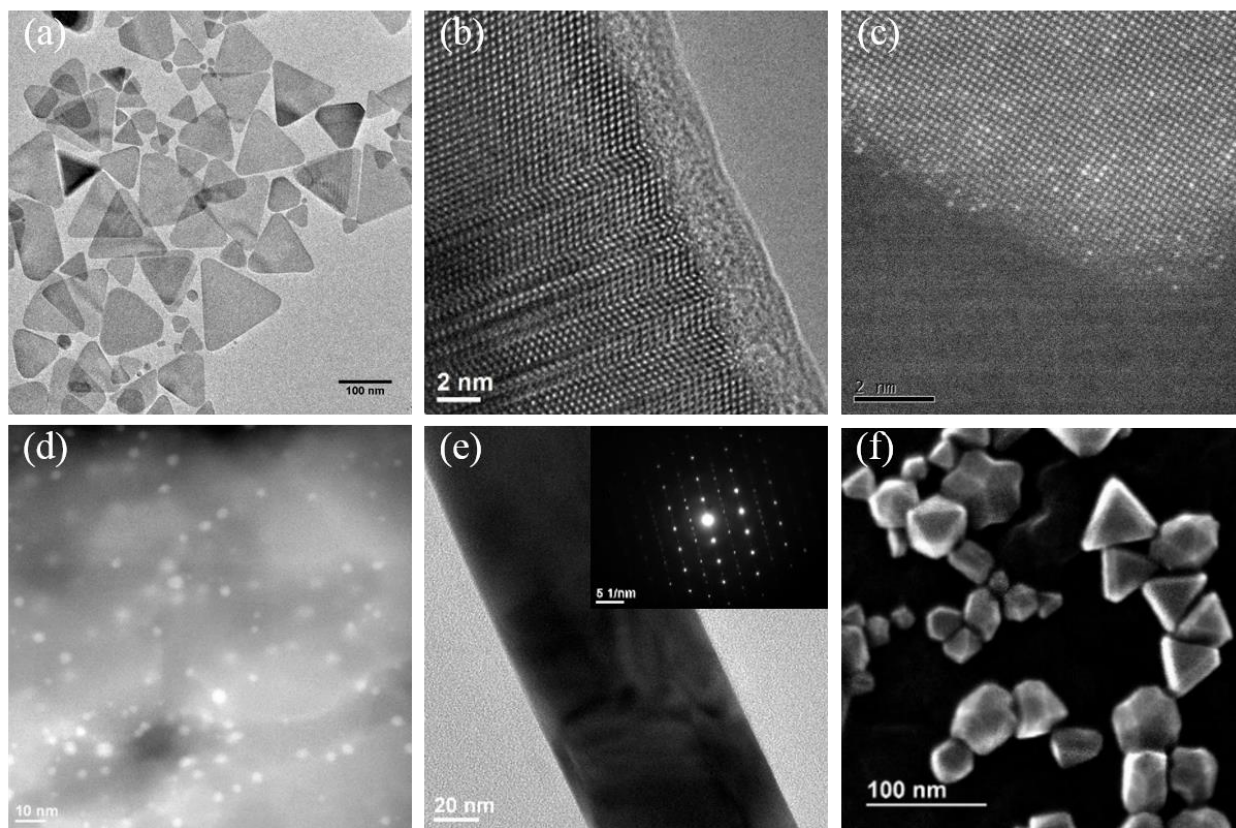


Figure 3.2 Applications of transmission electron microscopy (TEM): (a) Conventional TEM image of Ag nanoprisms (b) HRTEM image of GaAlAs/GaAs nanowires (c) HR-HAADF-STEM image of anatase  $\text{TiO}_2$  supported Ta single atom catalyst (d) HAADF image of mesoporous  $\text{SiO}_2$  supported Ag nanoparticles (e) electron diffraction pattern of a penta-twinned Au nanowire (f) secondary electron image of Pt/Pd bimetallic multiply twinned particles

### 3.3.2 Energy Dispersive X-ray Spectroscopy

Energy dispersive X-ray spectroscopy (EDX) is often used to reveal the compositional distribution in bimetallic nanoparticles. It could be performed in both TEM and STEM mode. The incident electron beam hits the sample and excites an inner-shell electron and an outer-shell electron will fill in to the inner-shell. A radiation energy will be released and it could be in the form of X-rays. The EDX detectors are installed above the samples. In STEM mode, the EDX detector collects the element-specific characteristic X-rays emitted, as a function of probe position. EDX maps, line scans or spectrum at any point on the sample can be acquired. Drift compensation

was used because sample drift was very common during the long acquisition. EDX can only identify elements heavier than Beryllium and is particularly sensitive to heavier elements. The spatial resolution of EDX depends on a number of factors, including the electron beam voltage and the sample thickness (particle size). EDX usually have 5-10% error of the measured composition.

For a binary system, weight percent of element A and B ( $C_A$  and  $C_B$ ) can be calculated by Cliff-Lorimer equation:

$$C_A/C_B = K_{AB} \cdot I_A/I_B \quad (3.1)$$

where  $I_A$  is the characteristic peak intensity of A above background,  $I_B$  the characteristic peak intensity of B above background and  $K_{AB}$  is the Cliff-Lorimer factor.

Steps for quantitative analysis include (1) background subtraction, (2) peak integration, and (3) k factor determination. There are several ways for background subtraction: window methods, modeling in background, and filtering out the background. Peak-integration methods depend upon previous background subtraction methods. We can experimentally determine the k factor by using a standard specimen of known composition. In addition, absorption correction can be necessary when one of elements preferentially absorbs X-rays.

### **3.3.3 Nanoparticle TEM Sample Preparation**

Colloidal synthesized metal and bimetallic nanoparticles are dispersed in aqueous or organic solution with surfactants capped around the nanoparticle surface. Before imaging, a great amount of surfactants need to be removed to avoid or minimize contamination issues in STEM, especially probe-corrected instruments. The as-synthesized particles were washed in different solvents by centrifugation for a couple of times. The washed particles were drop casted onto copper

TEM grids with supported carbon film and dried in air. Chromium and nickel grids were used for *in-situ* and *ex-situ* heating experiments so that the grids wouldn't undergo a shape change. The metal oxide supported metal nanoparticle or single atom catalyst samples were in the powder form. A few milligrams of the samples were dispersed in 3mL of ethanol. The suspension was also drop casted onto copper TEM grids with supported lacey carbon film. For TEM grids used in the JEOL ARM-200CF Cs-corrected STEM, 2 hr vacuum pre-annealing at 180°C were applied to the TEM grids to remove possible hydrocarbon or other contamination on the carbon films. 30s of weak Ar plasma cleaning of samples were often used to remove hydrocarbon or some surfactants before TEM experiments to slow down the contamination built-up onto the surface of the nanoparticles in the TEM column.

### 3.4 UV-vis Spectroscopy

Ultraviolet-visible spectroscopy (UV-vis) is a light spectroscopic technique which measures the absorbance or reflectance of the samples in the UV-visible-NIR region. The absorption spectra of synthesized metal nanoparticles were taken to have a rough idea about the size and shape of the particles, before taking them for further TEM characterization.

Unlike the absorption spectra of molecules, which corresponds to electronic transitions, involving  $\sigma \rightarrow \sigma^*$ ,  $n \rightarrow \sigma^*$ ,  $n \rightarrow \pi^*$ ,  $\pi \rightarrow \pi^*$  transitions and charge-transfers. Absorption spectra of metal nanoparticles have contribution from both absorption and scattering, which is also called extinction spectra. The extinction is the sum of absorption and scattering of the metal nanoparticles, and it is highly dependent upon the nanoparticle size and structure.

### 3.5 Wide-field Dark Field Optical Microscopy

Wide-field (WF) dark field optical microscopy is used to measure the LSPR spectrum and location of a particle simultaneously. This set-up is an inverted microscope equipped with a dark-field condenser, which only collects the scattered light from metal nanoparticles. The scattered light passes through the objective lens into a set of acousto-optical tunable filters, and only one wavelength goes to the EMCCD at a given time. This allows the simultaneous measurements of the LSPR spectra and locations of a moving particle. The schematic of the set-up is shown in Figure 3.3. In this technique, a white light source is sent through a dark-field condenser with a high numerical aperture (NA), and it illuminates the sample. The NA can be defined as,

$$NA = n \cdot \sin\theta \quad (3.2)$$

where  $n$  is the refractive index of the medium and  $\theta$  is the half angle of the cone of light. In order to get a higher NA, oil condenser is preferred over the dry condenser. The dark-field condenser has a circular block located at the center of the condenser, so that only a hollow cone of light can be transmitted and focused at the position of the sample. The scattered light passes through a 100x oil immersion objective with a variable NA and 0.7 being the smallest NA. The NA of the objective has to be smaller than the NA of the condenser so that the transmitted light from the condenser will not be collected by the objective. The scattered light passing through the objective will be sent through a set of acousto-optical tunable filters, and only one wavelength goes to the EMCCD camera at a given time. The wide-field set-up allows acquisition of multiple particles at the same time. The diagram and the picture of the dark field set-up are shown in Figure 3.3 and Figure 3.4.

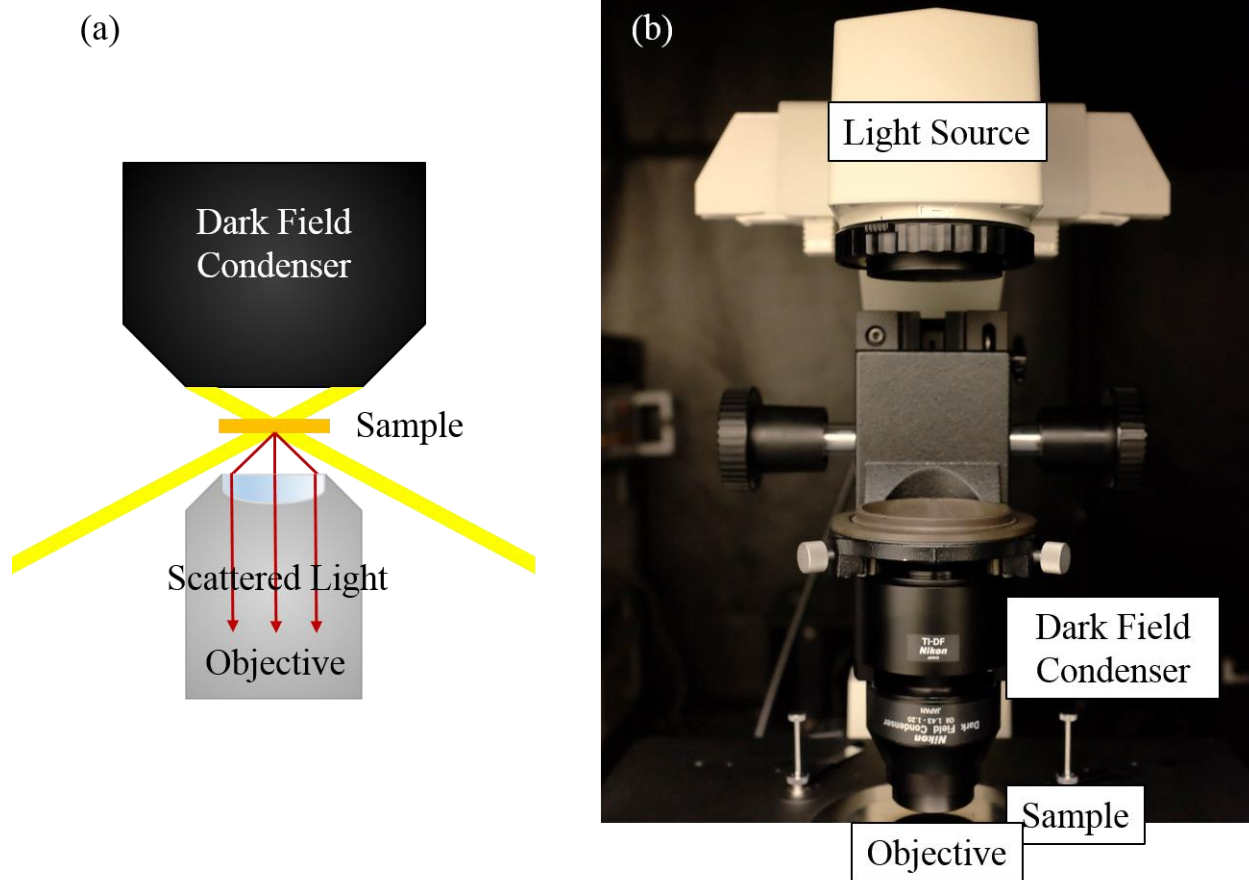


Figure 3.3 (a) Dark field microscopy setup. The transmitted light does go into the objective lens, but is blocked by the aperture. The yellow light in the diagram is exaggerated, but it emphasizes that only the scattered light is collected by the objective, and (b) picture of the apparatus.

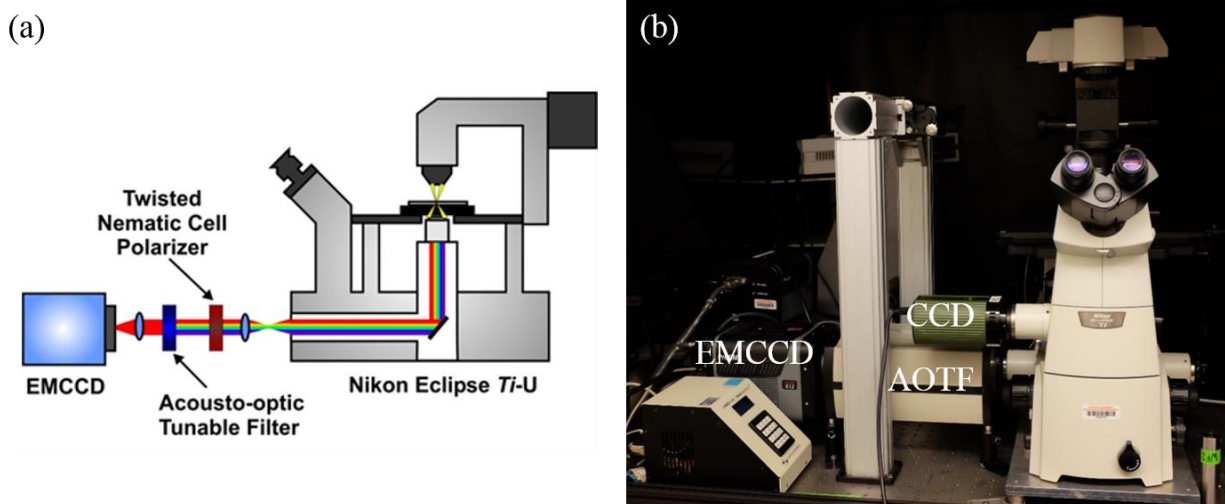


Figure 3.4 (a) Diagram of the WF set-up. An inverted microscope coupled with a colored CCD and EMCCD. A set of acousto-optic tunable filters are installed to allow one wavelength to reach the EMCCD at a time. (b) picture of the apparatus.

There were three types of light source used in this study. The conventional light source installed in this set-up is a halogen lamp. The intensity of the conventional light source is not strong enough to resolve very small particles. The second type of the light source was the super-continuum white light source generated from a pulsed laser. In this configuration, the Tsunami femto-second laser is pumped by a 532nm green CW laser. The pulsed laser passes through a photonic crystal fiber, which generates a super-continuum white light source, whose spectrum is dependent upon the power and the wavelength of the pulsed laser. There were some background issues associated with the super-continuum white light source. An axicon lens was installed when using the super-continuum source to further minimize the photon loss. The third type is a Xe light source from Nikon. It is brighter than the halogen lamp, and has higher intensity at bluer wavelengths.

The raw data contains a series of tiff files (100 frames was often used). The exposure time of each frame can be customized within a software called “LightField”. For static particles, longer exposure for each frame will give spectra with higher signal to noise ratio. However, for moving particles, shorter exposure time is preferred, in order to obtain reasonable diffusion trajectories. 0.033s of exposure is the limit of the acousto-optical tunable filters, and it is often used in the diffusional studies.

The spectra of the single particles need to be processed from the raw data. The spectra can be written as,

$$Spectrum = \frac{Raw\ Date - Background}{Lamp - Dark} \quad (3.3)$$

where *background* is the spectrum collected at a position without any particle scattering at the same acquisition conditions. *Lamp* is the ‘lamp profile’ of the light source, which is the lamp intensity as a function of wavelength. *Dark* is dark signal from the detector dark current. The *Lamp* and *Dark* spectra have to be acquired with the same parameters, but they may be different from those of the particle and background spectra. Raw particle spectra and the background spectra were collected when the NA of the objective is at the minimum. The NA has to be opened when collecting the *Lamp* and *Dark* spectra. Most of the time, the NA was not completely open to avoid saturating the CCD camera. The parameters were set to exposure = 0.033s and frame = 100.

The original MATLAB code for data analysis was written by Dr. Katherine Willet. I’ve modified the code for version later than MATLAB 7. The input parameters include acquisition wavelength, wavelength step and the time step of the data, as shown in Figure 3.5 (a). Three

moving particles and their corresponding spectra and mean square displacements are shown in Figure 3.6.

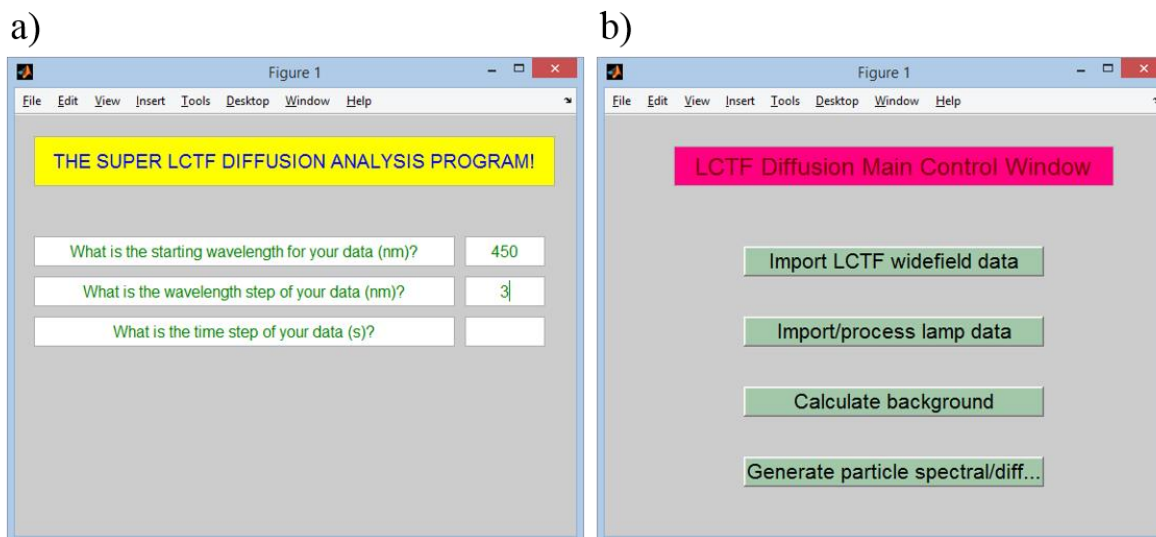


Figure 3.5 The GUI window made by the MATLAB code. (a) The input parameters include the starting wavelength, wavelength step and the time step of the data, and (b) shows the procedure of particle spectra generation

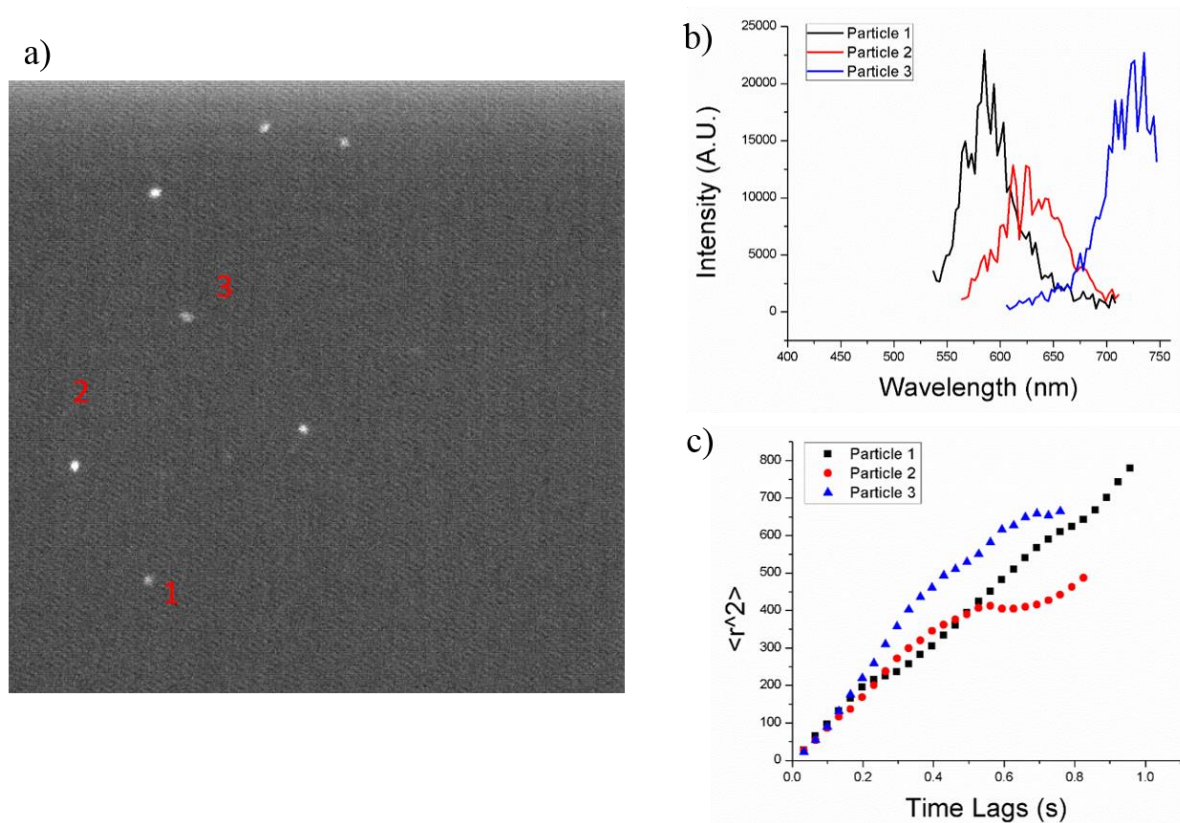


Figure 3.6 (a) One sample frame out of the 100 frames acquired by EMCCD. (b) LSPR spectra of three particles labeled in (a), and (c) the corresponding mean square displacements of these three particles

### 3.5.1 *In situ* Monitoring of Diffusional Particle Growth

Owing to the shallow depth of field of the 100x oil immersion objective lens, a very thin liquid cell is required to avoid losing the particle of interest. The liquid cell is composed of a glass slide, a 12.5  $\mu\text{m}$  Teflon spacer (also act as o-ring, purchased from Lebow), and a No.0 coverslip. The schematic of the liquid cell is shown in Figure 3.7. The No.0 coverslip was taped onto the glass slide to further avoid leaking.

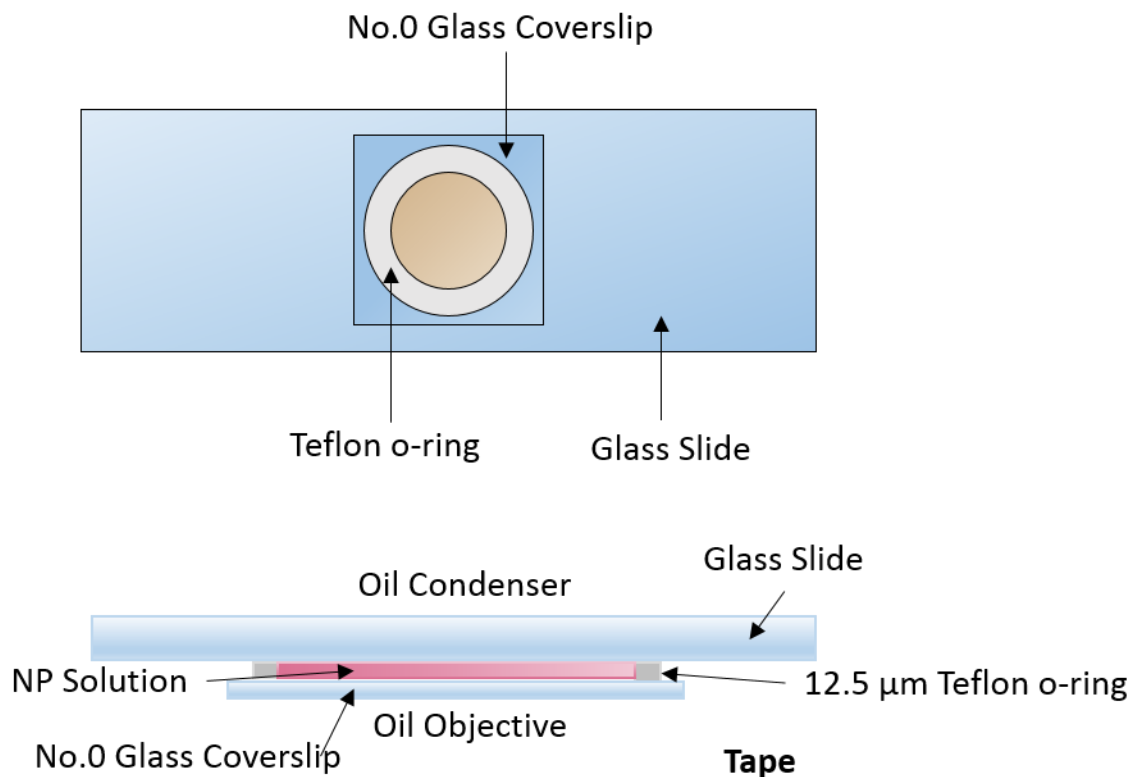


Figure 3.7 Schematic of the thin liquid cell

The standard cleaning steps for glass slides and coverslips include (a) clean with piranha solution for 30 min (b) rinse with milliQ water (c) clean the glass with base treatment with sonication for 60 min (d) rinse with milliQ water. The piranha solution is a 3:1 mixture of concentrated sulfuric acid and hydrogen peroxide. The solution for base treatment is a mixture of water, ammonium hydroxide and hydrogen peroxide, with a volume ratio of 5:1:1. For diffusion experiments, the glass was only sonicated in isopropyl alcohol (IPA) for 60 mins to avoid particles sticking onto the glass too quickly. The glass cleaned with the standard method will be negatively charged, and the positively charged particles will stick unto the glass instantly.

The particles moves in approximately 2D around the center of the cell, owing to the pressure from the objective. The particles around the Teflon o-ring still move in 3D. Areas around the center of the cell were chosen to be the areas of interest.

### **3.5.2 *In situ* Monitoring of Stationary Particle Growth**

In order to monitor the same particle over a long time, particles were immobilized onto conductive transparent substrate, i.e. a glass coverslip coated with a thin film of indium tin oxide (ITO). The particles on the conductive substrate can be characterized using SEM after the growth experiment. A distinct pattern was etched onto the ITO surface to facilitate identification of the same location when measuring the particles using both the WF set-up and SEM.

The ITO substrate was cleaned by sonication in IPA for 50 min, followed by rinsing with IPA and H<sub>2</sub>O. The plate was base treated for 10 minutes and heated at 60°C to functionalize the surface with hydroxyl (-OH) group. The plate was rinsed with H<sub>2</sub>O and IPA multiple times before it was transferred to a solution of IPA (50mL) and (3-mercaptopropyl) trimethoxysilane (0.5mL) for 6-10 minutes and heated at 70°C. The ITO substrate was then rinsed with IPA and dried with N<sub>2</sub>. 130 μL of nanoparticle seed solution was transferred to the functionalized ITO surface and it was allowed to be dried for 40 min in a N<sub>2</sub> box to prevent oxidation of the nanoparticles. The ITO surface was rinsed with water and dried with N<sub>2</sub>.

A 3D-printed liquid flow cell was used and the design of the cell is illustrated in Figure 3.8.

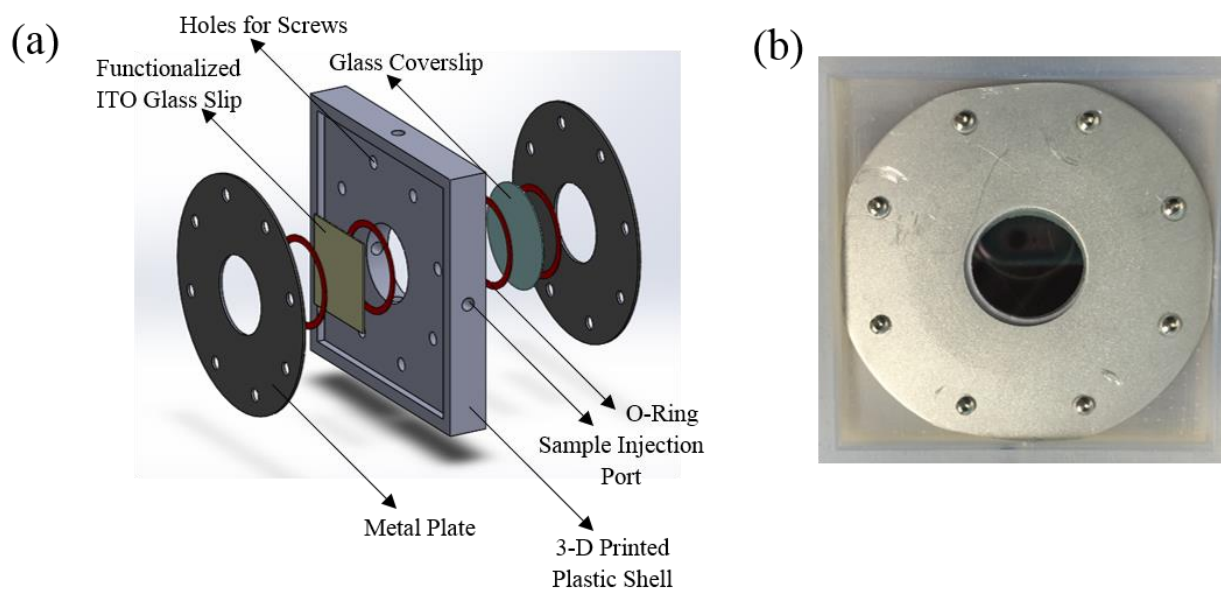


Figure 3.8 (a) Design of the liquid flow cell and (b) the picture of the assembled cell. Photo courtesy by Meaghan Bruening

The experimental methods introduced in this chapter will be utilized in the following chapters.

## CHAPTER 4

# **Compositional Gradient and Corner Enrichment of Pt in Pt/Pd Bimetallic Nanoparticles and Size-independent Corner Rounding in Nanoparticles**

## 4.1 Introduction

Metal nanoparticles are of interest, owing to their unique optical, electronic, and catalytic properties, which are different from their bulk counterparts, and they are widely used in various applications.[2, 3, 31] Their unique physical and chemical properties are dependent on their size, structure, and composition. [108-111] Changes in composition enable the tuning of physical and chemical properties of these particles. For instance, bimetallic nanoparticles offer distinct activities and selectivity that are different and often better than those of their monometallic counterparts. [46, 112, 113]

Understanding the thermodynamics and kinetics during growth and how they affect the final shape and composition profile of the nanoparticles is important. In this chapter, the concentration profile of Pd/Pt bimetallic multiply twinned particles is analyzed. A gradual increase of Pt concentration from the center to the outermost surface of the particle and an enrichment of Pt concentration at the particle corners were observed. I first demonstrate that the smooth compositional gradient is a result of Pt and Pd having different growth rates via analytical modeling. Then, it is shown that the corner concentration is related to the weighted mean curvature (chemical potential) of the corner, which correlates the corner concentration of Pt with the chemical potentials of Pt and Pd in solution. Size-independent corner rounding is also discussed in this chapter. The rounded corner is a Lyapunov steady-state solution of the growth, and corner rounding can be used as an indicator of the chemical potential of the species in the growth solution. The analyses in this chapter are not simply qualitative models. Instead, they are relatively rigorous quantitative analyses of the composition and corner rounding as a function of growth conditions.

These growth models can serve as bases for improved reproducibility of nanoparticle syntheses for various applications.

The Pt/Pd alloy multiply twinned particles were synthesized by a co-reduction method.[114] Composition profiles of the Pt/Pd particles were acquired by energy dispersive x-ray spectroscopy (EDX). Synthesis of anisotropic Au multiply twinned particles with different shapes was performed via the modification of a one-pot polyol synthesis.[115]

## 4.2 Methods

Synthesis of Pt/Pd alloy multiply twinned particles was performed via a method developed by Lim *et al.*[114] Based on the original synthesis, the ratio of Pt and Pd precursors was modified to yield Pt/Pd alloy multiply twinned particles with different overall concentrations and different degrees of Pt corner enrichment. Poly(vinyl pyrrolidone) (PVP,  $(C_6H_9NO)_n$ ; MW = 55000, from Sigma-Aldrich) was dissolved in 16 mL of deionized water, and the solution was heated to 80 °C in air. Different molar ratios of sodium tetrachloropalladate (II) ( $Na_2PdCl_4$ ) and potassium tetrachloroplatinate(II) ( $K_2PtCl_4$ ) were dissolved in 6 mL of deionized water at room temperature. For a 1:1 molar ratio solution with 100% PVP, 0.032 mmol of  $Na_2PdCl_4$ , 0.032 mmol of  $K_2PtCl_4$  and 70 mg of PVP were used. The  $Na_2PdCl_4$  and  $K_2PtCl_4$  solution was added to the PVP aqueous solution, and the solution was heated at 80 °C for 18 h in air.

The Pd/Pt nanocrystals were washed five times with deionized water and drop-casted onto ultrathin carbon grids (Ted Pella). The morphologies of the synthesized particles were characterized using a JEOL JEM-2100F field emission TEM and high-angle annular dark field (HAADF) imaging in an aberration-corrected JEOL JEM-ARM200CF S/TEM. The elemental distributions within the particles were characterized via EDX using both a Hitachi HD-2300 STEM

and a JEOL JEM-ARM200CF S/TEM. An *in-situ* heating experiment was performed in the JEOL JEM-2100F microscope.

Synthesis of multiply twinned Au nanoparticles with different shapes was performed via the modification of a one-pot polyol synthesis,[116] where different concentrations of PVP were used to yield particles with different sizes. For larger particles (65-120 nm), 2 g of PVP (MW 55000g/mol) was dissolved in 25 ml diethylene glycol (C<sub>4</sub>H<sub>10</sub>O<sub>3</sub>). The solution was refluxed at 255 °C for 10 mins. 20 mg HAuCl<sub>4</sub>•3(H<sub>2</sub>O) was dissolved in 2 mL diethylene glycol and then added rapidly to the solution. The mixture was allowed to reflux for 10 more mins. The reaction was quenched using a cold water bath, and the particles were washed with ethanol. This synthesis was carried out by Deniz Alpay.

The spatial resolution of EDX depends on the acceleration voltage of the microscope as well as sample thickness and geometry. In this study, EDX maps were acquired using a Hitachi HD 2300 STEM and a JEOL JEM-ARM200CF S/TEM, both operated at an acceleration voltage of 200 kV, which is rather high. Because the sample was very thin, the interaction volume was very small. This was confirmed by standard Monte Carlo simulations. The compositions quantified from EDX spectra are 2D projections of the 3D elemental distributions in the particles. Quantification was done using the Cliff-Lorimer method.

### 4.3 Results

The product of the Pt/Pd synthesis includes a variety of multiply twinned particles, such as truncated/untruncated bipyramids, Marks decahedra, Icosahedra, and hexagonal platelets. The TEM and HAADF images of as-synthesized particles are shown in Figure 4.1.

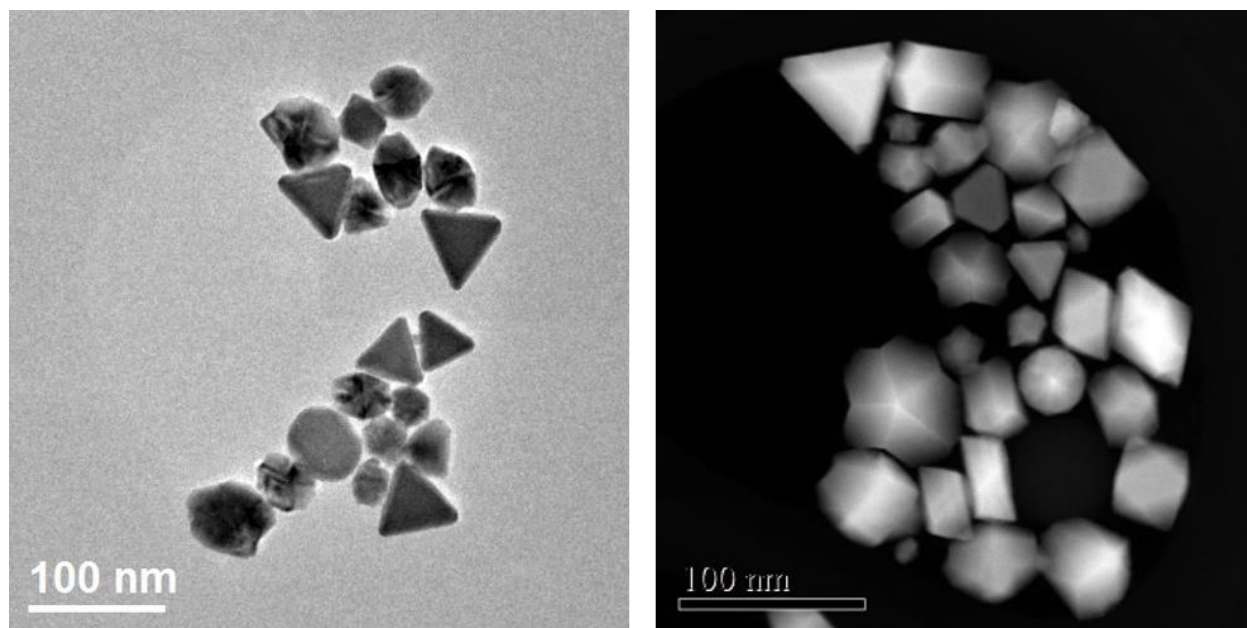


Figure 4.1 TEM and HAADF images of Pt/Pd multiply twinned particles made by 1:1 molar ratio of Pd and Pt precursors

EDX line scans taken from the corner to the bulk of a particle and between two corners of a particle indicate Pt enrichment at the surface, and especially at the corners. Figure 3.2 shows composition profiles as a function of distance from the center to the surface of particles synthesized with different amounts of precursors. Modeled functions are also included in Figure 4.2, which are discussed in Section 4.3.1. In Figure 4.3, 2D EDX maps of particles synthesized using a 1:1 molar ratio of Pt and Pd precursors are shown. An additional increase in Pt concentration at corners was observed. This corner enrichment was observed in more than 50 different particles and is reproducible.

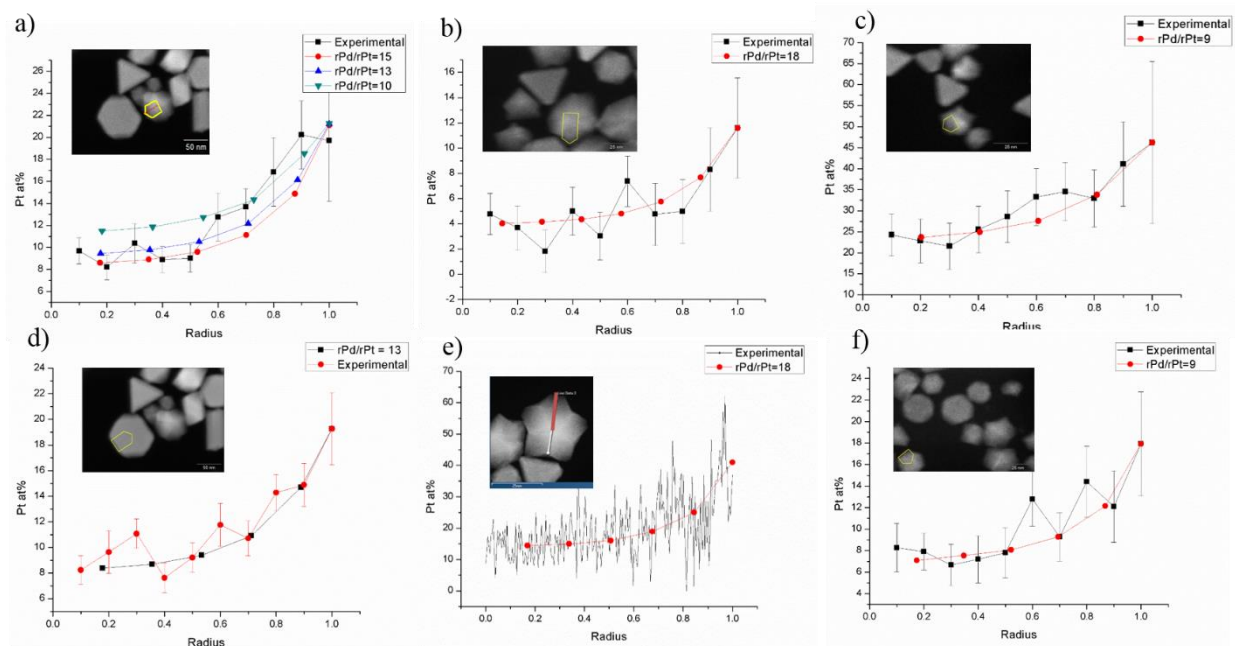


Figure 4.2 Measured composition profiles and calculated 2D projections as a function of distance from the center to the surface of particles. (a) The composition profile of a Dh fitted with different  $r_{Pd}(T)/r_{Pt}(T)$  ratios; (a) and (b) are composition profiles of a particle synthesized with a 1:1 molar ratio of Pd and Pt precursors. (b) Composition profile of a particle synthesized with a double amount of Pd. (e) Composition profile of a particle synthesized with a double amount of Pt. The composition profiles of particles in (b) and (e) have the same  $r_{Pd}(T)/r_{Pt}(T)$  ratio. (c) Composition profile of a particle synthesized with half of the amount of Pd. (f) Composition profile of a particle synthesized with half of the amount of Pt. The composition profiles of particles in (c) and (f) have the same  $r_{Pd}(T)/r_{Pt}(T)$  ratio.

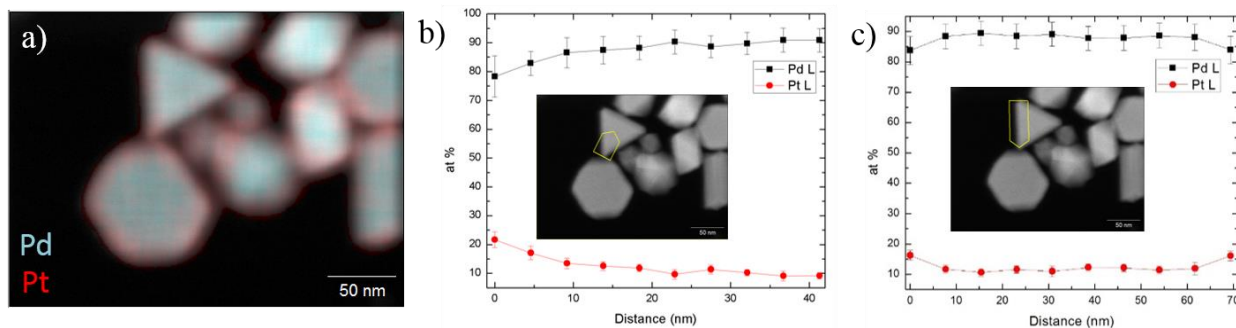


Figure 4.3 EDX measurements showing the surface and corner enrichment of Pt in Pt/Pd bimetallic nanoparticles. (a) The EDX elemental maps of the Pd/Pt multiply twinned particles. (b) A EDX line scan from the corner to the center of a particle (c) A EDX line scan between two corners of the sample particle.

### 4.3.1 Model for Radial Concentration Change

The shape of nanoparticles with facets can be described in terms of either surface energy (thermodynamic Wulff construction) or growth rate (kinetic Wulff construction). Here, a model developed based on established methods that account for the concentration profiles will be described. As shown in Figure 4.2 and Figure 4.3, the Pt concentration increases toward the surface. There are three possible explanations for this, and they are analyzed in this section.

The simplest possibility is that the nanoparticles were in their thermodynamic stable forms, and the surfaces were covered with the element with lower surface energy. It is well-established that surface energy can play an important role in determining the surface composition in alloy systems. [57, 96, 117, 118] Williams and Nason have developed a model based on thermodynamics, aiming to predict surface segregation. They minimized the surface energy by allowing atoms to exchange between surface layers and the bulk and suggested that within four atomic layers, the composition became constant. [119] They also analyzed the effect of chemisorption and size, and further compared the model with experimental results. [120-122] The same method has been used for predicting the surface segregation in Au/Ag bimetallic nanoparticles. [123] There are more recent studies showing that in nanoparticle systems, the surface composition can be altered by chemisorption. [113, 124-126] In the Pt/Pd system, there are experimental and computational results showing that Pd tends to segregate to the surface. [125, 127, 128] According to the alloy Wulff construction, there is a balance between a decrease in surface energy and an increase in bulk energy, which prevents the full surface segregation of a species. In this case, there would be a

surface segregation (complete or incomplete) on a homogeneous bulk alloy nanoparticle. This is not consistent with the present experimental results.

The second possibility is that the concentration gradients were the result of inter-diffusion within the particles. Kirkendall voids [129-131] are indicators of inter-diffusion, but they were not observed in these particles. Furthermore, an *in-situ* heating experiment was conducted to verify that inter-diffusion was not significant in this synthesis. The sample was heated up and remained at 700 °C for 90 min in an electron microscope. There was no evidence of any additional surface segregation or change in the composition, indicating that inter-diffusion was not dominant even at such high temperatures. Because the synthesis was conducted at a much lower temperature (80 °C), it is unlikely that these concentration gradients were a consequence of inter-diffusion during synthesis.

The third possibility is that the concentration gradient was due to growth kinetics, instead of segregation within the particle. Because the amounts of both Pt and Pd in solution was finite, this would lead to a gradual change in the composition, which is consistent with the experimental data. There are similar existing models that proposed this type of model in literature. For instance, Ahrenstorf *et al.* studied the formation mechanism of Ni/Pt bimetallic nanoparticles and demonstrated that Pt and Ni precursors were consumed at different rates. [132] Choi *et al.* studied the mechanism of formation of Pt/Ni octahedral particles and demonstrated control of the composition by varying the amount of solvent, precursors, and surfactant added. The concentration of Pt was richer at the edges and vertices than that at the center, which suggests that the amine group in oleylamine could coordinate with Pt(acac)<sub>2</sub> in the initial stage of the synthesis. [133] The quantitative comparisons are lacking, so a quantitative model will be discussed in this section.

For this particular synthesis, PVP was used as the reducing agent. As  $\text{PdCl}_4^{2-}$  and  $\text{PtCl}_4^{2-}$  were reduced to Pd and Pt monomers, the nucleation stage began, followed by the growth of nuclei that had reached a critical size. The final products had well-defined shapes, suggesting that the growth was interface-controlled and therefore may be described in terms of kinetic Wulff model. [54, 64, 134] In the kinetic Wulff model, on the atomic scale, monatomic terraces nucleate on an existing flat surface, followed by the growth of this terrace across the facet. According to classical nucleation theory, the free energy of terrace formation is negative, so the growth of nucleated monatomic terraces would be spontaneous and fast. The schematic of interface-controlled growth is shown in Figure 4.4 (a), where the rate limited step is where atoms move from region II to region III.

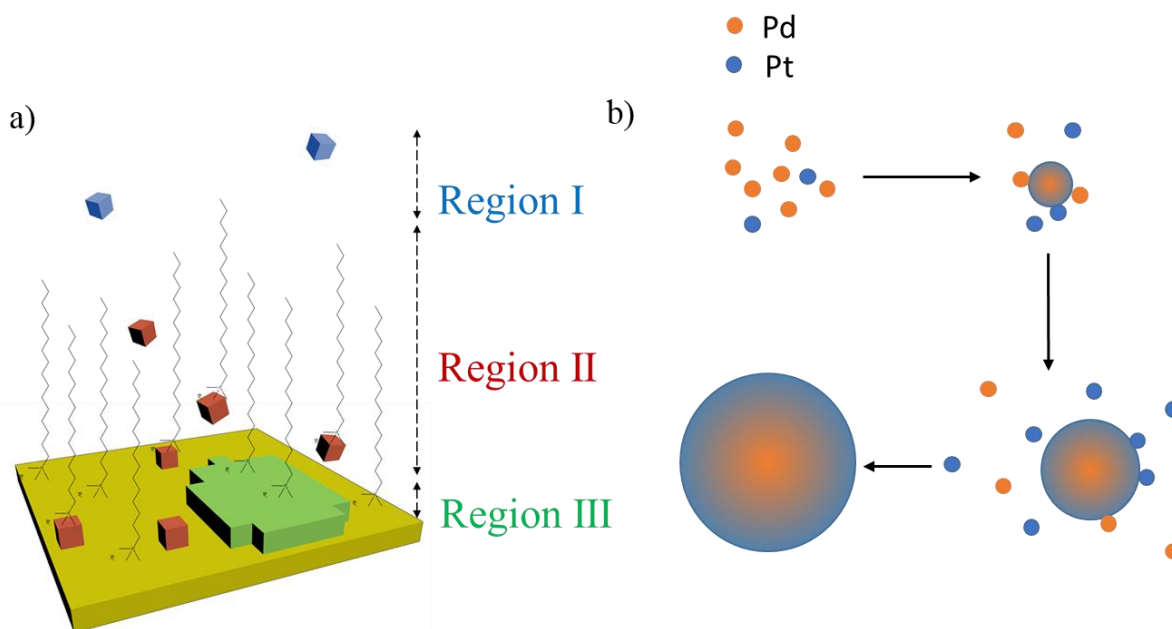


Figure 4.4 Schematics of nanoparticle formation. (a) The regions for kinetic growth. Region I contains external Pt and Pd atoms that are reduced by PVP. Region II is the region where Pt and Pd atoms diffuse to the terrace and region III is a nucleating terrace. (b) Schematic explaining the origin of the concentration gradient. The Pd atoms attach to the surface faster than that of Pt atoms. As growth proceeds, Pd atoms are consumed faster than Pt atoms and more Pd is deposited near the surface of the particles.

In order to model the concentration profile quantitatively, the formation of nanoparticles was separated into two steps – the reduction of precursors and the growth of nanoparticles – because the reduction and growth were on two different time scales. The time  $t$  used in this model had to be separated for these two steps. The effect of having a different nucleation period will be discussed later in this section.

The Pd concentration was higher in the cores of the synthesized particles and gradually decreased toward the particle surfaces. This indicated that the deposition rate of Pd was higher than that of Pt, assuming that the surface diffusion is much slower than the deposition rate (kinetic Wulff). The deposition rate had contributions from both the reduction of precursors and deposition of reduced monomers.

When the particles reached the critical nucleus size, they became relatively stable and started to grow. During growth, the reduced Pt and Pd atoms in the supersaturated solution were deposited onto the nanoparticle surface. The reduction rates can be written as

$$r(Pd) = k_{Pd}(T)[PdCl_4^{2-}][PVP]^2 \quad (4.1)$$

$$r(Pt) = k_{Pt}(T)[PtCl_4^{2-}][PVP]^2 \quad (4.2)$$

where  $r(Pd)$  and  $r(Pt)$  are the reaction rates of the reduction of Pd and Pt precursors, respectively;  $k_{Pd}(T)$  and  $k_{Pt}(T)$  are the reaction rate constants, which are dependent of temperature but independent of reactant concentrations;  $[PdCl_4^{2-}]$  and  $[PtCl_4^{2-}]$  are the concentrations of Pd and Pt precursors. Since the reaction temperature was held constant during the reaction,  $k_{Pd}(T)$  and  $k_{Pt}(T)$  are assumed to be constant for this synthesis and will be written as  $k_{Pd}$  and  $k_{Pt}$ .

The reaction rate constants can be written in an Arrhenius equation form, as shown in Equation 4.3 below. In order to calculate the ratio between  $k_{Pd}$  and  $k_{Pt}$ , the simple collision model was used as an approximation.

$$k = A e^{\frac{-E_a}{RT}} \quad (4.3)$$

where  $k$  is the reaction rate constant;  $E_a$  is the activation energy,  $R$  is the gas constant, and  $T$  is the reaction temperature.  $A$  is the pre-exponential factor which can be written as,

$$A = Z \cdot \rho = \rho \cdot N_A \sigma \sqrt{\frac{8k_B T}{\pi \mu}} \quad (4.4)$$

where  $\rho$  is a steric factor, and  $Z$  is the collision frequency, which can be written as:

$$Z = N_A \sigma \sqrt{\frac{8k_B T}{\pi \mu}} \quad (4.5)$$

where  $N_A$  is Avogadro's number,  $\sigma$  the reaction cross section,  $k_B$  the Boltzmann constant,  $T$  the temperature in Kelvin, and  $\mu$  the reduced mass of the reactants. The reaction rate constant ratio between Pd and Pt precursors is:

$$\frac{k_{Pd}}{k_{Pt}} = \frac{A_{Pd}}{A_{Pt}} \exp\left(\frac{-(E_{Pd}^a - E_{Pt}^a)}{RT}\right) = \frac{\rho_{Pd} N_A \sigma_{Pd} \sqrt{8k_B T / \pi \mu_{Pd}}}{\rho_{Pt} N_A \sigma_{Pt} \sqrt{8k_B T / \pi \mu_{Pt}}} \exp\left(\frac{-(E_{Pd}^a - E_{Pt}^a)}{RT}\right) = 1.0349$$

where the activation energy is the energy required to break Pd-Cl and Pt-Cl bonds in the precursor molecules. The steric factor was assumed to be similar for  $\text{PdCl}_4^{2-}$  and  $\text{PtCl}_4^{2-}$  because they have similar structures. It is worth mentioning that the reaction was solution based, therefore more than

one collision could happen in one encounter due to the cage effect. This could lead to a steric factor greater than 1.

The above calculation is accurate for an activation-controlled reaction. If the reaction was diffusion-controlled instead, the reaction rate constant would be dependent upon the diffusion rate, where the diffusion rate constant is defined as  $k_d = 8RT/3\eta$ , where  $\eta$  is the viscosity of the solution. The reaction rate constant ratio between Pd and Pt precursors would be 1, which is very close to the value calculated from the activation-controlled reaction based on collision model. Therefore, in the real system, the Pd and Pt precursors were reduced at a similar rate. In this model, the ratio  $k_{Pd}/k_{Pt} = 1.035$  was used in calculation.

To compare the calculated results with experimental results, three-dimensional concentration profiles were calculated based on the reaction kinetics outlined above, assuming spherical particles. The composition of Pt was numerically integrated as a function of distance along the beam direction (to match with the projected EDX measurements). The  $r_{Pd}(T)/r_{Pt}(T)$  ratio was adjusted to obtain reasonable fits to the experimental data. We found that the ratio obtained from the best fits varied with the total amount of precursors added during synthesis, and it was independent of the ratio between Pt and Pd precursors added. The  $r_{Pd}(T)/r_{Pt}(T)$  ratio is plotted as a function of the sum of Pt and Pd precursors in Figure 4.5. The  $r_{Pd}(T)/r_{Pt}(T)$  was kept constant for different syntheses by halving the amount of added Pd precursors (Pd/Pt precursor = 1:2) or by halving the amount of Pt precursors (Pd/Pt precursor = 2:1). Doubling the amount of one of the precursors and keeping the other constant resulted in the same  $r_{Pd}(T)/r_{Pt}(T)$  value. As the total precursor concentration increased, the  $r_{Pd}(T)/r_{Pt}(T)$  ratio would increase.

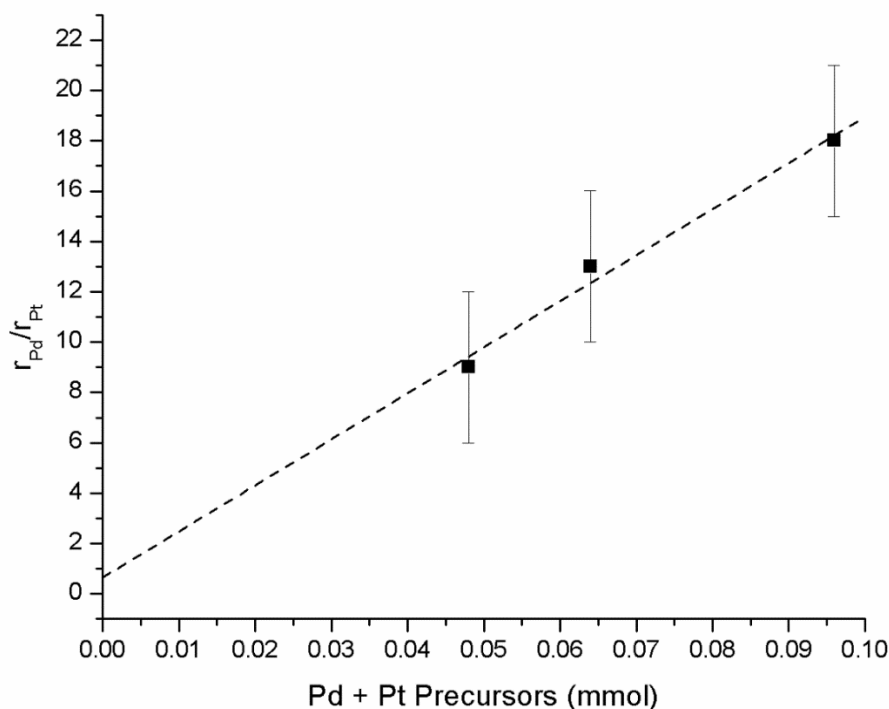


Figure 4.5  $r_{Pd}(T)/r_{Pt}(T)$  as a function of the total amount of Pd and Pt precursor concentration

The deposition rate  $R_{Pd}(T)$  and  $R_{Pt}(T)$  are proportional to the product of the deposition rate constants  $r_{Pd}(T)$  and  $r_{Pt}(T)$ , and the concentration of Pd and Pt monomers reduced from the precursors, respectively. Based on what was observed, Pd had a higher deposition rate and was deposited faster than Pt, resulting in a Pd-rich core. As growth proceeded, Pd atoms were consumed faster than Pt, and more Pt was deposited near the surface of the nanoparticles, which created a concentration gradient inside of the particle. This is illustrated in Figure 4.4 (b).

The concentration profiles depend on both the reduction and deposition rates of Pd and Pt as well as the incubation time (the nucleation period). The incubation period and the ratio between the reduction and deposition rates were determined to have minimal effects on the concentration profiles. The incubation period depended on the chemical potentials of Pt and Pd atoms in solution. By changing the incubation time from 10 time steps to 1000 time steps, the concentration profiles

from the center to the surface changed slightly, and these are plotted in Figure 4.6. The incubation time shows minimal influence on the concentration profiles.

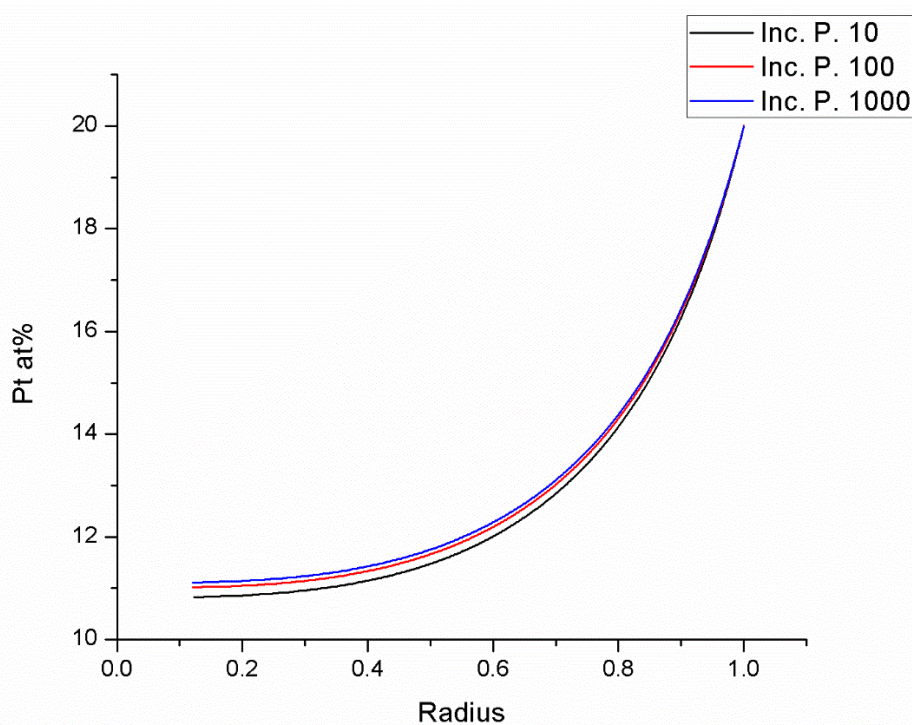


Figure 4.6 Pt concentration profiles as a function of distance from the center to the surface (0 represents the center of the particle, and 1 represents the surface of the particle), calculated with different incubation steps

Here, the effect of changing the ratio between reduction and deposition rate constants,  $r_{Pd}/k_{Pd}$ , is discussed. The concentration profiles from the center of the particle to the surface, calculated with different  $r_{Pd}/k_{Pd}$  are plotted in Figure 3.7. When  $r_{Pd}/k_{Pd} = 100$ , there was a very small discrepancy in the concentration profile, however, it was not likely to be the case because the growth would be diffusion-controlled if the deposition rate was much higher than the flux of atoms coming towards the particle surface, which depended upon the reduction rate of the precursors.

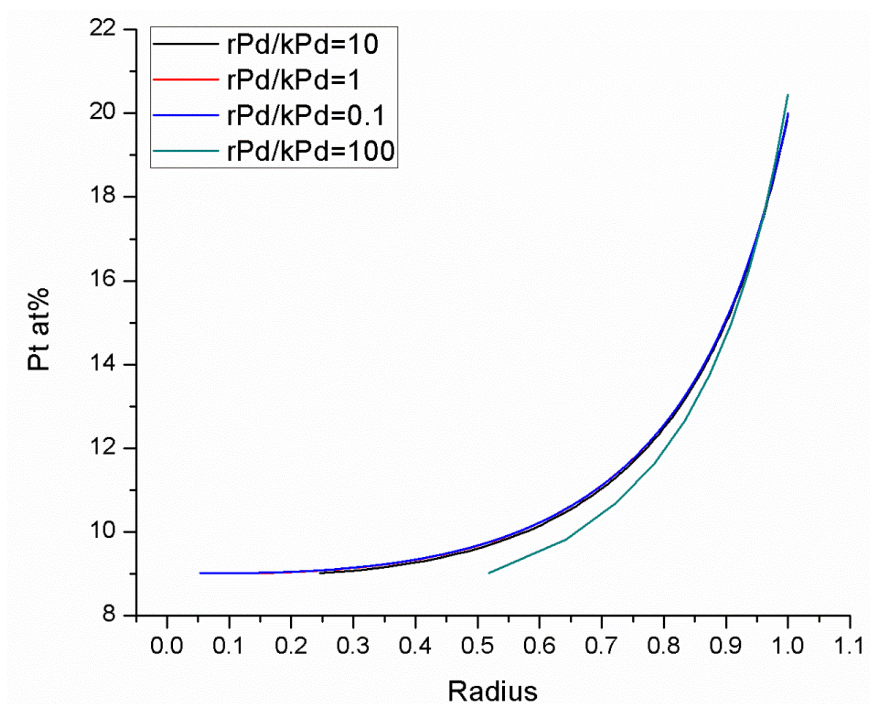


Figure 4.7 Pt concentration profiles as a function of distance from the center to the surface (0 represents the center of the particle, and 1 represents the surface of the particle) calculated with different ratios between deposition and reduction rate constant  $r_{Pd}/k_{Pd}$ .

As mentioned above, the shape of the particles was assumed to be spherical, but this was not the case in the real synthesis. When the  $r_{Pd}(T)/r_{Pt}(T)$  ratio of truncated bipyramids and Marks decahedra synthesized under the same conditions were compared, they appeared to be similar. The results obtained from fitting the data with a spherical model might differ from the real  $r_{Pd}(T)/r_{Pt}(T)$  ratio, but it was consistent between two dominant shapes.

### 4.3.2 Corner Rounding

The EDX maps showed that the Pt concentration was higher at the corners than that on the surface. In order to explain this phenomenon, the concept of corner rounding will be discussed in this section. There are classic models for understanding the structures of nanoparticles, such as the Wulff construction for free-standing single crystals, the modified Wulff construction for particles

with twins involved, the kinetic version of the Wulff and modified Wulff constructions, and the Winterbottom construction when substrates are introduced. These models can predict nanoparticle shapes at a fairly accurate level. However, in these models, sharp corners and edges were considered, but in many cases, such as plasmonics, a small difference in corner rounding can have large effects. [1, 135]

Rounded corners are often observed experimentally, and there is a need to develop a model to understand particles with corners and edges that are not sharp. Within a continuum model, the chemical potential of a sharp corner can be understood in terms of the weighted mean curvature (wmc), [136] a limit similar to a functional derivative of the total surface energy  $E_S$  with respect to  $h_i$ , the normal distance to the facet,

$$wmc(h_i) = \lim_{\delta \rightarrow 0} \Delta E_S(h_i + \delta h_i) / \Delta V(h_i + \delta h_i) = \mu^s(h_i) / \Omega_0 \quad (4.6)$$

where  $\mu^s(h_i)$  is the chemical potential associated with a given facet  $i$  as a function of  $h_i$ , and  $\Omega_0$  is the atomic volume. For a simple corner, as illustrated in Figure 3.8, the chemical potential at the apex can be written as,

$$wmc(h_i) = \bar{\gamma}_i / (L_i - h_i) \quad (4.7)$$

where  $L_i$  is the distance from the Wulff center to the apex and  $\bar{\gamma}_i$  is the weighted mean surface energy. The facet disappears when  $h_i \geq L_i$ . The wmc is inversely related to the distance of a truncation facet from the apex, so it is nominally singular for a sharp corner. However, the validity of this continuum model at the atomistic scale needs to be verified. It can be verified by density functional theory (DFT) calculations, and the DFT calculated chemical potential in the limit of small sizes is plotted in Figure 3.8(b). The DFT calculations were performed using the all-electron APW+lo WIEN2K code [137] for a simple gold pyramid with P4/mmm symmetry as a function

of truncation using the Wu and Cohen GGA functional.[138] The calculations were carried out by Professor Laurence Marks.

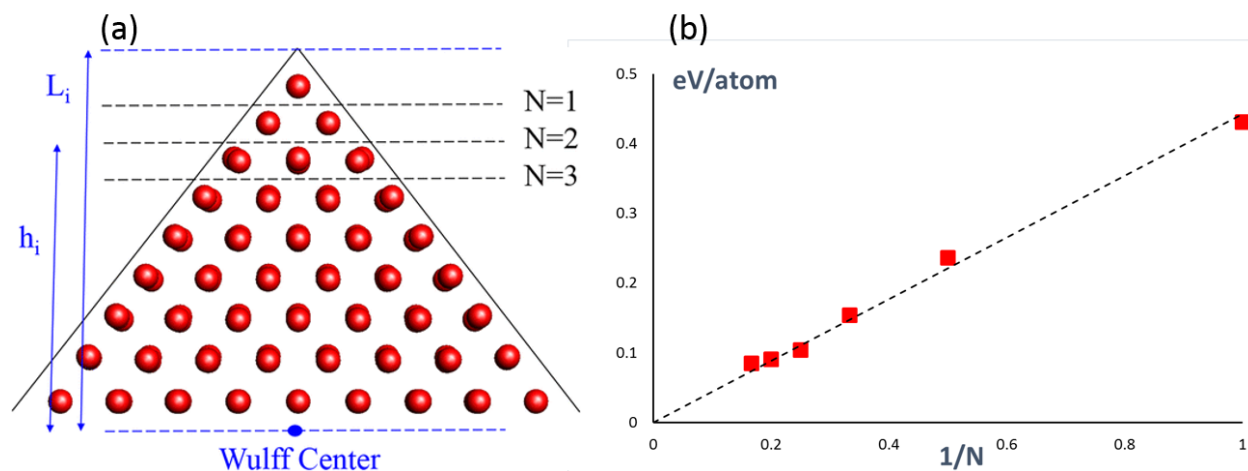


Figure 4.8 (a) Illustration of truncation of a (001) facet for different numbers of planes ( $N$ ) to take account of atomicity, with the corresponding equimolar surfaces and facet length shown.  $L_i$  is the distance normal to the facet from the Wulff center to the apex, while  $h_i$  is the distance from the Wulff center to the facet shown for  $N=2$ . (b) The chemical potential in eV/atom vs.  $1/N$ , calculated using DFT.

From the DFT calculations, inverse scaling between the chemical potential and the distance  $L_i-h_i$  was observed, and within numerical accuracy, this scaling matched very well to the continuum expectation. Therefore, we can apply the continuum wmc formulation without any concerns about its validity for small sizes.

The synthesis of anisotropic Au nanoparticles with different shapes was performed by Deniz Alpay via the modification of a one-pot polyol synthesis [115], using different concentrations of PVP to yield different size particles. In this study, the corner rounding of decahedral multiply-twinned nanoparticles (Dh) and truncated bitetrahedra (BTd) were analyzed. Several examples of these are shown in images in Figure 3.9. Note that in both cases, each corner had a twin boundary with a vector normal either perpendicular or parallel to the viewing direction

for the Dh and BTd particles, respectively. The size of the nanoparticles decreased as the concentration of PVP increased. The corner rounding plotted as a function of edge length of both Dh and BTd particles is shown in Figure 4.10a. The rounding as a function of particle size synthesized using three different concentrations of PVP (MW  $\approx$  55000 g/mol), with a wider size range, is plotted in Figure 4.10b. While the corner rounding data was more scattered at larger sizes, the rounding was very close to constant over the total range.

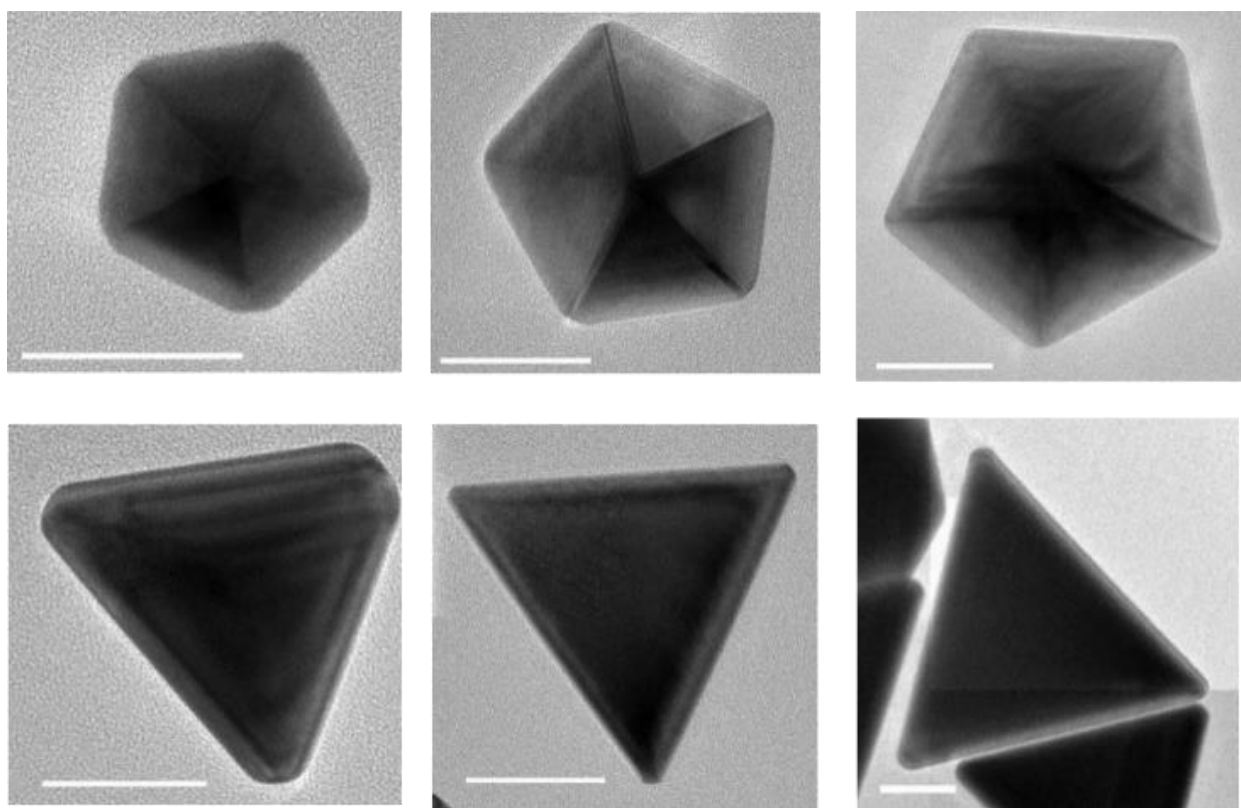


Figure 4.9 Transmission electron microscope images of different Dh (top) and BTd (bottom), with scale bars of 50 nm.

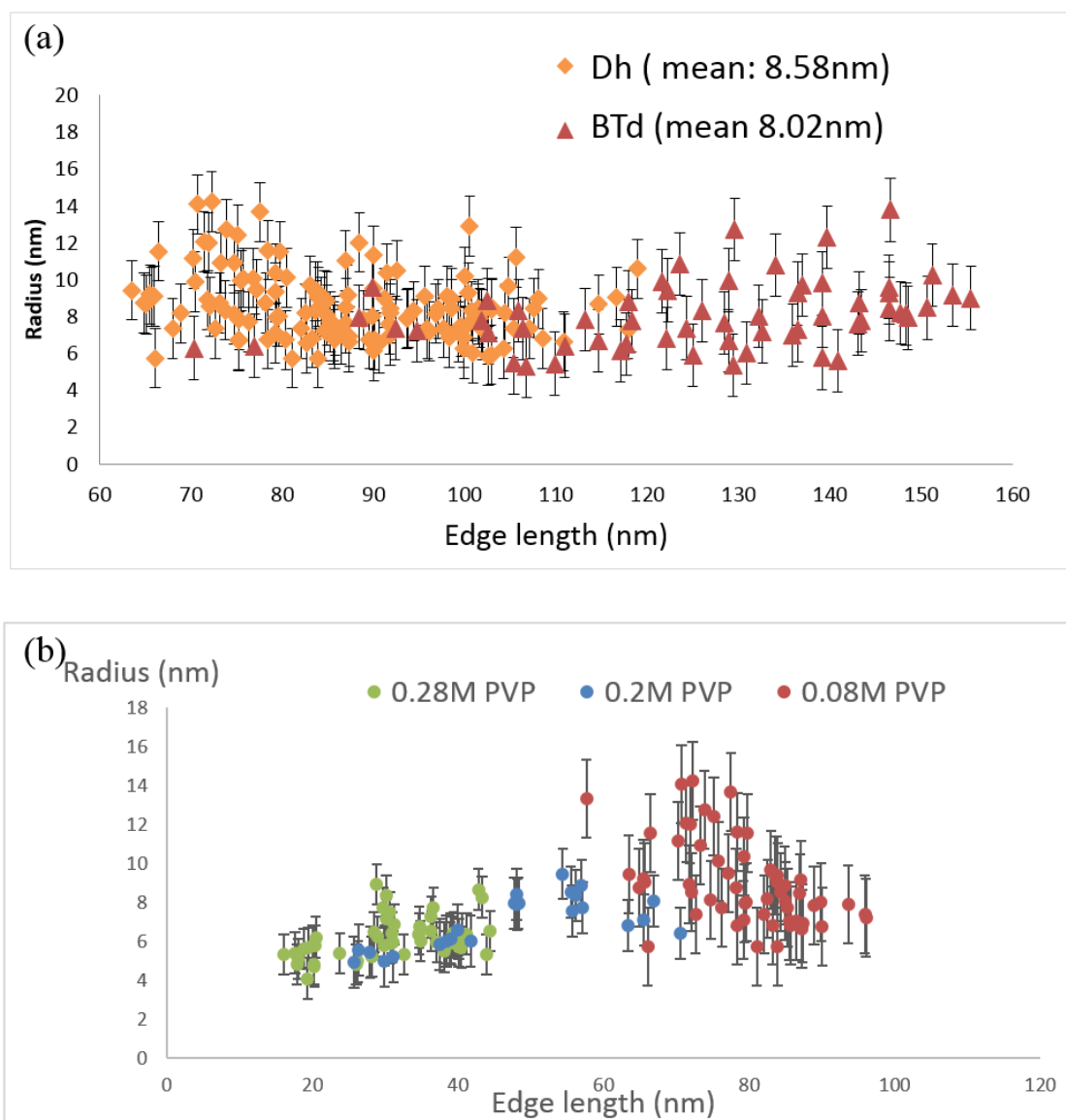


Figure 4.10 In a) measurements of Dh and BTd particles from a synthesis using 2 g PVP, and in b) measurements for Dh particles synthesized using different concentrations of PVP.

The thermodynamic minimum energy shape at a twin has a re-entrant surface. [11, 139] However, there could be faster growth at the twin boundary caused by faster nucleation at the twin. This is because the nucleation barrier at the twin is only half of the energy required to nucleate a terrace on a flat surface. [140] The thermodynamic shape is a shape with (100) re-entrant surfaces

at twin boundaries (Marks decahedra). Fast growth at twin boundaries is important for yielding the perfect decahedra with no re-entrants at the corners. DFT calculations, carried out by Prof. Laurence Marks, were used to clarify the preferential nucleation at the twins. Three simple systems of a long surface slab of size  $41.6955 \text{ \AA} \times 39.3109 \text{ \AA} \times 2.833 \text{ \AA}$  composed of Al were calculated as shown in Figure 3.11, with case a) without any surface steps, case b) with 4 steps per unit cell and case c) with 2 steps and 2 terminations at a twin boundary. Bulk Al and a reference Al (111) surface were also calculated. All calculations were performed at the DFT relaxed lattice parameters. Since the number of surface atoms were the same for all three cases, by subtracting the bulk energy, both the step energy and the energy for termination at a twin were found. With a surface energy of 0.42 eV per  $1 \times 1$  cell, the excess energy for a step was 0.25 eV per atom while that for a termination of a step at the boundary was -0.03 eV ( $\sim 0$  eV). Technical parameters for the larger calculations were  $1 \times 1 \times 14$  k-points, an RKMAX of 7.5 and RMTs of 2.5, using the PBEsol functional.

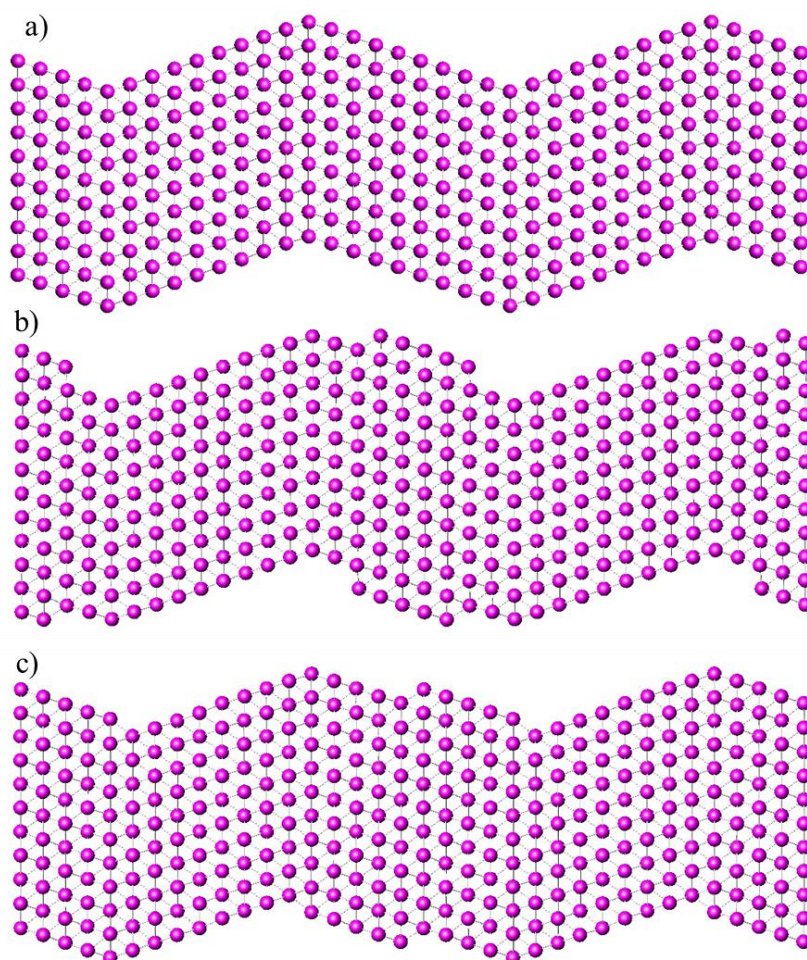


Figure 4.11 Three surface slabs used to calculate the energy associated with terminating an extra layer at a twin boundary.

Then the size-independent corner truncation will be discussed. Because the decahedra produced in this polyol synthesis had kinetic shapes, the kinetic Wulff construction could be used to describe the shape. These shapes could be understood in terms of a kinetic Wulff construction for twinned particles with slower growth of  $111$  facets [141] and enhanced growth at the re-entrant surfaces. The particles had flat surfaces, which was an indication of interface controlled growth. For a large facet, the growth velocity is controlled by the time taken to nucleate a single atomic

height terrace, which depends upon the chemical potential of both the external solution and the flat facet, plus the time for this terrace to grow over the whole facet.

The kinetic Wulff construction has two different solutions. One solution shows that the external surfaces are moving away from a common Wulff point, when all the facets are a part of the inner envelope. The second solution has the Wulff point lying outside the crystal and the facets are outside the inner envelope. However, at a truncated corner, the facet size is comparable to that of a critical single atomic height nucleus. If the chemical potential of the facet (via the wmc) is larger than that of the surrounding solution, the single-layer nucleus will never be stable. This third case leads to a Lyapunov steady-state solution where  $\mu_{ext} = \mu_i = \Omega_0 \bar{\gamma}_i / (L_i - h_i)$ . If  $(L_i - h_i)$  increases due to fluctuations of growth rate, the growth velocity  $\partial h_i / dt$  will increase as there is a larger driving force to add atoms to the facet. Similarly, if  $(L_i - h_i)$  decreases, the growth velocity will decrease and atoms would tend to be etched back into the solution from the facet. Therefore, the steady-state solution  $(L_i - h_i)$  is independent of particle size.

However, the kinetic Wulff construction assumes that growth occurs via nucleation of a small atomic height island followed by step-flow growth across the facet. If the surface is rough with existing steps, there is almost no nucleation barrier. Therefore, the simple truncation model has to be extended to rounded corners to account for this. In addition, a flat facet also has corners, and the same arguments can be applied to these corners, being truncated infinite times.

A simple approximation is to consider the truncation at the corner as a sphere, and the edge as a cylinder. In this case, the steady-state solution changes to  $\mu_{ext} = \mu_i = C \Omega_0 \gamma_R / R$  where  $R$  will be the radius of the corner,  $C$  depends upon the angles for the corner, and  $\gamma_R$  is the weight mean surface free energy of the rounded corner. For a simple rounded corner, the geometry can be

estimated as a circular cone, as shown in Figure 4.12. The apex angle of the cone is defined as  $2\theta$  according to geometry, so  $C$  may be written as,

$$C = \frac{6(1 - \cos\theta)}{\cos\theta \sin^2\theta + \sin^3\theta \tan\theta - 2(1 - \cos\theta)} \quad (4.8)$$

The weighted mean curvature can be understood as the rate of change of energy with respect to the change in volume. It is expected that the rate would be dependent on the solid angle of the corner. This was consistent with the experimental results. It should be mentioned that the radius  $R$  is also proportional to the homogeneous critical nucleation radius that would be used within a spherical model. This is not the critical nucleus size for the initial nucleation; it is rather the critical nucleus size for the current growth conditions. Therefore, the corner radius is also an indicator of the chemical potential of the growth solution.

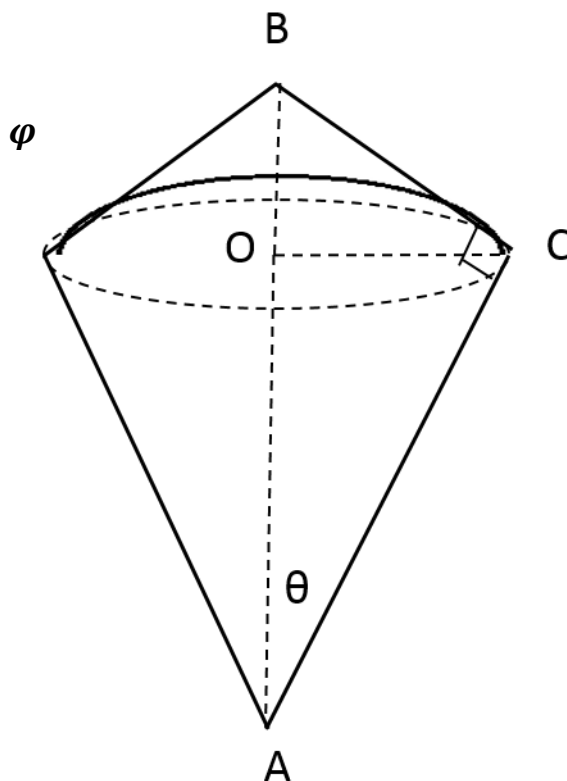


Figure 4.12 The geometry of the rounded corners when they are estimated as circular cones.

As a final point of this analysis, since the solution given above is the Lyapunov steady-state solution, the shape in actual growth will oscillate about this solution and only asymptotically converge to it. The scatter in the experimental data was real, and it showed the magnitude of the deviations from the solution during growth.

#### 4.3.3 Model for Pt Enhancement at the Corners

The EDX maps showed that the Pt concentration was higher at the corners than that on the surface. The corner rounding concept discussed in Section 3.3.2 is applied to explain this phenomenon. The local thermos-equilibrium is reached when the external chemical potential equals the chemical potential at the truncated corner.

The Lyapunov stable solution can be extended to the alloy systems. This is analogous to the Stefan problem. At the corner, the differential equation as a function of chemical potential can be written as,

$$\frac{ds}{dt} = -a(\mu(x_{Pt}) - x_{Pt}\mu^{ext}(Pt) - (1 - x_{Pt})\mu^{ext}(Pd)) \quad (4.9)$$

where  $s$  is the boundary of the corner,  $a$  is a constant,  $\mu^{ext}$  is the external chemical potential, and  $\mu(x_{Pt})$  is the chemical potential of the corner as a function of the Pt corner concentration, which can be written as,

$$\mu(x_{Pt}) = \frac{\Omega_o(x_{Pt}\bar{\gamma}_{Pt} + (1 - x_{Pt})\bar{\gamma}_{Pd})}{L - h} \quad (4.10)$$

where  $L$  is the distance from the Wulff center to the apex of a corner,  $h$  is the distance from the Wulff center to the truncated surface at a corner,  $\Omega_o$  is the atomic volume, and  $\bar{\gamma}_{Pt}$  and  $\bar{\gamma}_{Pd}$  are the weighted mean surface energy of Pt and Pd, assuming the surface energy of Pt/Pd alloy varies linearly between Pt and Pd. The Lyapunov solution is,

$$x_{Pt} = 1 - \frac{C\mu^{ext}(Pd) - \bar{\gamma}_{Pt}}{C[\mu^{ext}(Pt) - \mu^{ext}(Pd)] + \bar{\gamma}_{Pd}} \quad (4.11)$$

where,

$$C = \frac{L - h}{\Omega_o} \quad (4.12)$$

The Pt concentration at the corner is plotted as functions of Pt and Pd external chemical potentials in Figure 4.13.

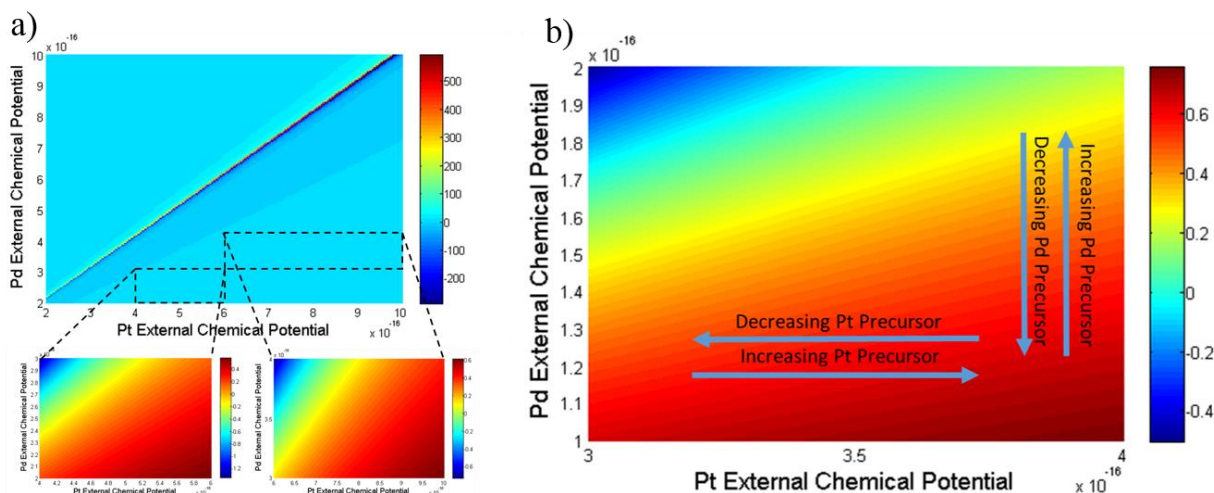


Figure 4.13(a) The corner concentration of Pt as functions of Pd and Pt external chemical potential. (b) A zoomed in Pt corner concentration map showing how Pt corner concentration changes with Pt and Pd precursor concentrations

The external chemical potential depends on the Pd and Pt monomer concentration in solution, and the chemical potential of one species can be written as,

$$\mu_i = \mu_0 + RT \ln a_i = \mu_0 + RT \ln \gamma \frac{b_i}{b_o} \quad (4.13)$$

where  $\mu_0$  is the standard chemical potential of a species,  $a_i$  is the activity of the species,  $\gamma$  is the activity coefficient,  $b_i$  is the molality, and  $b_o$  is the standard molality.

In Figure 4.13 (b), it shows that with increasing Pd precursor and decreasing Pt precursor concentrations in solution, the concentration of Pt at the corners decreases. In contrast, as the Pd precursor concentration decreases or as the Pt precursor concentration increases in solution, the Pt corner concentration increases. This is consistent with the experimental results.

#### 4.4 Discussion

The coexistence of a smooth composition gradient within the particle and the Pt corner enrichment indicates mixed control from the reaction kinetics that form the two different

monomers and the reaction kinetics of growth with local thermodynamic control at the corners, for the synthetic conditions herein. This is a natural extension of the corner rounding model to alloy systems. This could be of general relevance in many solution-based alloy nanoparticle growths, and we leave this hypothesis to future work.

From the analysis above, the deposition rate constant  $r_{Pd}(T)/r_{Pt}(T)$  ratio ranges from 9 to 18, with different amount of precursors added, and the reduction rate constant ratio  $k_{Pd}/k_{Pt}$  is around 1. In this particular synthesis, Pt has a much slower deposition rate compared to that of Pd. It implies that the presence of PVP slows down the Pt deposition rate. This is consistent with a Fourier transform infrared (FTIR) spectroscopy study which shows that there is a larger peak shift of C=O in FTIR spectra for PVP-Pt compared to PVP-Pd. The stronger interaction between Pt and PVP slows down the deposition of Pt, and therefore Pd preferentially get deposited onto the surface of the nanoparticles.

The degree of corner enrichment also depends on the amount of PVP used during synthesis. The degree of corner enrichment can be written as,

$$\text{degree of corner enrichment} = \frac{\text{corner concentration} - \text{central bulk concentration}}{\text{central bulk concentration}}$$

By changing the amount of PVP added during reaction, a significant change in degree of corner enrichment is observed. The degrees of corner enrichment for 50, 100 and 200% PVP are 35, 100 and 150%, (8, 18 and 50% of Pt at the corner) respectively. The corner concentrations are representations of the external chemical potentials.

There are mechanistic studies on how bimetallic nanoparticles form present in literature. Ahrenstorf *et al.* has studied the mechanism of Ni/Pt bimetallic nanoparticle formation and

demonstrated that Pt and Ni precursors had different consumption rates. [132] Choi *et al.* has systematically studied the formation mechanism of Pt/Ni octahedral and demonstrated the size and composition can be controlled by varying the amount of solvent, precursors, and surfactant added. [142] Mi *et al.* claimed that Pt/Ru alloy particle formation was the result of inter-diffusion between a core-shell-like structure, which was formed from two-step nucleation. [143] I have discussed the possibility of inter-diffusion in Section 4.3.1, and it was determined not to be the case in this system from post-annealing experiments. Yin *et al.* has seen Pd/Ag nanoparticles with highly twinned structures formed by coalescence and agglomeration. [144] The model discussed in this chapter demonstrated the coexistence of kinetic and thermodynamic controls, with detailed quantitative analysis. This model helps understand the inhomogeneous elemental distribution in bimetallic nanoparticles and would be beneficial for rational design of novel catalysts.

#### **4.5 Conclusion**

The smooth composition gradient within the particle is a result of reaction kinetics of monomer formation and growth of nanoparticles. The deposition rate constant ratio  $r_{\text{Pd}}(\text{T})/r_{\text{Pt}}(\text{T})$  is a function of the total amount of precursors, and it is independent of the ratio between Pt and Pd precursors added. The corner Pt enrichment is a result of local thermodynamic control at the corners. The mixture of thermodynamic and kinetic control in bimetallic nanoparticle synthesis could result in particles with complex composition distribution within the particles. This model offers opportunities to design novel bimetallic catalysts utilizing local elemental enrichments at the corners, where these are more active sites for a variety of catalytic reactions.

## CHAPTER 5

### **Thermodynamic Stability of Asymmetric Decahedral Nanoparticles**

## 5.1 Introduction

The size, shape and internal structure of nanoparticles are of interest in the past few decades. The physical and chemical properties of nanoparticles are largely dependent upon their morphologies, and they are widely used in many plasmonic and catalytic applications. [3, 5, 31, 145, 146] In the past decade, a tremendous amount of efforts have been made to synthesize nanoparticle with desired size, shape and internal structures. [30, 147] The understanding of the thermodynamics and kinetics of growth became crucial for improving nanoparticle synthesis.

In nanoparticle synthesis, other than single-crystalline particles, multiply twinned particles (MTPs) are commonly observed morphologies. There are three major types of MTPs, which are lamellar twinned particles (LTP), decahedral (Dh) particles and icosahedral (Ic) particles, respectively. LTPs are particles with a number of parallel (111) twin boundaries. Dh and Ic MTPs contain multiple twin boundaries and disclinations. Dh MTPs contain 5 single-crystalline segments, each separated by two (111) twin boundaries. Ic MTPs consist of 20 single-crystalline segments, each separated by three (111) twin boundaries.

The equilibrium shapes of the MTPs could be expressed by the modified Wulff construction, which finds the minimum energy shape for each single crystal subunits, with the twin boundaries taken into account. The final composite particle is the assembly from these single crystal subunits. [148] In this chapter, the thermodynamic stability of Pt/Pd bimetallic Dh nanoparticles is analyzed. In modified Wulff construction, only symmetric MTPs were considered as the five single crystal segments were identical. As mentioned in Chapter 2, depending on the surface energy ratio  $\gamma_{111}/\gamma_{100}$ , the thermodynamically stable Dh could have different shapes. The commonly observed thermodynamic shapes are the ones with (111) re-entrant facets, as known as

Marks Dh. When  $\gamma_{111}/\gamma_{100} > 2/\sqrt{3}$ , the re-entrant notches will disappear, and the particles will form a rod-like shape, similar to the ones that first investigated by Ino. [14, 17, 18] This is a constrained thermodynamic structure, not a global minimum. If  $\gamma_{111}/\gamma_{100} \ll 1$ , the (100) facets no longer appear in final shapes, and the Dh has a star like shape. This is a plausible global thermodynamic structure. The possibilities are more limited for Ic particles.

However, the Dh particles that don't have 5-fold symmetry had been previously observed by Prof. L. D. Marks. Figure 5.1 shows two examples of particles which lack 5-fold symmetry.

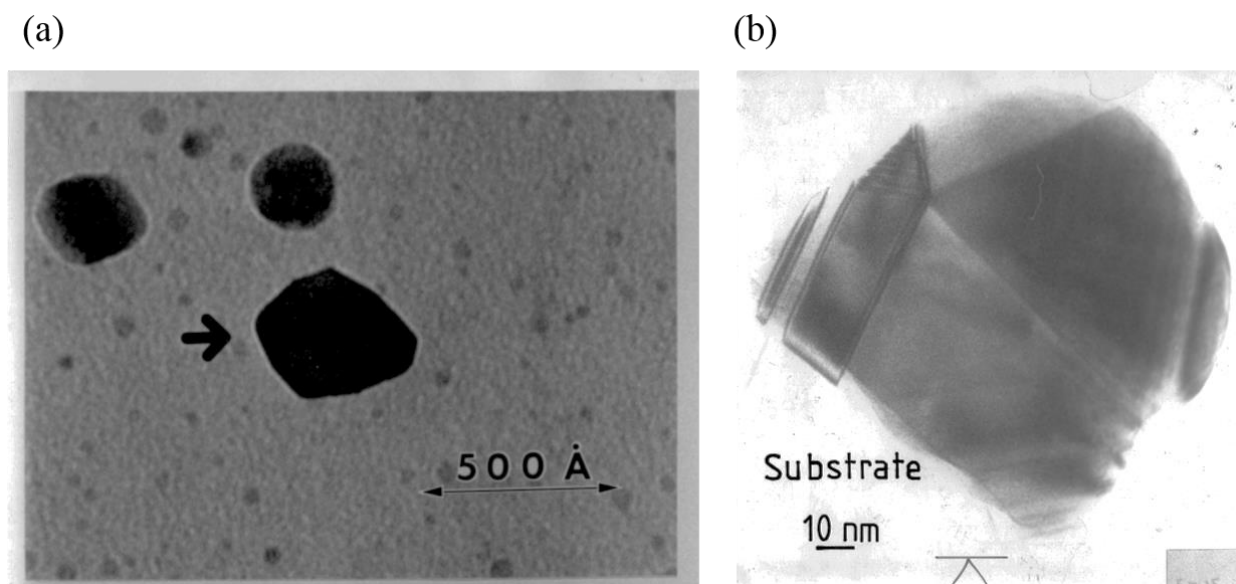


Figure 5.1 TEM images of asymmetric Dh particles that have been previously observed. (a) Asymmetric Dh particle with two small segments, and (b) asymmetric Dh particle with one small segment.

As shown in Figure 5.1, one or two segments of the Dh were significantly smaller than the rest of the segments, which corresponded to two different cases. The disclination migrates towards one side of the particle and this corresponds to the structural change from Dh to single crystal. The motion of the disclination to the other side gives a change from Dh to a particle with one twin

boundary. The migration of the disclination is illustrated in Figure 5.2. [19] Figure 5.1 (a) corresponds to the first case and Figure 5.1 (b) corresponds to the second.

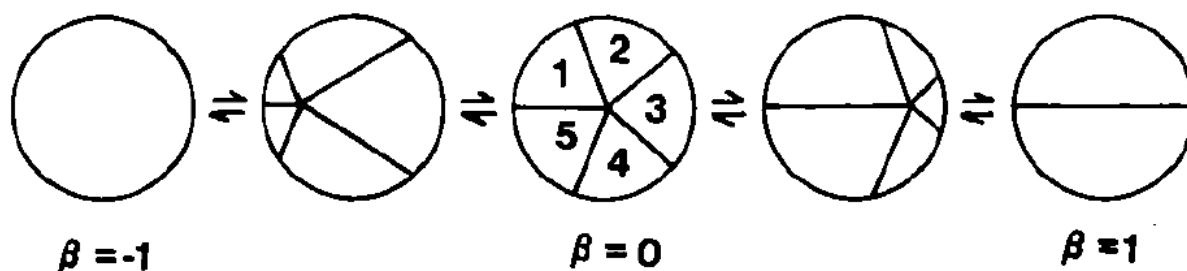


Figure 5.2 Schematics showing the two cases when the disclination migrates out of the Dh MTP

In this chapter, Dh's with mirror symmetry were observed. The thermodynamic stability of the asymmetric Dh nanoparticles was discussed, and the future direction was proposed.

## 5.2 Methods

### 5.2.1 Synthesis of Pt/Pd Bimetallic Nanoparticles

Similar to the Pt/Pd nanoparticle synthesis described in Chapter 4, the synthesis of Pt/Pd alloy multiply twinned particles was performed via a method developed by Lim *et al.* [114] PVP (MW = 55000, from Sigma-Aldrich) was dissolved in 16 mL of deionized water and the solution was heated to 80 °C in air. 0.032 mmol of Na<sub>2</sub>PdCl<sub>4</sub> and 0.032 mmol K<sub>2</sub>PtCl<sub>4</sub> were dissolved in 6mL of deionized water at room temperature. The Na<sub>2</sub>PdCl<sub>4</sub> and K<sub>2</sub>PtCl<sub>4</sub> precursor solution was added to the PVP aqueous solution and the mixture was heated at 80 °C under stirring for 18 h in air. The Pt/Pd nanocrystals were washed five times with deionized water before TEM imaging. The syntheses were carried out by Lu Jiang.

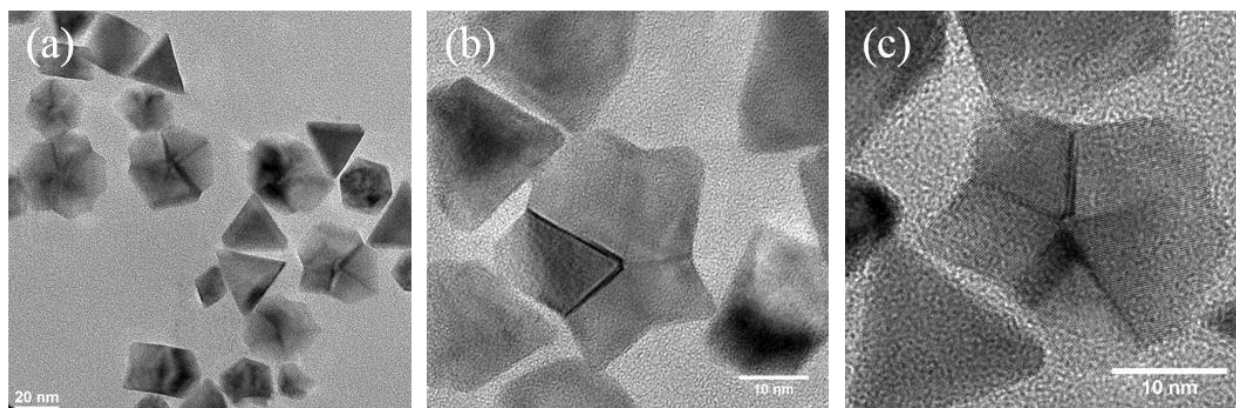


Figure 5.3 (a) As-synthesized particles synthesized with 50% PVP, (b) An asymmetric Dh particle synthesized with 110% PVP, and (c) An asymmetric Dh particle synthesized with 100% PVP

### 5.2.2 Synthesis of Pd Dh Nanoparticle

Pd nanoparticles were synthesized by the method developed by Lim *et al.* [149] PVP (MW=55000, from Sigma-Aldrich) and citric acid were dissolved in 8mL of deionized water and the solution was heated at 90 °C in air under stirring. 3 mL of 17.4 mM Na<sub>2</sub>PdCl<sub>4</sub> (from Sigma-Aldrich) aqueous solution was added to the PVP/citric acid solution. In this synthesis, 100% PVP concentration corresponds to the molar ratio of Na<sub>2</sub>PdCl<sub>4</sub> to the repeating unit of PVP at 1:5. 100% concentration of citric acid is 0.39 M. Different PVP concentration (75, 83, 91.5 and 100%) and citric acid (100 and 150%) were used in this synthesis to yield Marks decahedra with mirror symmetry. The solution was heated at 90 °C under stirring for 26 h in air. The product was washed once with acetone, once with ethanol, and three times with deionized water before imaging. The syntheses were carried out by Dana Lapides.

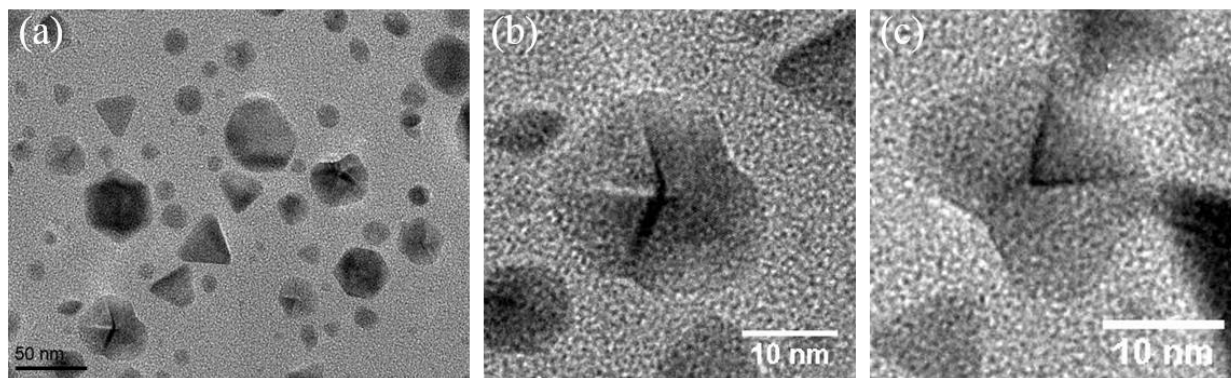


Figure 5.4 As-synthesized particles synthesized with 75% PVP

### 5.2.3 Finite Element Analysis

The finite element analysis (FEA) calculations were performed by Professor Srikanth Patala from North Carolina State University. FEA is a numerical method for solving partial differential equations with appropriate boundary conditions. The large problems were divided into smaller and simpler problems, which are called finite elements. This method has been widely used in the field of elasticity, heat transfer, and fluid dynamics.[150] The strain energy density in asymmetric Dh was calculated in ABAQUS. In comparison with the analytical methods, the FEA was able to calculate the strain energy density for specific geometries that were similar to the ones observed in experiments.

### 5.3 Determination of Re-entrant levels

The synthesized Dhs had a mirror symmetry, instead of a 5-fold symmetry. The re-entrant level was defined as  $(2a + 2b + c)/Full\ Twin\ Length$ , and  $a$ ,  $b$ , and  $c$  are the length of re-entrances. Full twin length was defined as the length of the twins without truncation. To simplify this problem, the five re-entrant values were reduced to three, owing to the mirror symmetry. The mirror plane was shown as the dash line in Figure 5.5. The single crystal segments were labelled as  $A$ ,  $B$  and  $C$ .

The re-entrant lengths were defined as  $a$ ,  $b$  and  $c$ . A TEM image of a typical asymmetric Dh was shown in Figure 5.5 (i). The total re-entrant level vs. full twin length and the distribution of the re-entrant levels were plotted in Figure 5.6. As shown in Figure 5.6, the total re-entrant level centers around 1.7.

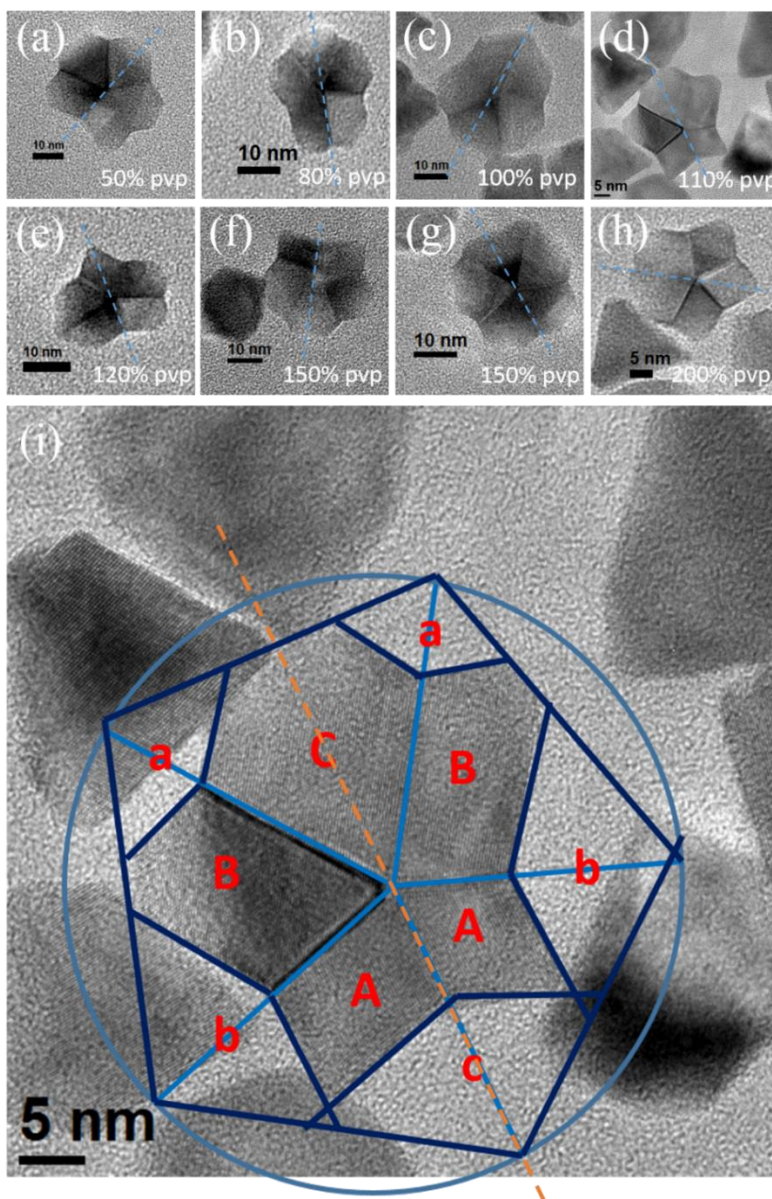


Figure 5.5 TEM image of (a) – (h) asymmetric Dh particles synthesized using different amount of PVP, and the mirror symmetry is present in all syntheses conditions, and (i) a typical asymmetric Dh with geometric parameters  $a$ ,  $b$  and  $c$  being labeled.

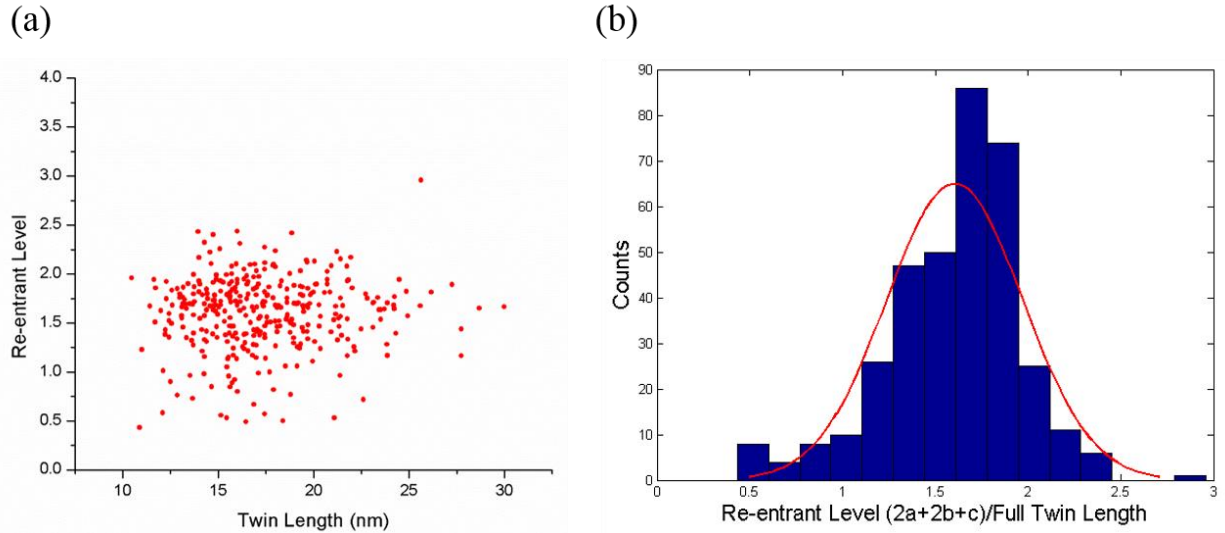


Figure 5.6 (a) The re-entrant level of asymmetric Dh as a function of twin length, and (b) the histogram of the re-entrant level of 359 asymmetric Dh particles.

#### 5.4 Bulk-surface Energy Balance

In Dh particles, the single-crystalline segments are not completely space filling, so the bulk strain energy has a similar order of magnitude as the surface energy. The strain energy can be written as,

$$W_D = [\varepsilon_D^2 \mu V / 4(1 - \nu)](1 - \beta^2)^2 \quad (5.1)$$

where  $\varepsilon_D$  is the plane strain in Dh, with  $\varepsilon_D = 0.0205$ ,  $\nu$  is the Poisson's ratio,  $\mu$  is the shear modulus, and  $\beta$  is the fractional distance of the disclination from the center.

The surface stress energy can be considered as a correction term to the surface energy term, and it can be written as,

$$W^S = \frac{1}{2} \varepsilon_D g \gamma_{111} e_w V^{\frac{2}{3}} (1 - \beta^2) \quad (5.2)$$

where  $e_w$  is a dimensionless energy parameter and it can be expressed as,

$$e_w = (\gamma_{111})^{-1} \left( \int \gamma dS \right) \left\{ \int dV \right\}^{-2/3} \quad (5.3)$$

Therefore, the total surface energy  $E_S$  is  $E_S = e_w \gamma_{111} V^{2/3}$ .  $e_w$  is also a function of surface anisotropy ratio  $\alpha$ , which is the ratio between (100) surface energy and the surface energy of (111) facets.

The total surface energy with surface stress contribution will be the sum of the strain-free surface energy and the surface stress energy, which can be expressed as,

$$E_S = \gamma_{111} e_w V^{2/3} \left( 1 + \frac{1}{2} \varepsilon_D g (1 - \beta^2) \right) \quad (5.4)$$

The surface stress contribution can be approximated as a fraction of the strain free surface energy. Therefore, the next step will be to determine the total surface energy and total volume as a function of geometry. Seeing from Figure 5.9, the surface area and volume can be written as functions of  $L$ ,  $h$ ,  $a$ ,  $b$  and  $c$ , where  $L$  is the side length of a perfect Ino Dh,  $h$  the length of the disclination along [100] direction,  $a$ ,  $b$ , and  $c$  the re-entrances, respectively.

## 5.5 Finite Element Methods

The analytical representation suggests that the symmetric case wouldn't be stable at larger sizes because the elastic strain energy dominates as the size of the Dh increases. The strain energy per-volume  $W_D$  calculated by FEA varied with the geometry and the strain energy density as a function of  $a$ , when fixing  $c$  at 0.34 and total re-entrant level at 1.7. The stress concentrations in asymmetric Dh's with different  $a$  values are shown in Figure 5.7. The strain energy density as a function of  $a$  is plotted in Figure 5.8(a), and the corresponding dimensionless parameter  $e_w$  is

plotted in Figure 5.8(b). The FEA calculations were performed with Ag. Assuming that the strain were elastic, and the corresponding strain energy density of Pd were calculated.

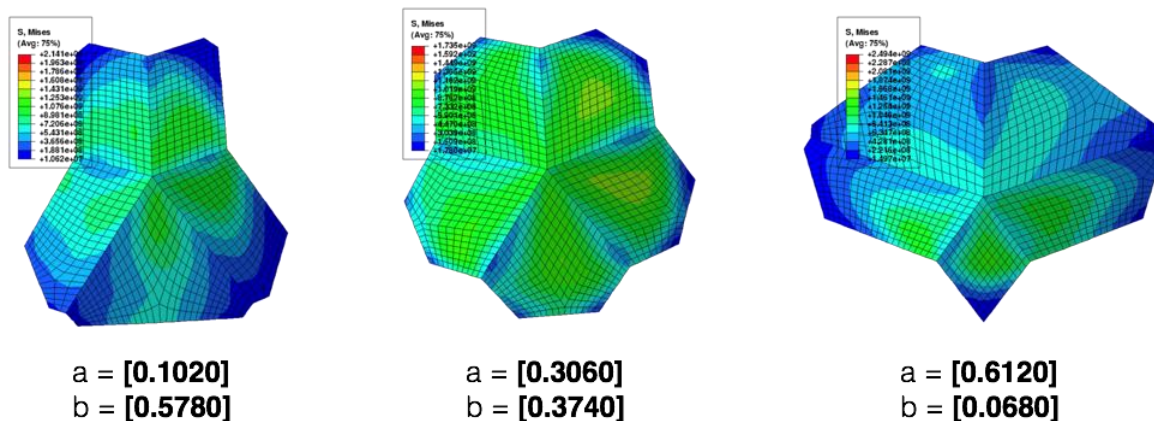


Figure 5.7 Von Mises stress concentration in asymmetric Dh particles with geometric parameters: (a)  $L = 1$ ,  $h = 1$ ,  $a = 0.102$ ,  $b = 0.578$ ,  $c = 0.34$ , (b)  $L = 1$ ,  $h = 1$ ,  $a = 0.306$ ,  $b = 0.374$ ,  $c = 0.34$ , and (c)  $L = 1$ ,  $h = 1$ ,  $a = 0.612$ ,  $b = 0.068$ ,  $c = 0.34$ .

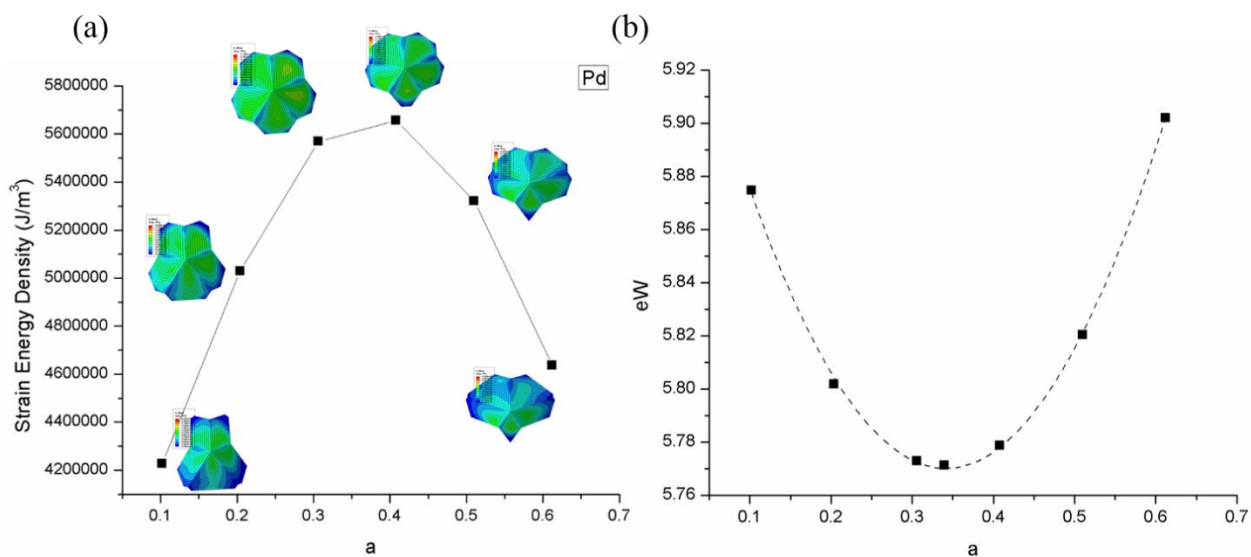


Figure 5.8 (a) Strain energy density of Dh with different geometric parameters,  $a = [0.102, 0.204, 0.306, 0.408, 0.51, 0.612]$ ,  $b = [0.578, 0.476, 0.374, 0.272, 0.17, 0.068]$ , and  $c = 0.34$  (b) The dimensionless surface energy parameter at the corresponding geometric parameters.

## 5.6 Results

In order to calculate the total energy of the asymmetric nanoparticles, the total volume and surface area of the Dh needs to be determined. The Dh can be divided into five segments. Owing to the mirror symmetry, there are only 3 distinct segments, A, B and C, as shown in Figure 5.5. A single segment is demonstrated in Figure 5.9 (a), and the projection of an asymmetric Dh along  $[110]$  direction is shown drawn in Figure 5.9 (b).

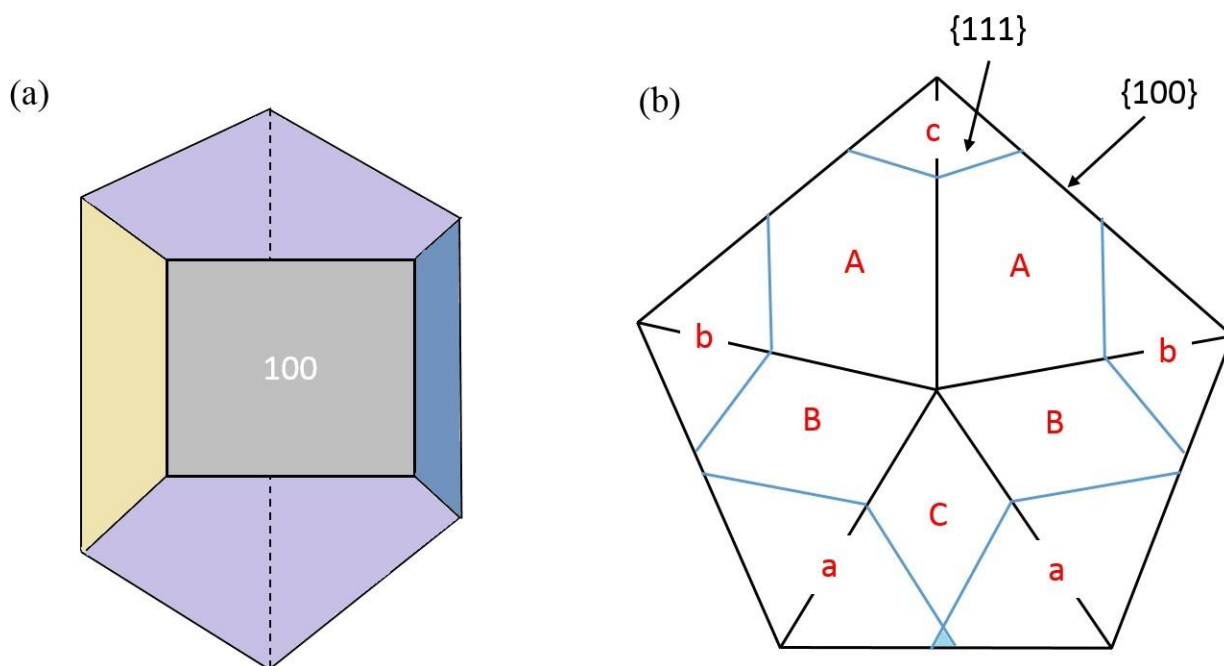


Figure 5.9 (a) Illustration of one segment in the asymmetric Dh. The gray facet corresponds to  $111$  facets, and the rest of the facets are  $111$ . (b) Schematic of an asymmetric Dh with geometric parameters  $a$ ,  $b$  and  $c$ .

The volume of a segment could be written as the volume of a complete tetrahedron subtracted by the volume of the re-entrants. For instance, the volume of segment  $B$  in Figure 5.9 (b) can be written as,

$$\begin{aligned}
V_B &= V_T - V_a - V_b \\
&= \frac{L^3}{6\sqrt{2}} + \frac{L^2}{2\sqrt{2}} \cdot (h - L) - \left[ \frac{a^3}{6\sqrt{2}} + \frac{a^2}{2\sqrt{2}} \cdot (h - L) \right] - \left[ \left[ \frac{b^3}{6\sqrt{2}} + \frac{b^2}{2\sqrt{2}} \cdot (h - L) \right] \right]
\end{aligned} \tag{5.5}$$

where  $V_T$  is the volume of a complete tetrahedron;  $V_a$  is the volume of the re-entrance with length  $a$ , and  $V_b$  is the volume of the re-entrance with length  $b$ . The volume of the asymmetric Dh is the sum of the five segments. It worth mentioning that, the volume of re-entrance could be double counted when the sum of the length of the two re-entrance is greater than the side length of the perfect Dh, highlighted in blue in Figure 5.9 (b). In this case, the volume of segment A can be written as,

$$\begin{aligned}
V_C &= V_T - 2V_a + V_S \\
&= \frac{L^3}{6\sqrt{2}} + \frac{L^2}{2\sqrt{2}} \cdot (h - L) - \left[ \frac{a^3}{3\sqrt{2}} + \frac{a^2}{\sqrt{2}} \cdot (h - L) \right] + \left[ \frac{(2a - L)^3}{6\sqrt{2}} + \frac{(2a - L)^2}{2\sqrt{2}} \cdot (h - L) \right]
\end{aligned} \tag{5.6}$$

where  $V_S$  is the volume of the shaded region in Figure 5.9 (b).

The surface area of the Dh is the sum of the surface area of the five segments. For instance, the surface area of segment B will be the sum of the surface area of 100 and 111. The surface area of segment B in Figure 5.9 (b) can be written as,

$$\begin{aligned}
S &= S_{100} + S_{111} = (L - a - b) \cdot (h - L) + \frac{\sqrt{3}}{2} (L^2 - a^2 - b^2) \\
&\quad + \frac{\sqrt{3}}{4} [(h - L + a)^2 + (h - L + b)^2 - 2(h - L)^2]
\end{aligned} \tag{5.7}$$

where  $S_{100}$  and  $S_{111}$  are the surface area of 100 and 111 facets, respectively. The 100 facets will vanish when the sum of two re-entrance is greater than  $L$ . The MATLAB code is provided in *Appendix A*.

The total energy as a function of  $a$ ,  $b$ ,  $c$ ,  $L$  and  $h$  can be written as,

$$E = W_V^D V + \gamma_{111} e_W S \quad (5.8)$$

where  $W_V^D$  is the strain energy density, calculated by FEA. The energy as a function of  $a$  for Dh with volume of  $10^{-25}$ ,  $5 \times 10^{-24}$ ,  $10^{-23}$ , and  $1.5 \times 10^{-23} \text{ m}^3$  are plotted in Figure 5.10. One thing needs to be mentioned was that the surface energy  $\gamma_{111}$  was the sum of strain-free surface energy and the surface stress. The surface stress was assumed to be proportional to the strain-free surface energy.

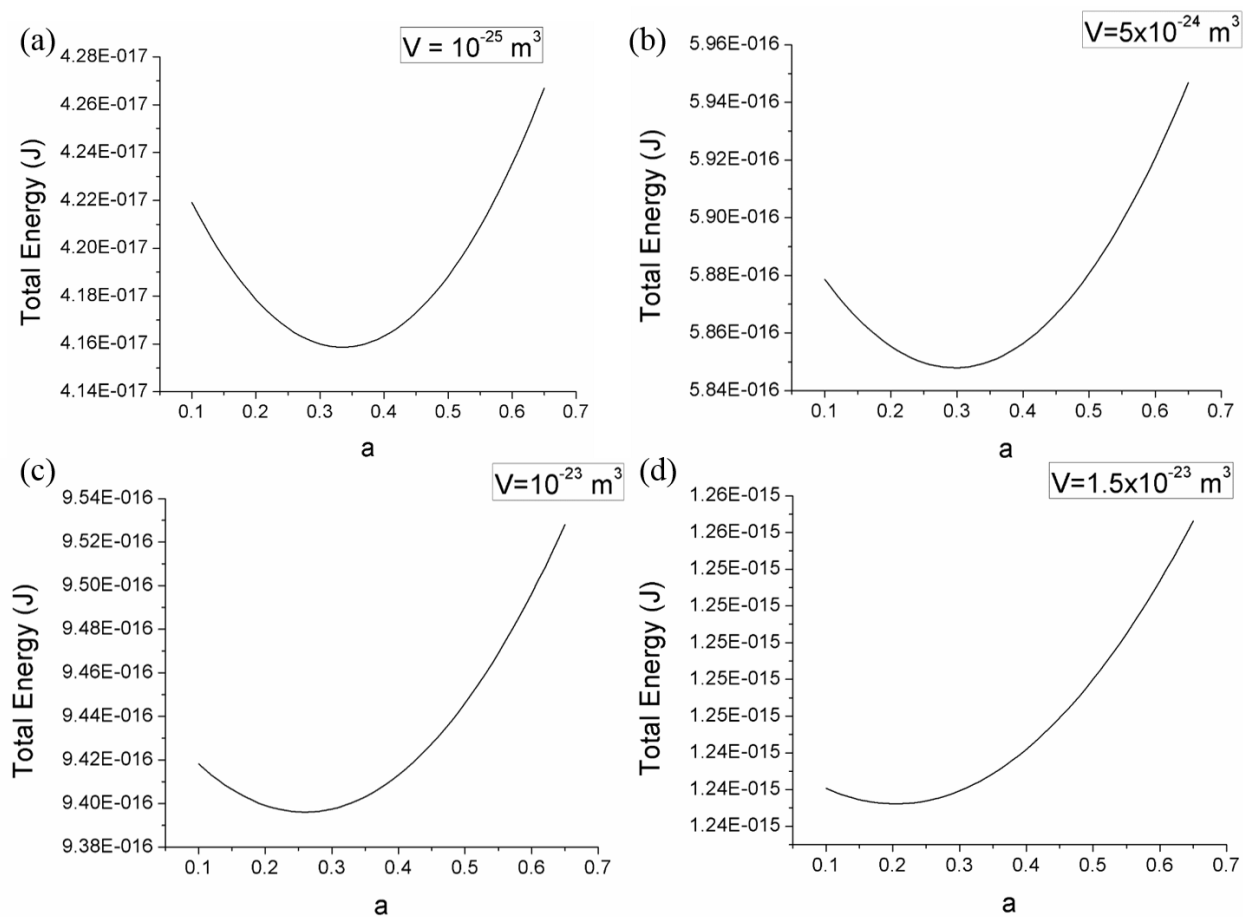


Figure 5.10 Free energy of asymmetric Dh as a function of  $a$ , with  $c$  and re-reentrant level fixed at 0.34 and 1.7, respectively, at different sizes.

Seeing from Figure 5.10, the free energy minimum shifted as the size of the particle increased. The dimensionless surface energy parameter  $e_w$  has a minimum when the Dh has a five-fold symmetry. Therefore, at small sizes, particles with 5 identical segments had the thermodynamically stable configuration. However, as the size of the Dh increased, the local minimum shifted towards a smaller  $a$  value, as shown in Figure 5.10. The Dh with 5-fold symmetry was no longer the thermodynamically stable structure.

The  $a$  value corresponding to the free energy curve was a function of size. In order to plot  $a$  vs. radius of the Dh, the strain energy and  $e_w$  as a function of  $a$  were fit with a 2<sup>nd</sup> order polynomial. The  $a$  values corresponding to free energy minima as a function of Dh radius is plotted in Figure 5.11. The radius of the Dh was calculated by approximated the Dh as a cylinder.

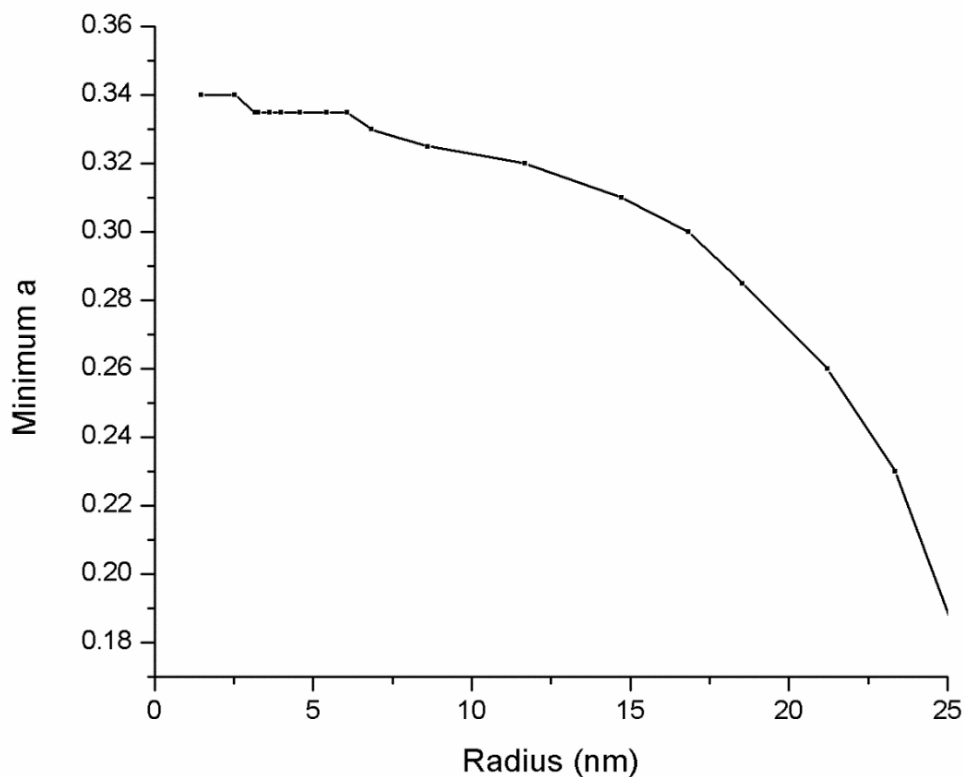


Figure 5.11 Calculated  $a$  values at free energy minima as a function of Dh particle size

Figure 5.11 shows that the asymmetric Dh nanoparticle may not be the thermodynamically stable structure when the size of the Dh particles grown bigger. Figure 5.11 is one trajectory when the total re-entrant level is fixed at 1.7.

## 5.7 Conclusion

Asymmetric Dh particles with a mirror symmetry had been synthesized under different conditions. The products had shapes which could be fit with a full Dh with some level of re-entrance at each corner. The total re-entrant level of 359 Dh particles synthesized using different amount of PVP was measured and the total re-entrant centered around 1.7. This phenomenon had been observed in syntheses of both Pd/Pt and Pd Dh particles.

FEA calculations have been performed on particles with different  $a/b$  ratio, with  $c$  and total re-entrant level being fixed at 0.34 and 1.7, respectively. The free energy of the particles (strain energy + surface energy) was calculated and plotted as a function of  $a$ . As the size of the Dh increased, the local minimum shifted towards a smaller  $a$  value. It indicates that the 5-fold symmetric Dh is the thermodynamically stable configuration at very small sizes, and as the size of the particle increases, the asymmetric particle with a mirror symmetry starts to be the thermodynamically stable structure.

## 5.8 Future Work

The free energy of the Dhs with different  $a/b$  ratios with  $c$  and total re-entrant level being fixed at 0.34 and 1.7 respectively was calculated. The free energy minimum was found to be shifted towards smaller  $a$  values. However, only 6 points on one trajectory were calculated, which were not enough to cover the whole free energy landscape. Other local minima could be found at some

other geometric parameters. More FEA calculations will be performed to cover the whole free energy landscape. The calculation will be performed at  $a = [0.1:0.1:0.9]$ ,  $b = [0.1:0.1:0.9]$ ,  $c = [0.1:0.1:0.9]$ , respectively. Then a set of calculations with finer mesh size will be performed to determine the fine details of the free energy minimum.

In addition, the surface stress term was assumed to be proportional to surface energy, but independent of geometry. However, one would expect that the surface stress would be a function of geometry as well. The surface stress could be obtained from the FEA calculations, and the contribution from surface stress should be considered.

Furthermore, the as-synthesized particles could be annealed at high temperature over a few hours. If there is no significant shape change, it would further confirm that the synthesized particles have thermodynamic shapes.

## CHAPTER 6

### **Strain-induced Segregation in Bimetallic Multiply Twinned Particles**

## 6.1 Introduction

Bimetallic nanoparticles have received substantial attention in recent years. They offer unique optical, electronic, and catalytic properties that depend on the size, shape, and composition of the particles, as well as elemental distribution within them and at their surfaces.[39, 151-155] For instance, the localized surface plasmon resonance (LSPR) of noble metal alloy nanoparticles can be tuned by their composition as well as their morphology, as shown in both theoretical and experimental works.[35, 156] A second property of interest is their catalytic behavior.[39, 42, 157-159] Alloy nanoparticles have been widely used as heterogeneous catalysts since last century. The bimetallic nanoparticles offer distinct activities and selectivity different and often better than those of their monometallic counterparts, because the local electronic environment of and local chemisorption and reaction properties of adsorbates are modified. [39, 43, 157, 159, 160] The structures of bimetallic nanoparticles are more complicated because of their one additional degree of freedom – composition. The particles can be phase separated into different structures, such as core-shell[86, 161] and Janus[91, 92] structures, or alloyed, where the two elements can be mixed randomly or with some degree of segregation.[93-95, 162]

Numerical simulations, such as density functional theory (DFT), Monte Carlo simulations using empirical/semi-empirical potentials including second-moment approximation tight binding (SMATB) potentials, and embedded atom potentials have been widely used to analyze the segregation of small alloy nanoparticles with a limited number of atoms and, most of the time, with fixed shapes.[163-171] The numerical methods can be very accurate in some cases for small particles by using the appropriate potentials and particle structure approximation. However, they

lack the ability to extract trends as a function of composition, size, temperature, and other possible parameters. In this case, analytical models are more powerful.

Ringe *et al.*[172] have developed an analytical model called alloy Wulff construction. In this model, one can predict the surface segregation and equilibrium shape of a free-standing single-crystalline bimetallic nanoparticle as a function of composition and size. In many cases, nanoparticles are not single crystals but instead multiply twinned particles (MTPs) containing twin boundaries. The most commonly observed MTP shapes are lamellar twinned particles (LTP), decahedral (Dh) particles and icosahedral (Ic) particles. LTPs are particles with a number of parallel (111) twin boundaries. Dh MTPs contain 5 single-crystalline segments, each separated by two (111) twin boundaries. Ic MTPs consist of 20 single-crystalline segments, each separated by three (111) twin boundaries.

In this chapter, the elastic strain induced segregation inside bimetallic MTPs is discussed, and an analytical solution of the composition distribution at thermal equilibrium is derived.

## **6.2 Derivation of Strain-induced Segregation**

### **6.2.1 Inhomogeneous Strains in Decahedra and Icosahedra**

In multiply twinned particles, namely Dh and Ic, the single-crystalline segments are not completely space filling, so there are some internal distortions present.[65, 173] The internal strains have been considered in several ways in literature. Bagley[65] and Yang[66] suggested that there is a structure transformation from FCC to body-centered orthorhombic. However, that is no longer considered to be correct. The homogeneous strain was first analyzed by Ino.[14] De Wit first pointed out that the elastic strain could be formulated via classical Volterra disclinations.[67] The inhomogeneous strain for both Dh and Ic particles used in this model were

analyzed and approximated by Marks, Howie, and Yoffe.[68] More recently, Patala *et al.* have shown nonuniform elastic strain distributions in Dh and Ic particles via finite element analysis (FEA).[69] Zhou *et al.* have observed nonuniform strain in Dh nanowires using large-scale molecular dynamics simulations.[70] In this chapter, a detailed analytical analysis of strain driven segregation in MTPs is discussed.

### 6.2.2 Change in Energy

Segregation produces two additional change in energy terms. In order to obtain the most stable segregation state, the total change in energy in multiply twinned particles is minimized. The first term is the change in strain energy, which is analogous to a  $PdV$  term. By assuming the local strain field does not change, the change in strain energy is the additional energy term, which is the change in strain energy due to local expansion or contraction. It can be written as,

$$E^{strain} = -K \int \Delta \cdot (a(C_i)^3 - a_H^3)/a_H^3 dV \quad (6.1)$$

where  $K$  is the bulk modulus;  $\Delta$  is the cubic dilatation;  $C_i$  is the local concentration of element “i”;  $a(C_i)$  is the local lattice parameter;  $a_H$  is the lattice parameter for the homogeneous concentration.  $(a(C_i)^3 - a_H^3)/a_H^3$  is the local expansion or contraction when the expansion or contraction from segregation is assumed to be equivalent to the lattice expansion or contraction.

For decahedral particles, strains are estimated as plane strains since there are no components in z direction. The strains defined in cylindrical coordinates are,[139]

$$e_{rr} = \left[ \frac{1 - 2\nu}{2(1 - \nu)} \right] \varepsilon_D \left[ \ln \left( \frac{r}{R} \right) + 1 \right] - \varepsilon_D/2 \quad (6.2)$$

$$e_{\varphi\varphi} = \left[ \frac{1-2\nu}{2(1-\nu)} \right] \varepsilon_D \ln\left(\frac{r}{R}\right) + \varepsilon_D/2 \quad (6.3)$$

where  $\nu$  is the Poisson's ratio,  $r$  is the local radius,  $R$  is the radius of the Dh, and  $\varepsilon_D$  is the strain of the Dh, which is 0.0205.

Segregation also changes the configurational entropy in a binary system,

$$\Delta S_{mix} = S_{seg} - S_o \quad (6.4)$$

where  $S_{seg}$  is the configurational entropy after segregation, and  $S_o$  is the entropy of the solid solution before segregation when the composition is homogeneous.

In this model, the bimetallic system is assumed to be an ideal binary solid solution, hence the change in free energy from the entropy of mixing is:

$$E^{Entropy} = \int nkT \{x(r) \ln x(r) + (1-x(r)) \ln(1-x(r)) - [C_H \ln C_H + (1-C_H) \ln(1-C_H)]\} / a_H^3 dV \quad (6.5)$$

where  $n$  is the number of atoms in a unit cell, which is 4 for FCC metals;  $C_i$  is the local concentration of element "i", and  $C_H$  is the homogeneous bulk concentration of element "i".

The total change in energy  $E$  is the sum of  $E^{Strain}$  and  $E^{Entropy}$ . It is a function of position  $r$  and the local concentration  $x(r)$  and can be written as follows for the Dh case,

$$\begin{aligned} E &= E^{Strain} + E^{Entropy} \\ &= \int \left[ \left( 4kT \{x(r) \ln x(r) + (1-x(r)) \ln(1-x(r))\} - [C_H \ln C_H + (1-C_H) \ln(1-C_H)] \right) \right] / a_H^3 \\ &\quad - K\Delta \left\{ [(a_i - a_j)x(r) + a_j]^3 - a_H^3 \right\} / a_H^3 dV \end{aligned} \quad (6.6)$$

where  $a_i$  is the lattice parameter for element “i”;  $a_j$  is the lattice parameter for element “j”, and  $a_H$  is the lattice parameter at the homogeneous bulk concentration.

### 6.2.3 Derivation of Composition Distribution

In order to get the equilibrium composition profile within a MTP, the total change in energy is minimized subject to a mass conservation constraint. For Dh particles, the mass conservation constraint is,

$$C = \int_0^R x(r)2\pi r t dr = \pi R^2 t C_H \quad (6.7)$$

where  $x(r)$  is the local concentration of element “i” as a function of position  $r$ . Now, the energy  $E(r,x)$  must be minimized with respect to the functional  $x(r)$ , which is a constrained variational problem and is solved by a calculus of variation method. The Lagrangian function is:

$$L(r, x) = E(r, x) - \lambda C(r, x) \quad (6.8)$$

where  $E(r,x)$  is the change in energy, with  $x(r)$  as the target function, and  $C(r,x)$  is the constraint.

Because both  $E(r,x)$  and  $C(r,x)$  are independent of the derivative of  $x(r)$ , the Euler-Lagrange equation can be simplified as,

$$\frac{d}{dr} \left( \frac{\partial(E - \lambda C)}{\partial x'} \right) = \frac{\partial(E - \lambda C)}{\partial x} \rightarrow \frac{\partial E}{\partial x} - \lambda \frac{\partial C}{\partial x} = 0 \quad (6.9)$$

If the change in concentration is small, the change in strain energy can be Taylor expanded and written as,

$$E^{strain} = - \frac{K\Delta[a_j^3 + 3a_j x(a_i - a_j)]}{a_H^3} \quad (6.10)$$

where  $a_i$  is the lattice parameter for element “i” and  $a_j$  is the lattice parameter for element “j”. If eq. 6.10 is plugged into eq. 6.9, the Euler-Lagrange equation then has a Fermi-Dirac-like solution,

$$x(r) = \frac{1}{1 + \exp\left[\left(C_1\Delta(r) - \frac{a_H^3}{4}\lambda\right)/kT\right]} \quad (6.11)$$

where  $C_1 = -\frac{3K}{4}a_j^2(a_i - a_j)$  and is a constant. The Lagrangian multiplier  $\lambda$  can be solved numerically by plugging  $x(r)$  into eq. 6.7. In this chapter,  $C_I$  will be written as  $C$  and  $\lambda$  will be written as  $\mu$ , which is the chemical potential per unit volume of species “i”. This composition distribution  $x(r)$  of element “i” is analogous to the distribution of point defects around a dislocation line (Cottrell Atmosphere)[174] that is caused by the elastic strain field around the dislocation.

The chemical potential  $\mu$  of element “i” can be determined by solving,

$$\int_0^R 2\pi r t \frac{1}{1 + \exp\left[\left(C\Delta - \frac{a_H^3}{4}\mu\right)/kT\right]} = \pi R^2 t C_H \quad (6.12)$$

The definite integral is evaluated applying the Simpson’s 3/8 rule.

The composition profile of an Ic can be calculated using the same method. For Ic particles, the inhomogeneous strains have been solved by Yoffe, Howie and Marks and are defined in spherical coordinates as,[173]

$$e_{rr} = \frac{2}{3}\varepsilon_I \left(\frac{1-2\nu}{1-\nu}\right) \left[\ln\left(\frac{r}{R}\right) + 1\right] - \frac{2\varepsilon_I}{3} \quad (6.13)$$

$$e_{\theta\theta} = e_{\varphi\varphi} = \frac{2}{3}\varepsilon_I \left(\frac{1-2\nu}{1-\nu}\right) \ln\left(\frac{r}{R}\right) + \frac{\varepsilon_I}{3} \quad (6.14)$$

where  $\varepsilon_I = 0.0615$  is the strain in an icosahedral particle.[173]

For Ic particles, the mass conservation constraint is,

$$\int_0^R x(r)4\pi r^2 dr = \frac{4}{3}\pi R^3 C_H \quad (6.15)$$

Patala *et al* [175] have calculated the strain energy for Dh and Ic particles using finite element analysis (FEA) methods and compared them with the approximation used above.[173] The strain energy of a Dh particle is approximately 0.75 times that of the plane strain approximation, and the strain energy of an Ic particle is about 1.45 times that of the spherical inhomogeneous strain approximation.

The above analytical solution was derived based on the assumption of an ideal solution. If a regular solution system is considered, the change in energy is from both the entropy of mixing and the enthalpy of mixing. This produces an additional energy term, and the energy change  $E^{Entropy+Enthalpy}$  can be written as follows,

$$\begin{aligned} E^{Entropy+Enthalpy} &= \int \left( 4kT\{x(r)\ln x(r) + (1 - x(r))\ln(1 - x(r)) \right. \\ &\quad \left. - [C_H \ln C_H + (1 - C_H)\ln(1 - C_H)]\} + \Omega x(r)(1 - x(r)) \right) / a_H^3 dV \end{aligned} \quad (6.16)$$

where  $\Omega$  is a constant that can be either positive or negative depending on the system. When the variational method is used to solve this problem, the equation can be simplified to a form as follows,

$$kT \ln \frac{x}{1-x} + \Omega'(1 - 2x) = \lambda - C'\Delta \quad (6.17)$$

This equation does not have a simple analytical solution and has to be solved numerically.

### 6.3 Temperature-dependent Segregation

In this model, constant local strain is assumed to be only valid for systems with two elements that have a small lattice mismatch. In this chapter, the Au/Ag system is used as a model system for demonstration purposes. The lattice parameters of Au and Ag are 4.0782 Å and 4.0853 Å, respectively, and there is a lattice mismatch of 0.17% between the two elements.

The bulk moduli and Poisson's ratios for Au/Ag alloys of different compositions are determined by fitting the elastic moduli at different Au concentrations with a quadratic function. Table 1 shows the elastic moduli of Au/Ag alloys at different Au concentrations (at%). [176] The at% was converted to vol% in each calculation. The elastic modulus used in each calculation is extracted from the fitted lines. The lattice parameter is assumed to vary linearly between Au and Ag composition.

Table 6.1. Elastic moduli of Au/Ag alloys with different Au concentrations (at%) [176] and their corresponding Poisson's ratios and bulk moduli

at% Au	C <sub>11</sub> (GPa)	C <sub>44</sub> (GPa)	C <sub>12</sub> (GPa)	Poisson's Ratio	Bulk Modulus (GPa)
0	122.2	46.1	91.8	0.303	101.93
2	123.7	46.9	93	0.303	103.23
4	124.1	47.3	92.8	0.301	103.23
25	138.5	48.7	104.5	0.316	115.83
50	147.7	50.8	113	0.320	124.57
75	166.5	48.6	132.5	0.348	143.83
100	190	42.3	161	0.386	170.67

Fitted plots for bulk moduli and Poisson's ratios are shown in Figure 6.1.

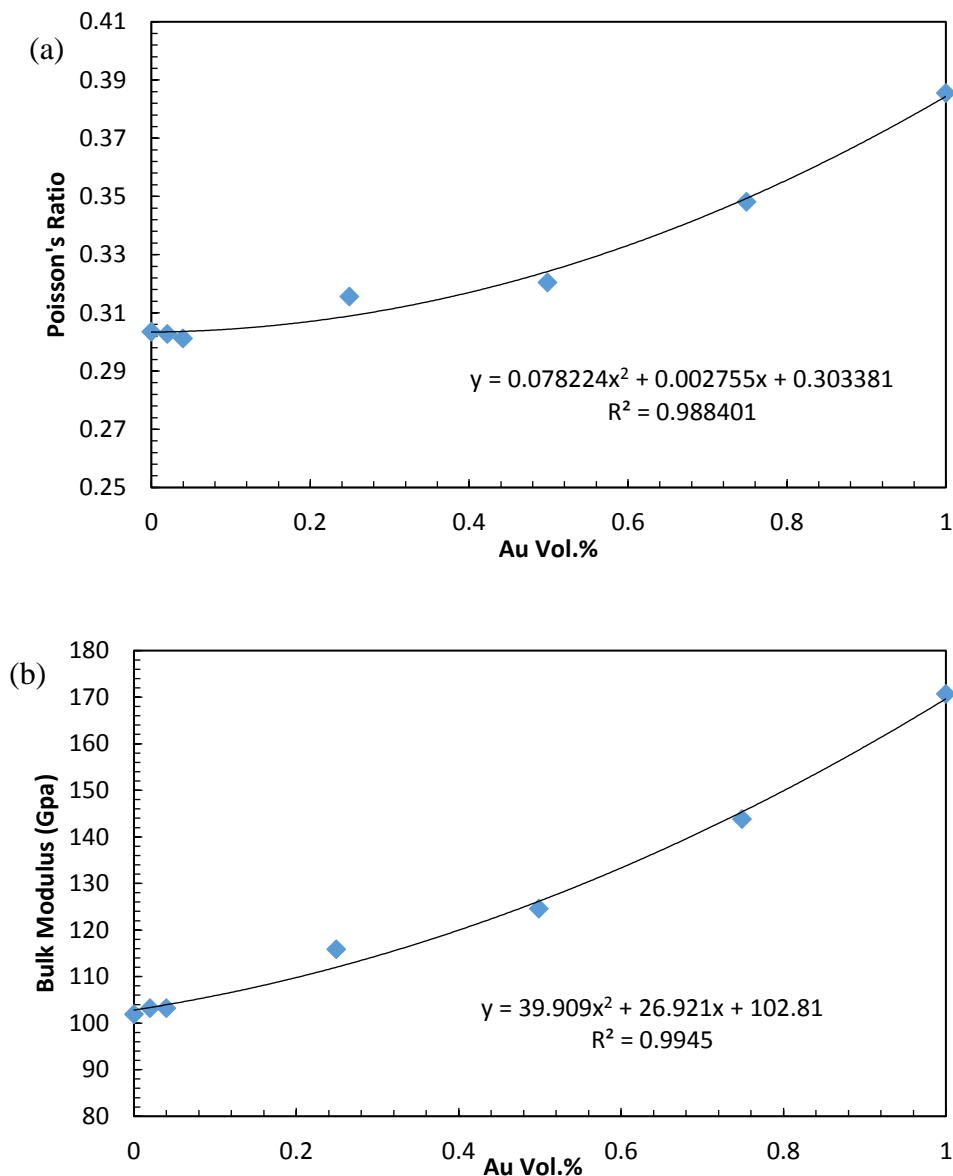


Figure 6.1 (a) Poisson's ratio of a Au/Ag alloy as a function of Au volume fraction (homogeneous concentration). (b) Bulk modulus of a Au/Ag alloy as a function of Au volume fraction

In Figure 6.2, the total change in energy and the contributions from both strain and the entropy of mixing as a function of Au homogeneous concentration are plotted for a Dh particle with a radius of 5 nm and a thickness of 3 nm at 300K and 1000K, respectively. The total change

in energy is small at all concentrations. The entropy of mixing always favors the mixing of atoms, so segregation inside a particle always results in an increase in free energy, neglecting the strain term. The change in strain energy term due to segregation has a larger magnitude compared to the entropy of mixing term, and therefore, the net change in energy is negative at thermal equilibrium. As temperature increases, the energy contribution from the entropy of mixing increases linearly with absolute temperature  $T$ , ignoring differential thermal expansion. Therefore, the segregation is less significant at higher temperatures.

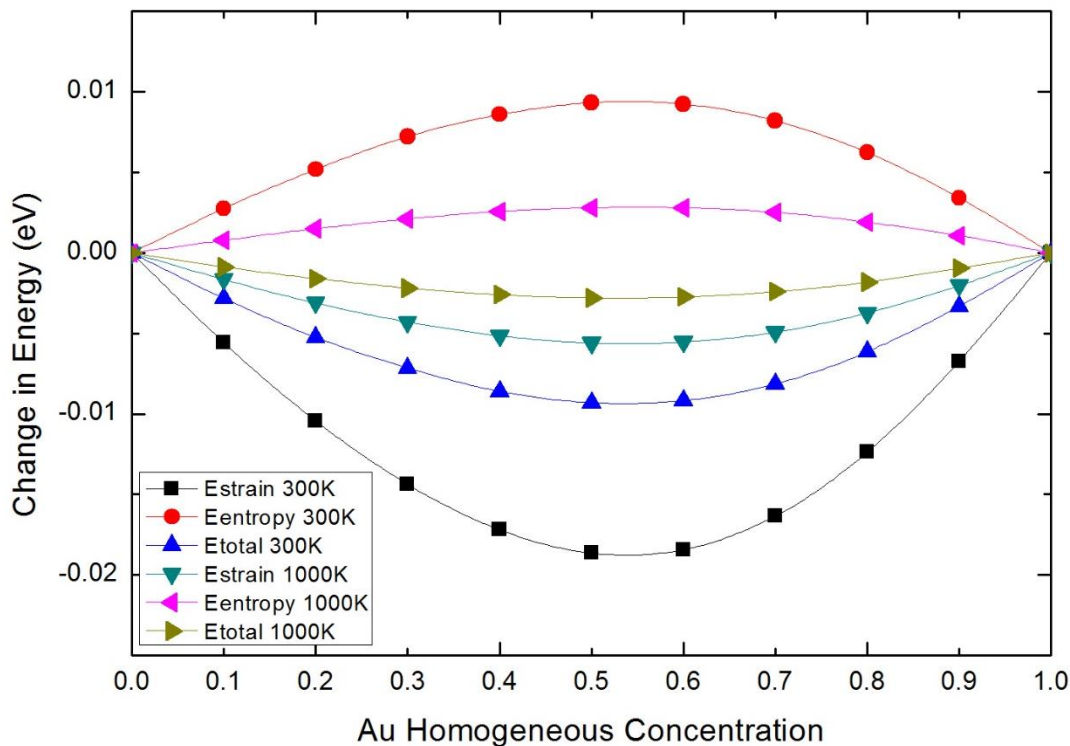


Figure 6.2 Change in energy of a Dh (5 nm in radius, 3 nm in thickness) as a function of homogeneous (initial) Au concentration at 300K and 1000K

While the total energy change from segregation is small, there is still a noticeable segregation within Dh and Ic particles, as shown in Figure 6.3. Figure 6.3 shows the strain-driven

segregation in Dh and Ic particles with Au homogeneous concentrations of 0.3 at different temperatures, and the calculated chemical potentials of the particles at different temperatures is given on the top right corner. The chemical potential of Au as a function of homogeneous Au concentration at various temperatures were calculated numerically and are plotted in Figure 6.4. The elastic strain energy in an Ic particle is one order of magnitude larger than the elastic strain energy in a Dh particle. As a consequence, the segregation in Ic particles is more significant than that of Dh particles.

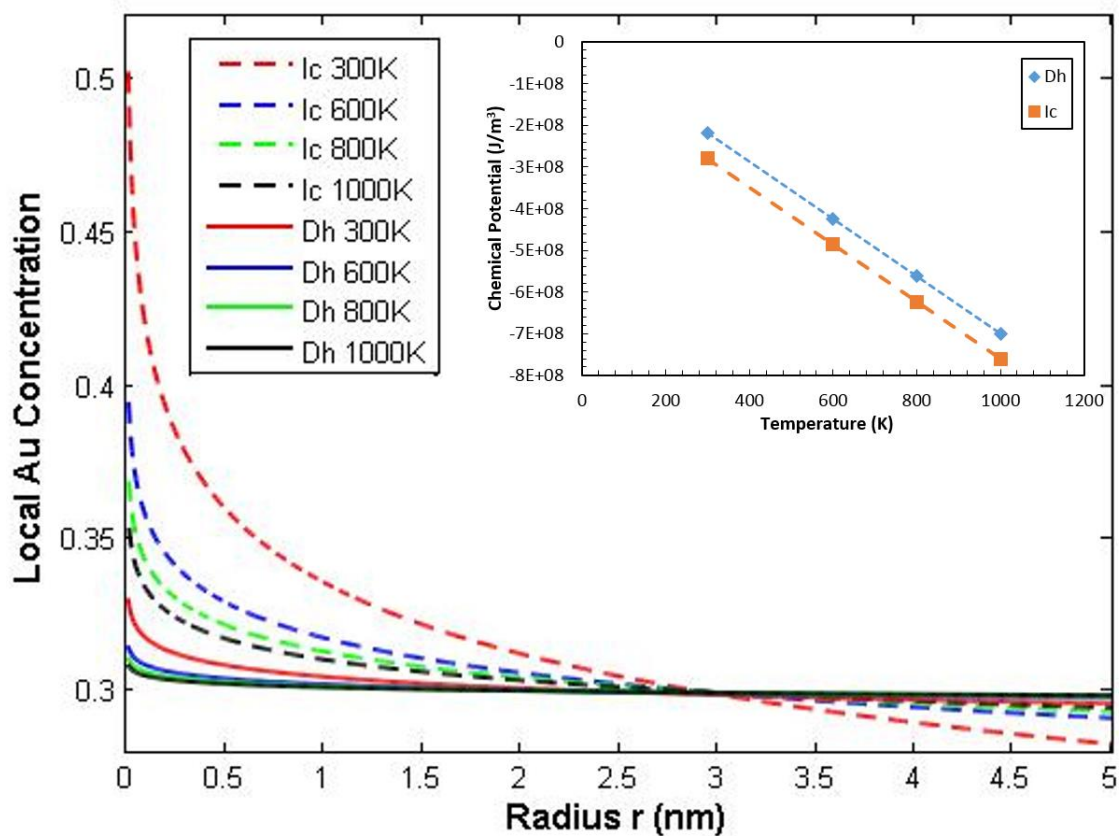


Figure 6.3 Temperature-dependent segregation inside Dh and Ic bimetallic nanoparticles. The local Au concentration is plotted as a function of particle radius, where  $r = 0$  represents the center of the particle. Dh particles (5 nm in radius with 3 nm thickness) are estimated as elastic cylinders with only plane strain. Ic particles (5 nm in radius) are estimated as elastic spheres that have radial strains

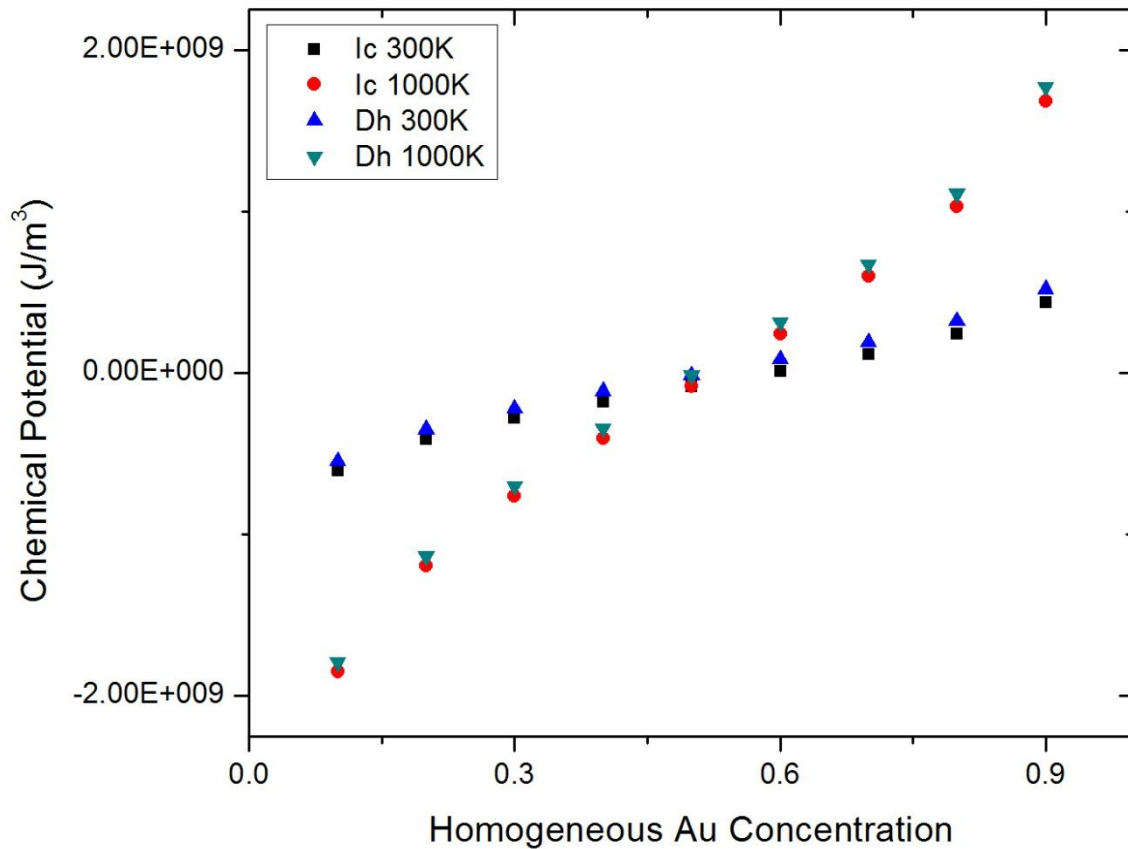


Figure 6.4 Chemical potential of Au as a function of homogeneous Au concentration at 300K and 1000K

#### 6.4 Degree of Segregation

To illustrate the degree of segregation inside a MTP, the variance of local Au concentration corresponding to the homogeneous concentration is taken and integrated over the whole particle. The degree of Au segregation is expressed as the square root of the ratio between the integrated variance and the total volume of the MTP,

$$Deg_{seg} = \sqrt{\frac{\int (x(r) - C_H)^2 dV}{\int dV}} \quad (6.18)$$

The degrees of segregation for Dh ( $r = 5$  nm, thickness = 3 nm) and Ic ( $r = 5$  nm) particles at 1000K (high temperature) and 300K (room temperature) as a function of Au homogeneous concentration are plotted and compared in Figure 6.5. The degree of segregation is proportional to the change in energy from the segregation.

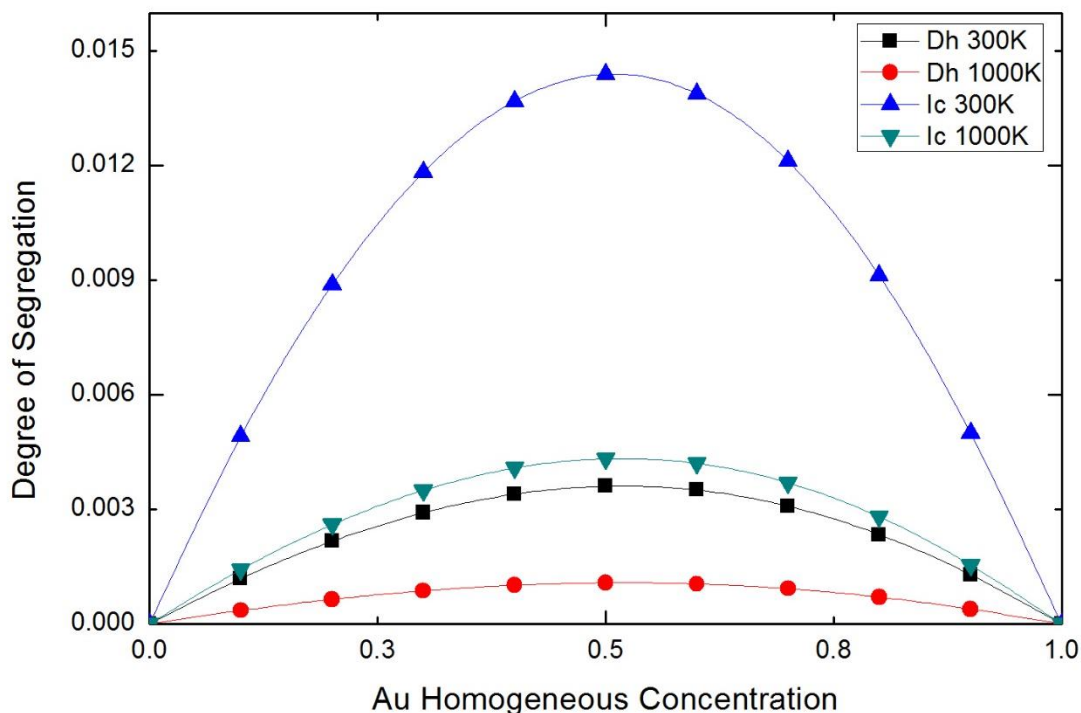


Figure 6.5 Degree of segregation of Dh and Ic particles as a function of Au homogeneous concentration at different temperature. The degree of segregation is linearly related to the total change in energy in a particle. Ic particles have higher inhomogeneous strain, resulting in a higher degree of segregation

## 6.5 Discussion

The compositional inhomogeneity inside bimetallic MTPs is driven by the strain induced segregation. The elastic strain fields in bimetallic MTPs drive atoms with smaller lattice parameters to segregate towards the center of the particles and larger atoms to the outermost surface. At low temperatures, the segregation is more significant. At high temperatures, the

contribution from the entropy of mixing drives the bulk composition toward homogeneity. Icosahedra, with higher solid angle deficiency, have higher degrees of segregation than decahedra.

There is some experimental evidence in support of the analysis here. High resolution electron microscopy studies have been performed targeted to understand the segregation behavior in bimetallic nanoparticles with different shapes or structures at the atomic scale. [94, 130, 177-179] There are some recent studies of Fe/Pt Ic nanoparticles showing that Pt segregates toward the surface,[180, 181] which is consistent with our prediction. While there is other work on Dh nanoparticles, they have not shown obvious segregation.[88] For completeness, in some cases, ordered phases are more thermodynamically stable at certain composition ratios.  $L1_0$  ordered structures were observed in both single crystal and multiply twinned Fe/Pt particles after annealing,[88, 182] and this is consistent with DFT[183] and Monte Carlo simulations.[184, 185] These  $L1_0$  phases are often formed at high temperatures, usually via a post-annealing process, and the segregation effects were predicted to be minimal at these temperatures.

Surface energy is a well-known factor that affects the segregation in bimetallic MTPs. In the case of Au/Ag alloy nanoparticles, the surface energy change from segregation is about 100 eV for a 5 nm Dh, which is around four orders of magnitude larger than the energy change from strain-induced bulk segregation. The energy change from the strain-induced segregation in Ic particles is around 50 times larger than the case in Dh particles. This is because of the higher degree of strain and segregation in an Ic particle. As shown in eq. 6.10, the strain energy scales as the cube of the lattice mismatch, so the contribution from strain energy could be much larger for systems with larger lattice parameters. For systems with large surface energy differences, surface energy driven segregation will dominate. However, if the surface energies of the two elements are

similar, strain driven segregation could be substantial. It is worth mentioning that while the change in energy is small, there is still a noticeable segregation of bigger atoms to the outermost surface, especially in Ic particles. Additionally, strain-induced segregation can either promote or reduce surface segregation. Besides systems with small lattice mismatch, such as Pt/Pd, which would follow the formulation derived above, there are many other possible combinations. For systems with larger lattice mismatch, such as Ag/Pd or Ni/Pt, the change in strain energy will be large, and the strain-induced segregation will be more pronounced.

At the large lattice mismatch limit, phase separation has also been observed in some numerical calculations for Ag/Ni, Ag/Cu and Ag/Co systems.[77, 78, 186] Phase separation causes larger atoms on the outside, where the stress is tensile, and the smaller atoms on the inside, where the stress is compressive. Although the systems in these studies do not form continuous solid solutions, it is still possible for core-shell structures to be formed in miscible alloys in some extreme cases.

## **6.6 Conclusion**

The possibility of strain-induced segregation in bimetallic MTPs is analyzed by an analytic first-order expansion within a continuum model. The results indicate that while the change in free energy is small, there is still a noticeable segregation of larger atoms to the outer most surface and smaller ones to the core, which can have interesting effects in heterogeneous catalysis.

## CHAPTER 7

### **Wide-field Super Resolution Plasmon Microscopy**

## 7.1 Introduction

A lot of efforts have been put into developing the *in-situ* observation of crystal growth using liquid cell transmission electron microscopy, which focused mainly on electrochemical reactions, nanoparticle nucleation, aggregation, etc. [187-191] The *in-situ* observation of nanoparticle nucleation and growth is a powerful tool to understand the nanoparticle growth mechanism. However, there are limitations of the liquid-cell experiments in TEM, such as the electron beams effects, including heating, charging or production of free radicals in solution. On the other hand, the growth reaction should be electron beam induced, which narrows down the number of reactions that can be studied using this technique.

In Van Duyne lab, there is a super-resolution plasmon microscopy (SRPM) set-up, which was previous utilized in *in-situ* nanoparticle tracking experiments. [192, 193] It will be an alternative method to directly monitor the nanoparticle motion and growth. This set-up includes an inverted microscope equipped with a dark-field condenser, which only collects the scattered light from metal nanoparticles. The scattered light passes through the objective lens into a set of acousto-optical tunable filters, and only one wavelength can be collected by the CCD camera at a given time. This allows the simultaneous measurements of the LSPR spectra and the locations of a moving particle. Bingham *et al.* has used this set-up to measure the scattering spectra of multiple Ag nanoparticles in parallel and to track their motion simultaneously. The single-particle diffusion coefficient was determined from the nanoparticle motion trajectory.[193] This set-up has also been used to perform single-particle tracking experiments with Au nanoparticle-labeled solid supported lipid bilayers (SLBs) containing increasing concentrations of ganglioside (GM<sub>1</sub>). The motion of the Au nanoparticles were measured and the introduction of GM<sub>1</sub> molecule confined the motion

of the Au nanoparticles. The percolation threshold was found to be 22% GM<sub>1</sub>, and the confining diameter at the percolation threshold is about 50nm.[192] The schematic of the set-up is shown in Fig. 7.1.

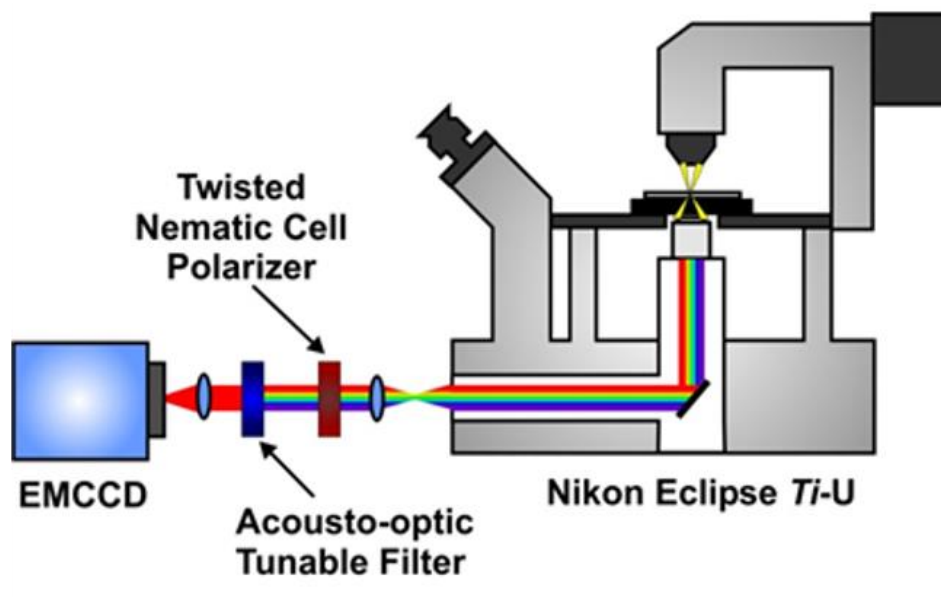


Figure 7.1 The schematic of the wide-field LSPR set-up

This set-up can also be utilized to monitor the *in situ* nanoparticle growth in solution. The spectra and diffusion coefficient as a function of time could be measured. Understanding the nanoparticle growth mechanism is very important because, at the present time, the elementary steps that determine which pathway the growth follows are not well understood. The understanding of growth mechanism could benefit the rational design of novel nanoparticles, and further improve the performance of various applications.

## 7.2 Methods

### 7.2.1 Synthesis of Ag Nanoprism

The synthesis of Ag nanoprisms was carried out by following a previously reported method.[194] Silver nitrate (99.998%), trisodium citrate dehydrate (99.9%), Bis(*p*-sulfonatophenyl)phenylphosphine dehydrate dipotassium (BSPP) (97%), and sodium borohydride (99%) were purchased from Sigma Aldrich. AgNO<sub>3</sub> (1.0mL, 0.01M), sodium citrate dihydrate (1.5mL, 0.02M) and 94 mL of de-ionized water were combined in an Erlenmeyer flask, and the flask was immersed in an ice bath. N<sub>2</sub> was flowed for 20min before the reaction. Freshly prepared, cold NaBH<sub>4</sub> (1.0mL, 0.02M) was then added to the solution, and 5 drops of NaHB<sub>4</sub> solution were added every two minutes for a total of 14 minutes. BSPP (1.0mL, 0.005M) was added dropwise after 15 minutes along with an additional 1.0mL of NaBH<sub>4</sub>. The reaction solution continued to be stirred for 5 hr on an ice bath and a dark yellow solution was produced. The Ag seeds were stored in a refrigerator to age overnight.

For *ex-situ* growth of Ag nanoprisms, 3mL of Ag seed solution was transferred to a small vial and illuminated with 550 nm of light for 5-8 hr. The time-resolved absorption spectra were collected by the Cary 5000 UV-Vis-NIR spectrometer. The as-synthesized Ag nanoprism growth solution was drop-casted onto ultrathin carbon grids (Ted Pella). The morphologies of the synthesized particles were characterized via a JEOL JEM-2100F field emission transmission electron microscope.

### 7.2.2 Synthesis of Au Nanorod

The Au nanorods synthesis was performed by Ji En (Jennifer) Park. In a typical procedure, HAuCl<sub>4</sub>·3H<sub>2</sub>O (0.25mL, 0.01M) aqueous solution was added to 7.5 mL of a 0.1 M CTAB solution

in a glass vial. The solution was gently mixed. Then ice-cold  $\text{NaBH}_4$  (0.6 mL, 0.1 M) aqueous solution was added, and the vial underwent inversion mixing for 2 mins. The solution appeared in a pale brown-yellow color and it was kept on a hotplate at 25 °C for future use.

For the synthesis of Au nanorods, CTAB (4.75 mL, 0.01M),  $\text{HAuCl}_4 \cdot 3\text{H}_2\text{O}$  (0.2 mL, 0.01M), and  $\text{AgNO}_3$  (0.03mL 0.01M) solution were added to a vial in this order, followed by gentle inversion mixing. L-ascorbic acid (0.032 mL, 0.1M) was then added to the vial. Finally, 0.1 mL of seed solution was added to the mixture and gently mixed by inversion for 10s, and then the reaction solution was kept on a hotplate at 27 °C for 5 hrs. The absorption spectra of the solution were taken using a Cary 5000 UV-Vis-NIR spectrometer. The as-synthesized Au nanorods growth solution was drop-casted onto ultrathin carbon grids (Ted Pella). The morphologies of the synthesized particles were characterized via a Hitachi 8100 transmission electron microscope.

### **7.2.3 Ultra-thin Liquid Cell**

Owing to the shallow depth of field of the 100x oil immersion objective lens, a very thin liquid cell was required to avoid losing the particle of interest. The liquid cell is composed of a glass slide, a 12.5  $\mu\text{m}$  Teflon spacer (also act as o-ring, purchased from Lebow), and a No.0 coverslip. The schematic of this cell is shown in Figure 3.7.

1x3 inch glass slides and 22x22 nm No.0 glass coverslips were sonicated in IPA for 60 mins. The 12.5  $\mu\text{m}$  thick Teflon o-ring was made by the punching tools. The Teflon o-ring was placed on top of the glass slide, and 2.5  $\mu\text{L}$  of growth solution was dropped onto the glass slide. The cell was sealed by gently placing the No.0 coverslip on the top of the o-ring, and it was further sealed by scotch tapes. The center of the cell was thinner than the areas close to the o-ring, where the particles move in approximately 2D around the center of the cell. The No.0 coverslip was

facing to the oil immersion objective so that the particles will be within the working distance of the objective.

#### **7.2.4 SEM-correlated Study of Ag nanoprism growth**

In order to monitor the same particle over a long time, particles were immobilized onto a conductive transparent substrate, i.e. a glass coverslip coated with a thin film of indium tin oxide (ITO). The particles on the conductive substrate can be characterized using SEM after the growth experiment. A distinct pattern was etched onto the ITO surface to facilitate identification of the same location when measuring the particles using both the WF set-up and SEM.

The ITO substrate was cleaned by sonication in IPA for 50 min, followed by rinsing with IPA and H<sub>2</sub>O. The plate was base treated for 10 minutes and heated at 60°C so the surface was functionalized with hydroxyl (-OH) group. The plate was rinsed with H<sub>2</sub>O and IPA multiple times before it was transferred to a solution of IPA (50mL) and (3-mercaptopropyl) trimethoxysilane (0.5mL) for 6-10 minutes and heated at 70°C. The ITO substrate was then rinsed with IPA and dried with N<sub>2</sub>. 130 µL of nanoparticle seed solution was transferred to the functionalized ITO surface and it was allowed to be dried for 40 min in a N<sub>2</sub> box to prevent oxidation of the nanoparticles. The ITO surface was rinsed with water and dried with N<sub>2</sub>.

Ag seed solution was diluted, and 130µL of the diluted solution was drop casted onto the functionalized ITO surface and was allowed to be dried for 40 min in a N<sub>2</sub> box to prevent the oxidation of the Ag seeds. Then the ITO surface was rinsed with deionized water and dried with N<sub>2</sub>. This ITO conjugated with Ag seed particles was assembled in the liquid cell, presented in Figure 3.8.

## 7.3 Experimental Results

### 7.3.1 Spectra and Diffusion Trajectories of Au nanospheres

The acquisition of spectra and motion of the particle inside the thin liquid cell was first demonstrated on 90nm Au nanospheres. The AOTF swept from 450 to 750 nm with 3 nm increment, and the exposure time at each wavelength was 0.033s. The normalized spectra and mean square displacements of three particles are shown in Figure 7.2.

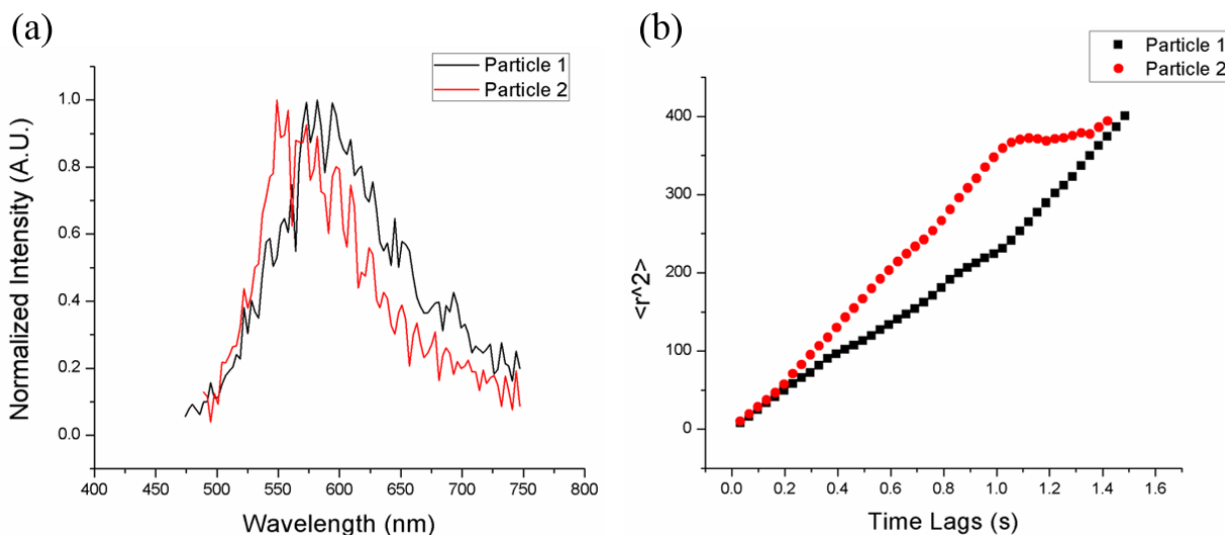


Figure 7.2 (a) normalized LSPR spectra of two single Au nanospheres, and (b) their corresponding mean square displacements

The slope of the mean square displacement equals to  $4D$ , where  $D$  is the diffusion coefficient of the particle in solution. The diffusion coefficient of the two particles were  $6.1 \times 10^{-9} \text{ cm}^2/\text{s}$  and  $7.9 \times 10^{-9} \text{ cm}^2/\text{s}$  respectively.

The same measurements has been made on Ag nanoprisms. The diffusion coefficient for particle 1, 2, and 3 were determined to be  $2.0 \times 10^{-8} \text{ cm}^2/\text{s}$ ,  $2.5 \times 10^{-8} \text{ cm}^2/\text{s}$ , and  $1.7 \times 10^{-8} \text{ cm}^2/\text{s}$  respectively.

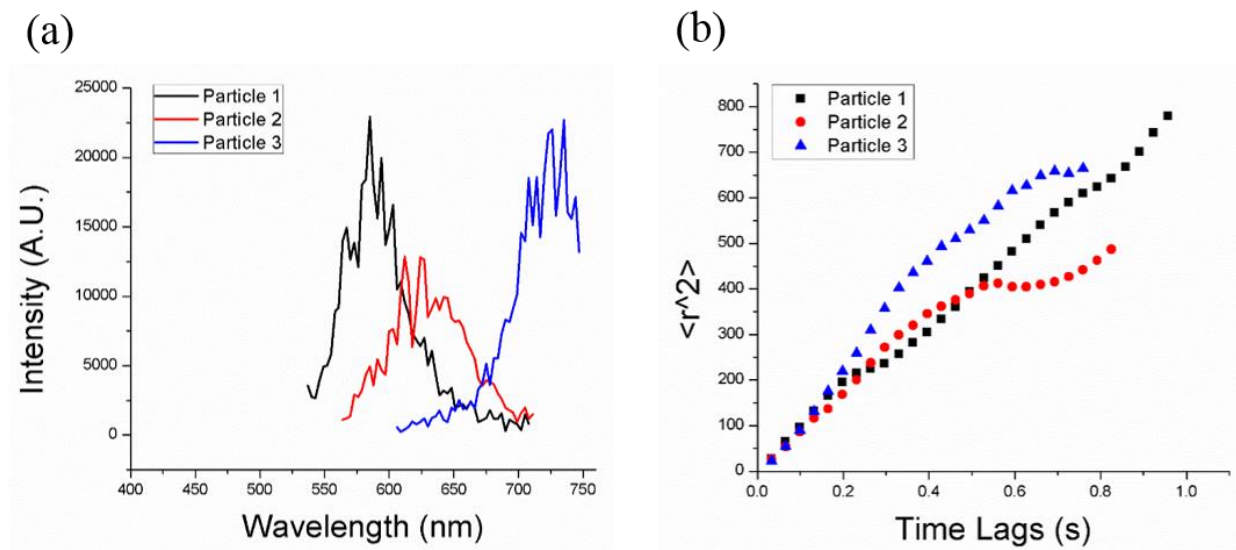


Figure 7.3 (a) LSPR spectra of three single Ag prisms, and (b) their corresponding mean square displacements

### 7.3.2 Time-dependent Study of Au Nanorod Growth

In order to study the Au nanorods growth *in situ*, 2.5 $\mu$ L of Au nanorods growth solution was deposited onto the surface of a 3x1 inch glass slide, which was sonicated in IPA solution for 1 hr. A 12.5  $\mu$ m thick Teflon spacer was placed around the liquid droplet, and then a No.0 glass coverslip was carefully placed on top of the Teflon spacer. The No.0 coverslip was taped onto the glass slide by scotch tapes. The scotch tapes were applied very gently to avoid leaking of liquids. The assembled liquid cell was transferred to an inverted dark field microscope. The No.0 coverslip was facing down toward the 100x oil objective, so that the Au nanorods will be moving within the focal distance of the oil objective. The glass slides and coverslips were cleaned by sonication in IPA, because the glass surface cleaned by the standard piranha bath would be negatively charged. The positively charged Au nanorods stuck onto the negatively charged glass surface instantly, and the tracking of moving particles would not be possible.

A series of 100 images were taken with 0.033s exposure and with 0.033s interval. Four frames at 551, 593, 722 and 782 nm wavelength were extracted from the image stack and they are shown in Figure 7.4 for 1 hr, 2 hr and 3 hr after the reaction begins, respectively. As shown in Figure 7.4, at 1 hr reaction time, the nanorods hasn't been grown into a size that was resolvable by the EMCCD. At 2 hr reaction time, the Au nanowires started to appear on the EMCCD and the concentration of nanowires appear to be too high. The data analysis was merely impossible because tracking of one particle was interfered by another just after a few frames.

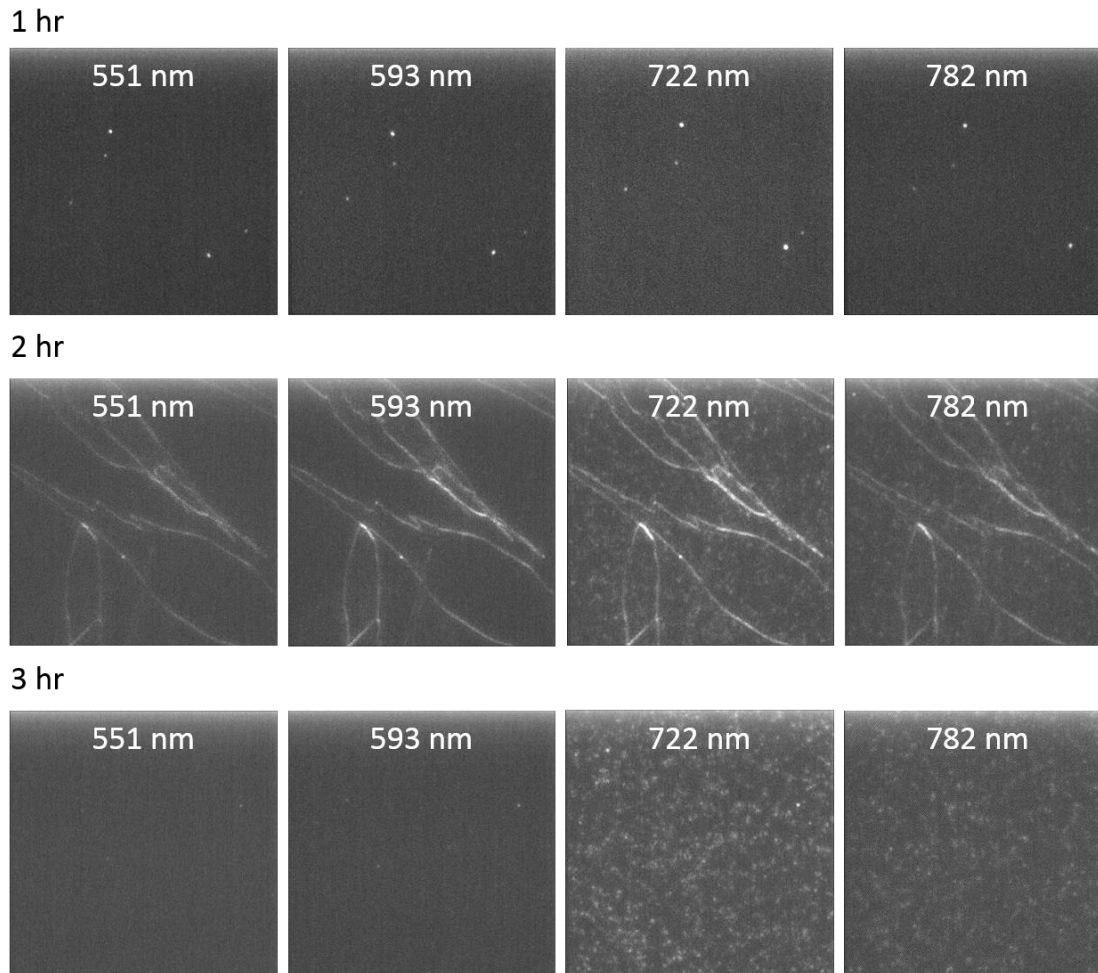


Figure 7.4 Four frames (551 nm, 593 nm, 722 nm, 782 nm) from the 100 frame image stack, which were taken at 1 hr, 2 hr, and 3 hr after the beginning of the reaction, respectively. The flakes appeared in 2 hr images were CTAB. (Video 1-3)

Several modification of the synthesis has been made to lower the particle concentration and at the same time, preserve the nanorod morphologies. In order to slow down the nanoparticle movements, the reactions had been carried out in more viscous mediums. After adding the seed solution to the growth solution, the solution was diluted 100 times by water, 1M glucose and 40% glycerol solution, respective, and the resulting shapes were shown in Figure 7.5.

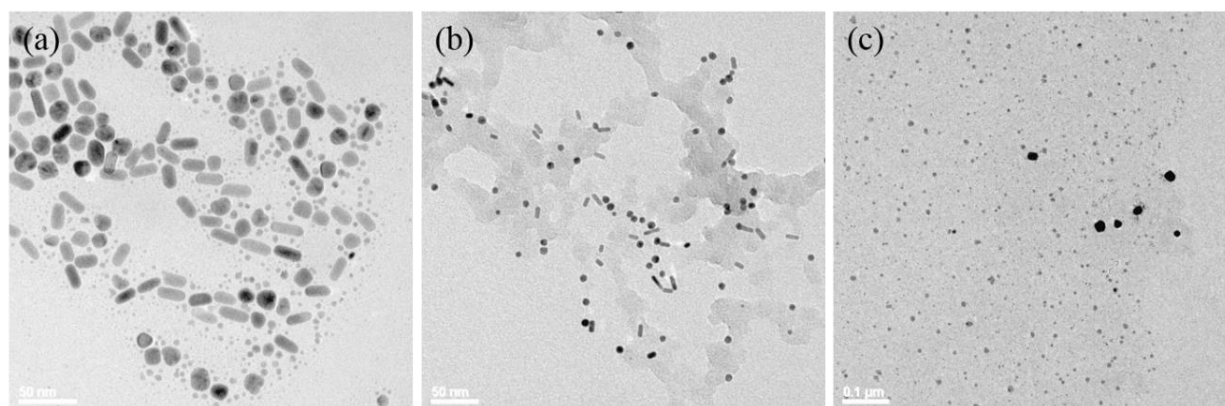


Figure 7.5 TEM images of Au nanorods. Au nanorods reaction solution were diluted 100 times in (a) water, (b) 1M glucose and (c) 40% Glycerol aqueous solution, respectively.

It appears that the reaction had the best yield in water, therefore, the further modified reaction was done in water. The following table shows the modified conditions and the resulting shapes are shown in Figure 7.6.

Table 7.1 Modified reaction conditions for CTAB stabilized Au nanorods synthesis

Modified Conditions		
Seed Solution	Growth Solution	Diluted in
2x	1x	Water
10x	1x	Water
100x	100x	Water/1M Glucose/40% Glycerol
100x	2x	Water
100x	5x	Water
100x	10x	Water
100x	20x	Water

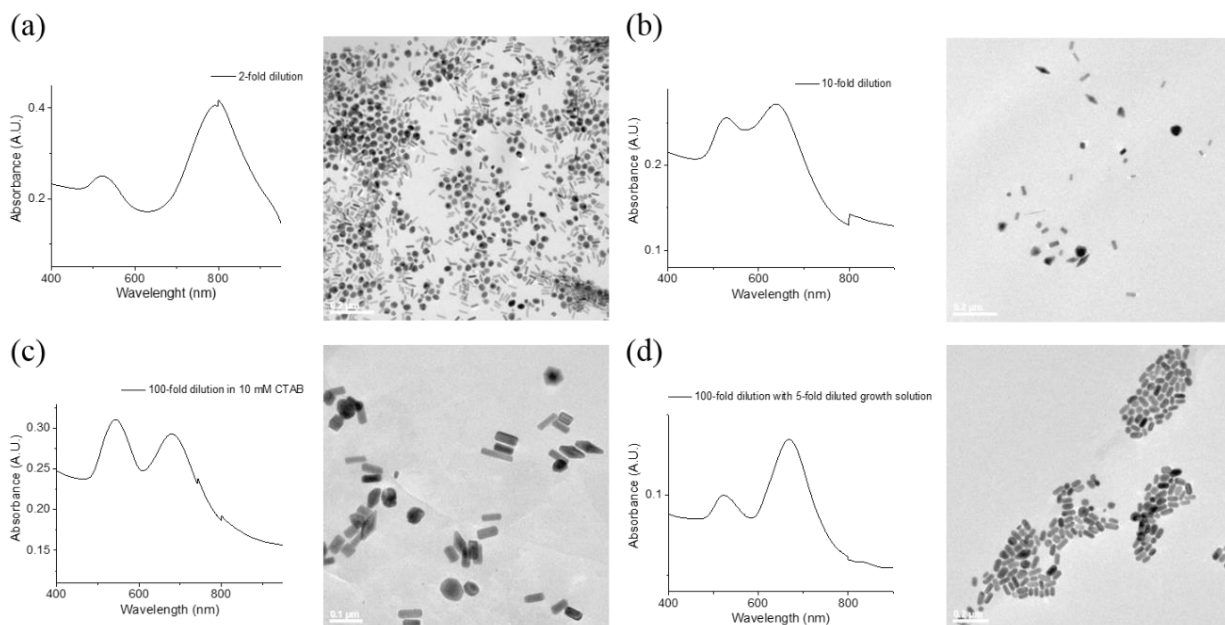


Figure 7.6 TEM images of Au nanorods synthesized with different dilution. (a) 2 times diluted seed solution was added in undiluted growth solution; (b) 10 times diluted seed solution was added in undiluted growth solution; (c) 100 times diluted seed solution was added in undiluted growth solution, and (d) 100 times diluted seed solution was added in 5 times diluted growth solution.

### 7.3.3 Time-dependent Study of Ag Nanoprism Growth

The experiment was first carried out *ex-situ*, the shapes of the nanoparticles at different reaction time are show in Figure 7.7. Before the illumination, there were seed particles in solution, and majority of them were sub-10 nm in size. The solution had an absorption peak around 400nm. The seed particles could be observed from the eye piece, but cannot be resolved on the EMCCD, and there were two reasons. First, the scattering intensity of Ag seed particles is very low, so that a much brighter light source other than halogen lamp or a very long exposure time would be required to give high enough signal, compared to the background noise. Second, in this wide-field set-up, the lower limit of the available wavelength is 450 nm, only the tail of the extinction peak could be captured. Examples of single particle spectra (exposure time = 5s) of Ag nanospheres

with diameter around 15 nm are shown in Figure 7.8. Therefore, only particles which have grown into a certain size can be resolved.

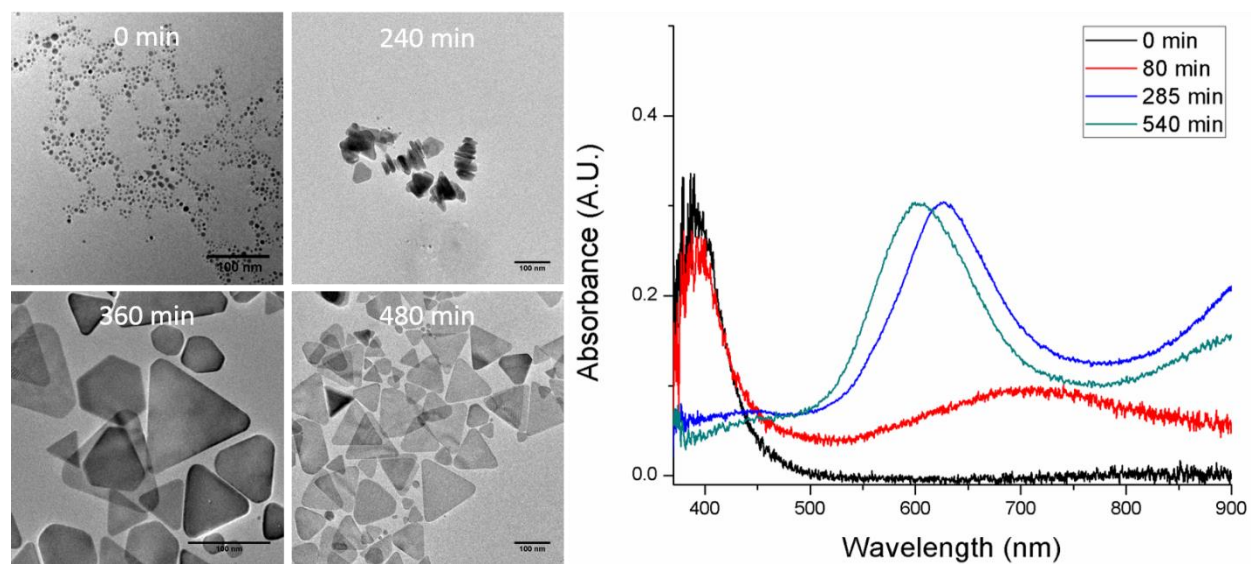


Figure 7.7 (a) Time series images of Ag nanoparticles in solution for the photo-mediated synthesis, and (b) UV-Vis spectra at different reaction time

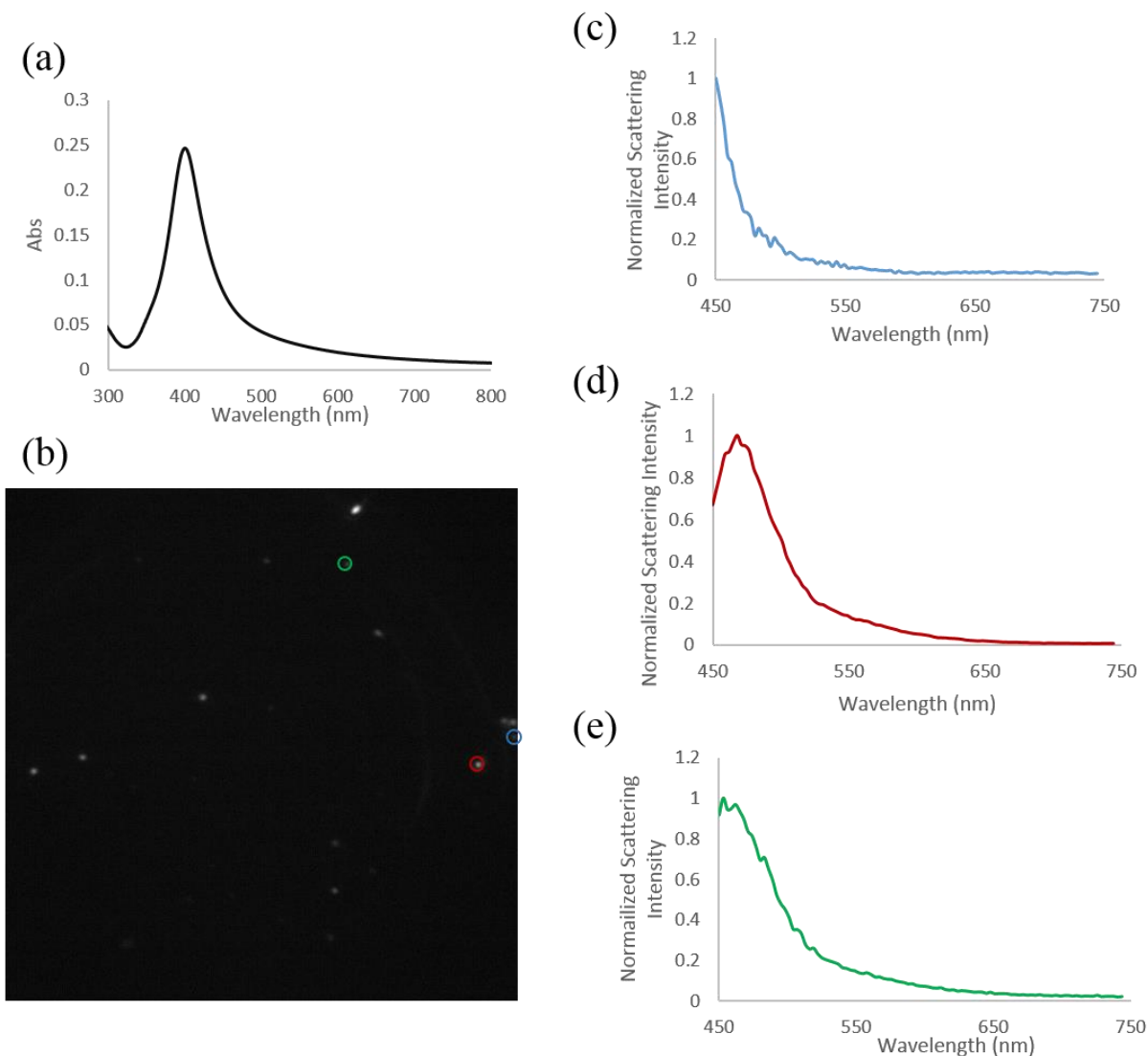


Figure 7.8 (a) UV-Vis spectrum of Ag nanosphere with a diameter around 15 nm, (b) The tiff image acquired by the EMCCD at 450 nm, (c) - (e) Single particle spectra of the corresponding particle labeled in (b)

In order to study the same particle over the course of reaction, the Ag seed particles were confined to the ITO surface with 3-Mercaptopropyltrimethoxysilane (MPS). The molecular structure of MPS is shown in Figure 7.9 (a). Figure 7.9 (b) shows the Ag nanoprisms synthesized in the liquid flow cell after illuminated with 550nm light for 5 hr. A pattern was etched on the ITO

surface so that the same location can be identified when analyzing the particles using both the dark field microscope and SEM. In Figure 7.10, the LSPR-SEM correlated study is illustrated. The collection of the spectra on number of particles at several different labeled regions were performed prior to the SEM characterization of the same areas. In Figure 7.10, the spectra of two static particles were collected during reaction. As we observed from Figure 7.10, the LSPR of the particles underwent a blue shift. This was consistent with the time-resolved UV-Vis study that there was a blue shift after the particle reached some certain size. This could be due to the corner rounding of the particles got bigger during reaction. More work has to be done on measuring the particles at an earlier stage of the reaction.

(a)

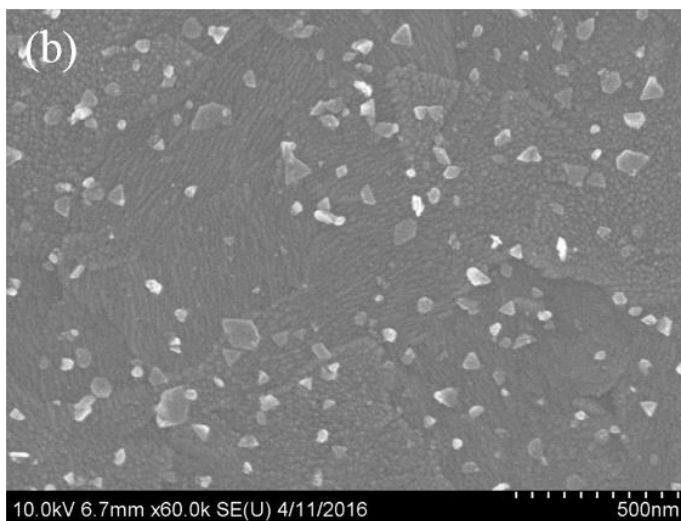
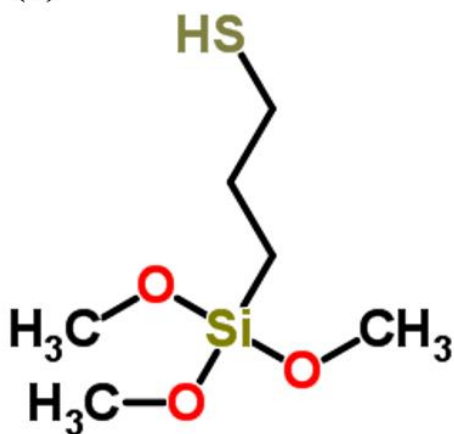


Figure 7.9 (a) The molecular structure of 3-Mercaptopropyltrimethoxysilane (MPS), and (b) SEM image showing the Ag nanoprisms synthesized in the liquid flow cell after illuminated with 550nm light for 5 hr

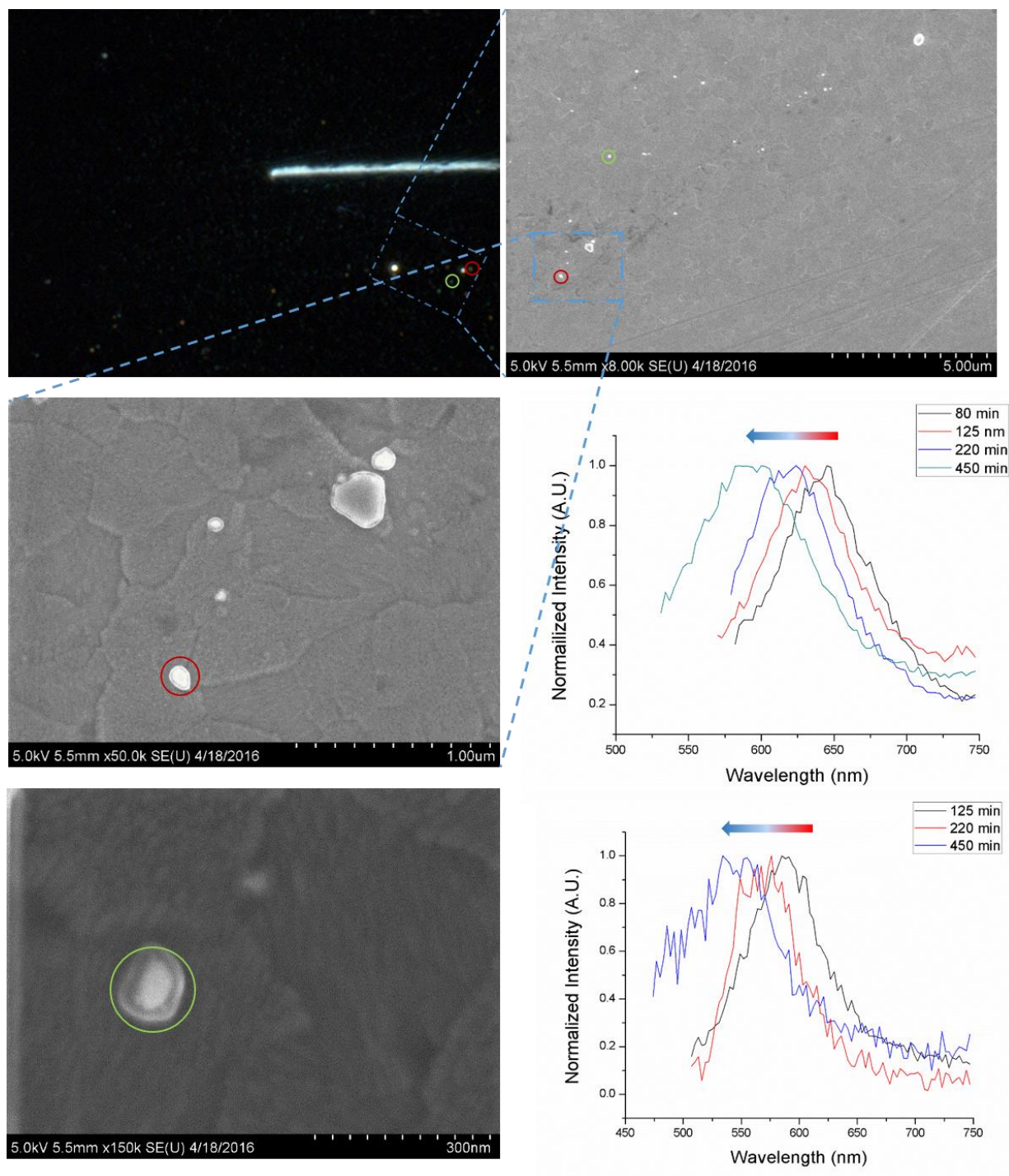


Figure 7.10 Illustration of SEM-correlation single nanoparticle LSPR measurements. The Ag seed particles were immobilized on the ITO surface and a distinct pattern was etched on the ITO surface to facilitate identification. The area under the etched line was characterized via STEM after the growth. The time-resolved single particle spectra of two Ag nanoparticles were present and both of them underwent a blue shift

### 7.3.4 Morphology Change from AgO Reduction

It is well known that Ag nanoparticles are prone to be oxidized and will lead to significant change in chemical and plasmonic properties.[195-197] In this study of Ag seed morphologies, the size of most seed particles were smaller than 10nm, so they were very easily to be oxidized when sitting in ambient air.

From counting the morphologies of the seed particles, there were a good amount of polyparticles, which were particles with complicated twinned structures, shown in Fig. 7.11(a), present in some of the samples. They did not exist in all the samples which means they were not likely to be formed from coalescence of small particles. A time series of oxidation experiment showed they were formed from the reduction of oxidized Ag nanoparticles in TEM, because AgO was very electron sensitive. The histogram shown in Fig. 7.11(b), shows the distribution of polyparticles among all seed morphologies increased as the oxidation time increased. The four different TEM samples were prepared at the same time, and was sit in air for 0, 27, 49 and 145 hours, respectively. The morphology distribution from the 27-hr sample did not follow the trend exactly because the counts of the sample was not enough.

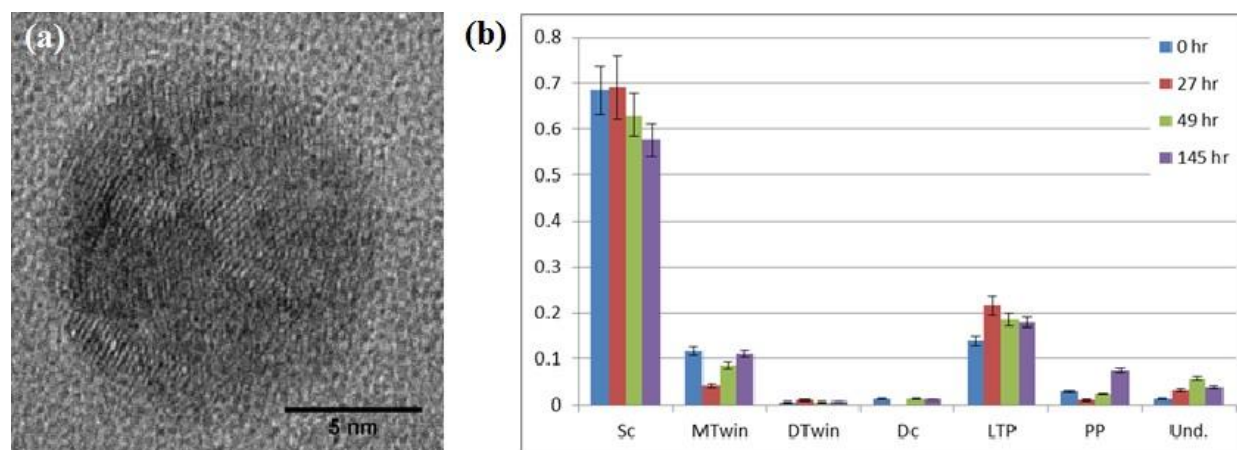


Figure 7.11 (a) A HREM image of a polyparticle. (b) Morphology distribution of Ag seed particles at different period of oxidation time

The as-synthesized Ag seed particles were also intentionally oxidized by  $O_2$  plasma. As shown in Figure 7.12 (a), majority of the as-synthesized Ag seed particles were single crystals. However, after  $O_2$  plasma treatment, all the seed particles transformed to polyparticles in TEM. It further verified that the appearance of polyparticles from aged Ag seed solution was due to the Ag oxidation.

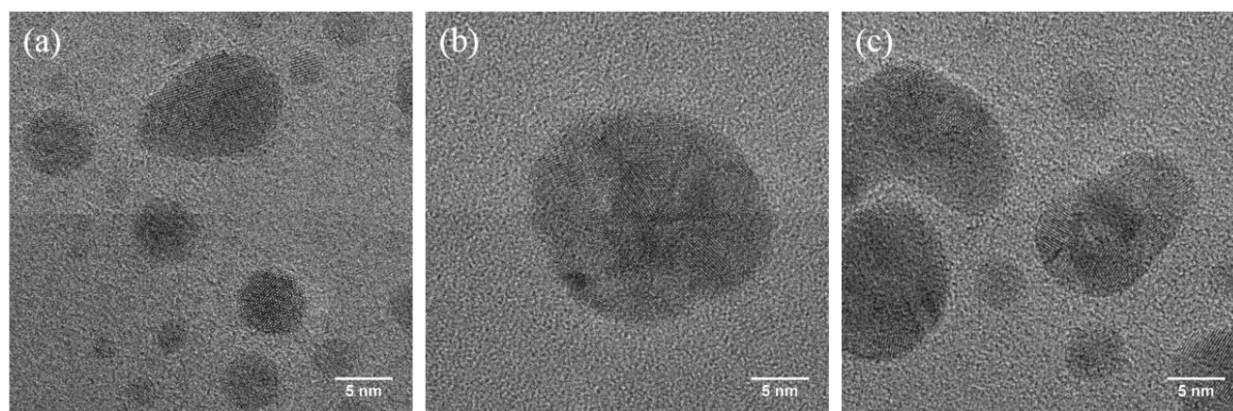


Figure 7.12 (a) Morphologies of the as-synthesized Ag seeds. The majority of the seed particles had single-crystalline structure. (b) and (c) shows the morphologies of the Ag seed particles after  $O_2$  plasma treatment, and all of them appeared to be polycrystals.

## 7.4 Different Light Source

Three different light sources have been used in this study, which are a halogen lamp, a Xe lamp and a super-continuum white light source, respectively. The previous published results generated from this set-up used a halogen lamp as the light source. [192, 193] The lamp profile depends upon the power of the light source and it has to be acquired every time after the data acquisition. One typical lamp profile of each source are presented in Figure 7.13.

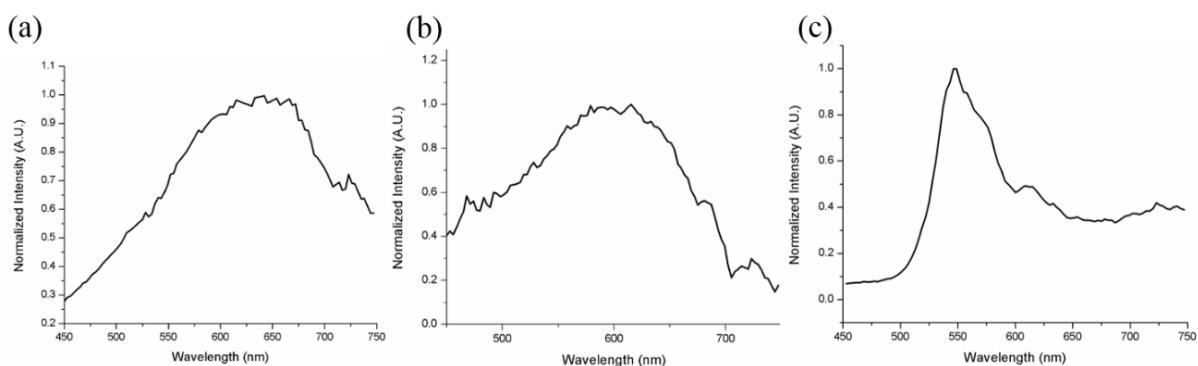


Figure 7.13 Typical lamp profiles of (a) Halogen lamp, (b) Xe lamp, and (c) super-continuum white light source

The lamp profiles of the halogen and Xe lamps are very similar. However, they are very different from the lamp profile of the super-continuum white light source. The super-continuum white light source has very low intensity below 500nm. The lamp profile of super-continuum white light source is dependent upon the output power as well as the wavelength of the femto-second laser. An axicon lens was installed to further minimize the photon loss. The spectra obtained using the super-continuum white light source appeared to be very noisy.

## 7.5 Future Work

As mentioned in Section 7.3.3, the concentration of Au nanorods in the synthesis described above was too high, and there were too many particles being captured in the same field of view. Also, at the beginning stage of the reaction, the particles moved very fast. The synthesis of Au nanorods will be modified so that the concentration of Au seed particles which further grow into Au nanorods will be significantly reduced. Therefore, the difficulty of tracking of nanorods will significantly decrease. Some preliminary results have been shown in Section 7.3.3, and the modified condition needs to be tested in the ultra-thin liquid cell. On the other hand, the static single particle spectrum of Au nanorods are very noisy when using 0.033s exposure time, multiple measurements on the same particles should be performed. The spectrum of the Au nanorods will be the average of the multiple spectra, and the noise of the spectrum will be reduced significantly.

One thing worth mentioning was that there were CTAB precipitated out during the reaction because the temperature of the room was below 27°C. A small heater was placed near the region of the interest to heat up the solution locally. An alternative way would be placing a space heater in the room to heat up the entire room to around 27°C.

Many other synthesis could be monitored by this wide-field set-up. Ag nanorods scatter better than Au, and they will be ideal for single particle tracking experiments. One possible synthesis that could be studied by this set-up was a Ag nanorod synthesis developed by Jana *et al.*[198] The TEM images of Ag nanorods synthesized by adding different amount of Ag seeds are illustrated below.

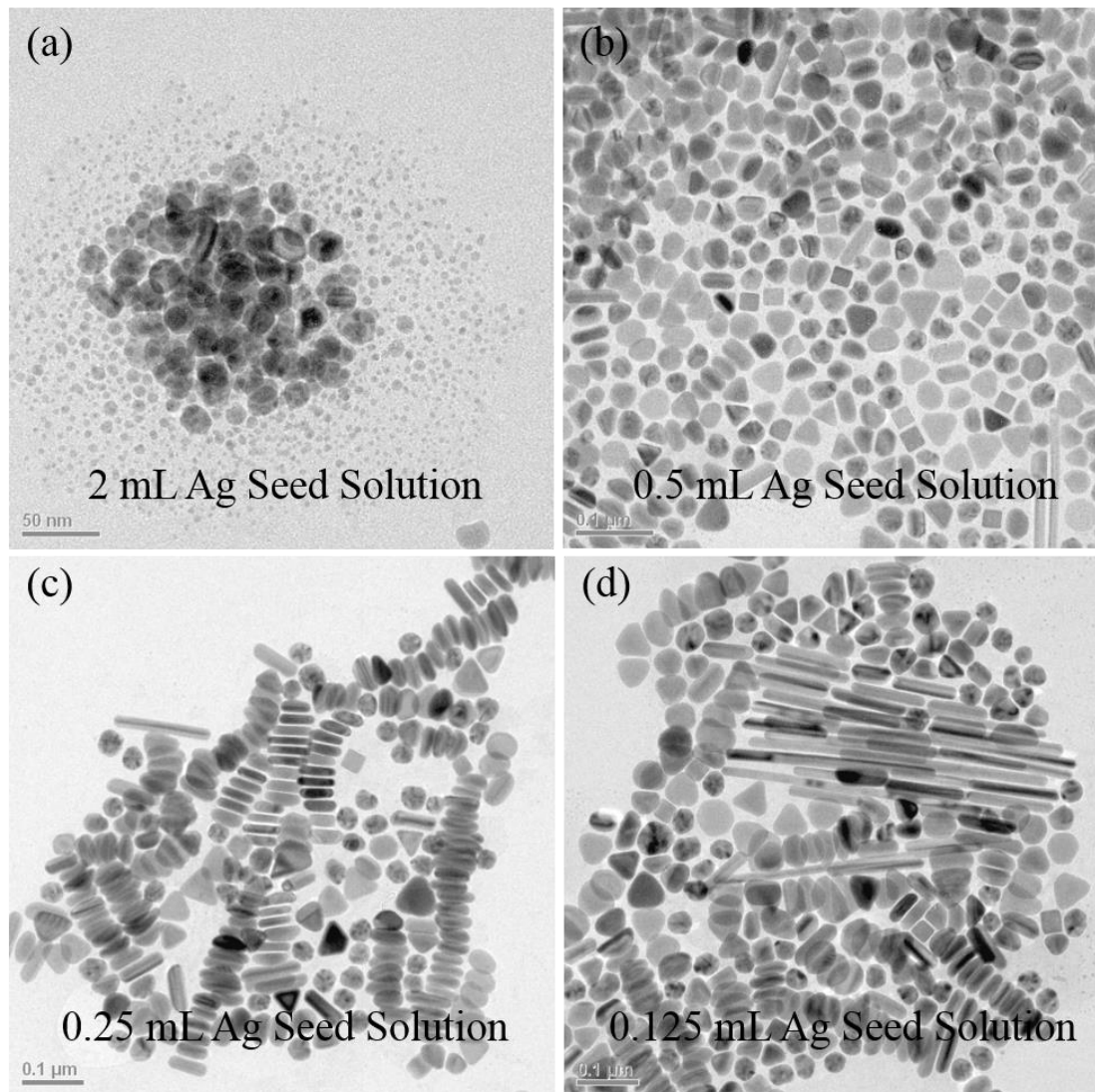


Figure 7.14 TEM images of Ag nanoparticles synthesized using different amount of Ag seed solutions. The yield of Ag nanorods increases with decreasing amount of Ag seeds added. The aspect ratio of synthesized Ag rods increases with decreasing amount of Ag seeds added

The nanoparticle moves very fast in water and it moves out of the depth of field very quickly. The ultra-thin liquid cell was designed to overcome this problem. However, the ability to measure 3D movements of particles will be beneficial for various studies. For instance, when the particles have anisotropic shapes, the 3D diffusion trajectories will provide valuable information. Also, this technique could be used for determining 3D structures of biological systems. The

principle of 3D tracking is to de-convolute the point light source to two points by applying a double-helix point spread function, which was first developed in Moerner group for single-molecule fluorescence imaging, beyond the diffraction limit. [199] The point spread function could be applied by either installing a spatial light modulator (SLM) or a physical phase mask. SLMs will enable dynamic modulation of the pupil functions and can cover a wide range of wavelengths. However, it only works with linear polarized light, and the efficiency is low. Additionally, a series of pupil functions need to be simulated. In contrast, by using a carefully fabricated phase mask, majority of the photons will be remained and collected and no modification of the set-up is required. On the other hand, it only works with specific wavelength and NA, and the cost of fabrication is rather high.

The MATLAB codes for data analysis needs improvements. The contrast of the individual tiff images needs to be adjusted when being visualized in MATLAB, in order to enable better efficiency of data analysis. The particle location can also be better defined by setting threshold on the image. In addition, the code could be modified to do automatic tracking.

## 7.6 Video Captions

**Video 1:** 1hr\_111816\_AuNRgrowth\_insitu.avi

Video of the moving Au nanowire after 1 hr of reaction, shown in Figure 7.4.

**Video 2:** 2hr\_111816\_AuNRgrowth\_insitu.avi

Video of the moving Au nanowire after 2 hr of reaction, shown in Figure 7.4.

**Video 3:** 3hr\_111816\_AuNRgrowth\_insitu.avi

Video of the moving Au nanowire after 3 hr of reaction, shown in Figure 7.4.

## CHAPTER 8

### **Conclusions and Future Directions**

## 8.1 Conclusions

Metal nanoparticles have been intensely studied in recent years. Owing to their unique optical, electronic and catalytic properties, they are widely used in various applications, related to chemical and biological sensing, catalysis, photonics, electronics, and Surface-enhanced Raman Spectroscopy, *etc.* Bimetallic nanoparticles are of interest because of the additional compositional degree of freedom, which enables tuning of the physical and chemical properties. Their physical and chemical properties are dependent upon their size, structure and compositions. Understanding the thermodynamics, kinetics and growth mechanisms will provide building blocks for developing more controllable and reproducible synthesis. In this dissertation, some of the aspects have been investigated and a few thermodynamic/growth models were suggested.

In Chapter 4, the Pt/Pd alloy nanoparticles were synthesized via colloidal methods, and the structure and elemental distribution were characterized via TEM, STEM and EDX. A smooth composition gradient within Pt/Pd alloy nanoparticle with Pt enrichment at the corners were observed experimentally. The smooth composition gradient was the result of reaction kinetics of both reduction of precursors and growth of nanoparticles, and it was explained by a growth model. The Pt corner enrichment was a result of local thermodynamic control at the corners, which was related to the local chemical potential at the corners, and it was equal to the chemical potential of the external solution at equilibrium. The mixed control of kinetics and thermodynamics in bimetallic nanoparticle synthesis could lead to the formation of particles with complex composition profiles. Additionally, the local thermodynamic control at the corners also resulted in rounded corners in nanoparticles. The Au MTPs, including Dh, Ic and truncated bi-tetrahedra, were synthesized via colloidal methods. The rounded corners were observed in these particles,

which appeared to violate the conditions for both thermodynamic and kinetic Wulff construction. The radius of curvature at the corners was measured on a few hundred particles and they were determined to be size-independent. This size-independent corner rounding phenomenon was explained by an analytic model. The rounded or even in some cases truncated corners were a Lyapunov steady-state solution while growth, and the rounding could be exploited to measure the chemical potential under different growth conditions.

In Chapter 5, the thermodynamic stability of asymmetric Dh particles was analyzed. The asymmetric Pt/Pd nanoparticles with mirror symmetry, instead of 5-fold symmetry, were synthesized under different reaction conditions. The resulting shapes were fit with a full Dh with some level of  $\{111\}$  re-entrance at each corner. The total re-entrant levels of 359 Dh particles synthesized using different amount of PVP were measured and the total re-entrant centered around 1.7. FEA calculations have been performed to determine the bulk strain energy. The total energy of the particles was the sum of bulk strain energy and surface energy, including both strain-free surface free energy and surface stress energy. The appearance of the asymmetric particles was found to be a local minimum of the free energy landscape. At very small sizes, 5-fold Dh appeared to have the lowest energy, and as size increases, the asymmetric particle with a mirror symmetry started to become the thermodynamically stable structure.

The strain-induced segregation in bimetallic MTPs was analyzed by an analytic first-order expansion within a continuum model, in Chapter 6. Segregation changes both the local strain energy and the configurational entropy in a binary system, by assuming it to be an ideal binary solid solution, where the change in free energy is the sum of these two terms. If a regular solution system is considered, the contribution from enthalpy of mixing will be included and the equation

in the model has to be solved numerically. Since constant local strain is assumed to be only valid for systems with two elements that have a small lattice mismatch. In this chapter, the Au/Ag system was used as a model system for demonstration purposes. For systems with larger lattice mismatch, the change in strain energy will be large, and the strain-induced segregation will be more pronounced. While the change in free energy is small, there is still a noticeable segregation of larger atoms to the outer most surface and smaller ones to the core. The results also indicate that the strain-induced segregation is temperature-dependent. At lower temperature, the segregation is more significant.

In chapter 7 of this dissertation, a method called super resolution plasmon microscopy (SRPM) was utilized to monitor the nanoparticle diffusion and growth *in situ* in solution. The time resolved single particle study was performed on photo-mediated synthesized Ag triangular platelets. The results indicated that there was a blue shift possibly due to the corner rounding as the reaction goes on. The single Ag nanoprism growth study will be performed on a particle at the much earlier stage of growth. An ultra-thin liquid cell was designed for confining the particles to move in 2D. It prevented the loss of tracking during the measurements. The single particle measurements were performed on 90nm Au nanospheres and photomediated synthesized Ag nanoprisms, respectively. The *in situ* Au nanorods synthesis was also carried out in this ultra-thin liquid cell. The CTAB precipitation problem needs to be solved and the concentration of seed and growth solution needs to be lowered so that the tracking of the particles would become possible. At the end of this chapter, future work was suggested.

## 8.2 Future Work

As mentioned in Chapter 2, there are mixed thermodynamic and kinetic control of nanoparticle growth. The thermodynamic and kinetic Wulff constructions correspond to the limits of very fast and very slow exchange of atoms between different surfaces respectively. The mixed growth can be achieved when the rate of atom exchange is in between the two limits.

These shapes are a mixture of the two classes of Wulff constructions. One possible example of this is shown in Figure 2.9. Pd nanoparticles were synthesized using citrate acid as a reducing agent, and PVP as surfactants. A transition from sharp decahedral bipyramids (kinetic shape) at higher concentrations of PVP to ones with re-entrant surfaces (thermodynamic shape) at lower PVP concentrations was observed. The shape transition is shown in Figure 8.1.

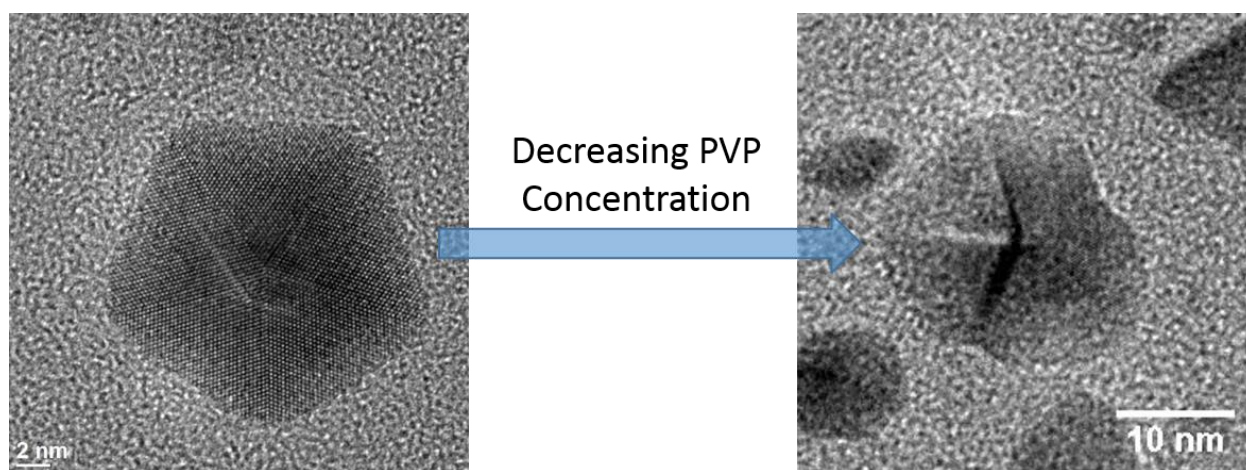


Figure 8.1 Pd Dh particles does not have  $\{111\}$  re-entrant facets

To what extent this is a general phenomenon is unclear. It is often hard to understand the relative role of kinetics and thermodynamics and couple them to nanoparticle synthesis parameters and reported experimental data – it can be fallen into one of the future directions.

In this dissertation, the segregation in colloidal synthesized bimetallic nanoparticles have been studied. In Chapter 4 and 6, I investigated how thermodynamics, kinetics and strain affect the elemental distribution in the bimetallic nanoparticles. These models are developed based on free-standing particles. The segregation in supported bimetallic nanoparticles could also be studied. The presence of a substrate influences the structure and elemental distribution of supported bimetallic nanoparticles. [200, 201] Negreiros *et al.* [201] has performed EP-DFT calculation showing that the interface between AgPd nanoparticles and MgO (100) substrate was Pd-enriched while the surface of the particles was Ag-enriched. The Pd enrichment at the interface was attributed to the stronger Pd-O bond, compared with the Ag-O bond. In addition, the Ag concentration at the interface increases with the nanoparticle size. This is because the lattice mismatch between Pd and the substrate is greater than that of Ag. Therefore, Ag will help release the stress at the interface. A number of factors such as surface energy, strain, growth kinetics will determine the final nanoparticle morphology and affect the catalytic performance when these systems are used in catalytic applications. Experimental studies could be performed to explore this new area. ALD would be an ideal synthesis method to produce such supported bimetallic nanoparticles on different metal oxide nanoparticle surfaces. In Marks group, the surface of SrTiO<sub>3</sub> (100) and (110), synthesized under different conditions, were studied using aberration-corrected HREM and they appeared to have different surface structures. [202, 203] Exploring how surface structures affect the bimetallic nanoparticle structure and segregation would be possible via aberration-corrected STEMs. This is definitely an interesting new avenue for research.

Nanoparticle catalysis has been an active research area for decades, and it still has great potential. Single atom catalysis has drawn a great amount of attention in recent years. [204-206]

Single atom catalysis provides insight on the identification and characterization of catalytic active sites, which will be crucial for the understanding of catalytic reaction mechanism at the atomic level. [206] In collaboration with Notestein group at Northwestern, we reported uniform distribution of Ta single atoms on anatase  $\text{TiO}_2$  (001) nanosheets, and found that Ta atoms sits on top of the Ti-O columns on the surface. According to XPS spectra, the Ta 4f peaks around 26.3eV and 28.3eV confirmed that Ta atoms are at 5+ state. Combining electron microscopy and other spectroscopy techniques, the possible single atom sites could be determined, which is essential for understanding the catalytic reaction mechanisms. We also found that Ta single atoms were much more stable on  $\text{TiO}_2$ , compared with Ta/ $\text{SiO}_2$  system. After electron beam irradiation, both anatase  $\text{TiO}_2$  and  $\text{SiO}_2$  nanosphere substrates were damaged and underwent shape change. However, Ta on  $\text{TiO}_2$  remained in single atom form, where Ta on  $\text{SiO}_2$  agglomerated and formed clusters. The HAADF images of Ta/ $\text{TiO}_2$  and Ta/ $\text{SiO}_2$ , before and after electron beam irradiation, are shown in Figure 8.2.

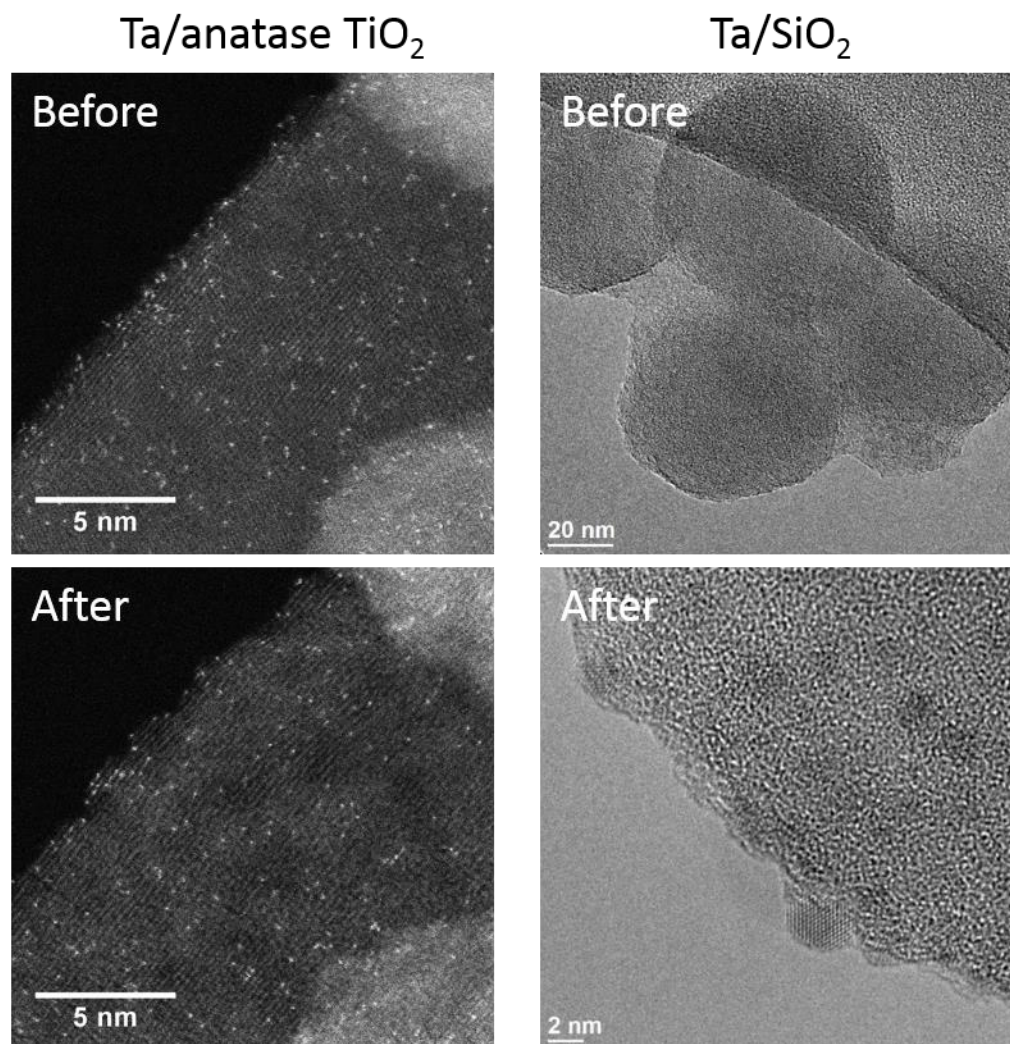


Figure 8.2 HADDF/TEM images of Ta/TiO<sub>2</sub> and Ta/SiO<sub>2</sub>, before and after electron beam irradiation

The stability of the single atoms will largely affect the catalytic performance, and understanding the interactions between the metal atoms and supports are very important. The successful and effective characterization of the single atom catalytic systems will provide insights to understand the catalytic mechanisms.

Many other room temperature syntheses could be monitored by the super-resolution plasmon microscopy (SRPM), and it can be used in various other applications, such as biosensing.

The resolution could be improved by using a brighter light source and the 3D tracking could be possible. Further development of this set-up can enable monitoring the particle growth at elevated temperatures.

## Reference

1. Henry, A.I., et al., *Correlated Structure and Optical Property Studies of Plasmonic Nanoparticles*. J. Phys. Chem. C, 2011. **115**(19): p. 9291-9305.
2. Talapin, D.V., et al., *Prospects of colloidal nanocrystals for electronic and optoelectronic applications*. Chem. Rev., 2010. **110**(1): p. 389-458.
3. Burda, C., et al., *Chemistry and properties of nanocrystals of different shapes*. Chem. Rev., 2005. **105**(4): p. 1025-102.
4. Wiley, B., Y. Sun, and Y. Xia, *Synthesis of silver nanostructures with controlled shapes and properties*. Acc. Chem. Res., 2007. **40**(10): p. 1067-76.
5. Cuenya, B.R., *Synthesis and catalytic properties of metal nanoparticles: Size, shape, support, composition, and oxidation state effects*. Thin Solid Films, 2010. **518**(12): p. 3127-3150.
6. Wulff, G., *Zur Frage der Geschwindigkeit des Wachstums und der Auflösung der Krystallflächen*. . Z. Kristallogr. Mineral. , 1901. **34**: p. 449-530.
7. von Laue, M., *Der Wulffsche satz fur die gleichgewichtsform von kristallen*. Z. Kristallogr., 1943. **105**: p. 124-133.
8. Winterbottom, W.L., *Equilibrium Shape of a Small Particle in Contact with a Foreign Substrate*. Acta Metall., 1967. **15**(2): p. 303-310.
9. Herring, C., *Some Theorems on the Free Energies of Crystal Surfaces*. Phys. Rev., 1951. **82**(1): p. 87-93.
10. Dinghas, A., *Uber einen geometrischen sat von Wulff fur die gleichgewichtsform von kristallen*. Z. Kristallogr., 1944. **105**: p. 304-314.
11. Marks, L.D., *Modified Wulff Constructions for Twinned Particles*. J. Cryst. Growth, 1983. **61**(3): p. 556-566.
12. Marks, L.D. and A. Howie, *Multiply-Twinned Particles in Silver Catalysts*. Nature, 1979. **282**(5735): p. 196-198.
13. Yagi, K., et al., *In-situ observations of growth processes of multiply twinned particles*. Journal of Crystal Growth, 1975. **28**(1): p. 117-124.
14. Ino, S., *Stability of Multiply-Twinned Particles*. Journal of the Physical Society of Japan, 1969. **27**(4): p. 941-953.

15. Tsutomu, K., *Study on the Structure of Evaporated Gold Particles by Means of a High Resolution Electron Microscope*. Japanese Journal of Applied Physics, 1968. **7**(1): p. 27.
16. Allpress, J.G. and J.V. Sanders, *The structure and orientation of crystals in deposits of metals on mica*. Surface Science, 1967. **7**(1): p. 1-25.
17. Ino, S. and S. Ogawa, *Multiply Twinned Particles at Earlier Stages of Gold Film Formation on Alkali Halide Crystals*. Journal of the Physical Society of Japan, 1967. **22**(6): p. 1365-1374.
18. Ino, S., *Epitaxial Growth of Metals on Rocksalt Faces Cleaved in Vacuum. II. Orientation and Structure of Gold Particles Formed in Ultrahigh Vacuum*. Journal of the Physical Society of Japan, 1966. **21**(2): p. 346-362.
19. Dundurs, J., L.D. Marks, and P.M. Ajayan, *Structural fluctuations in small particles*. Philosophical Magazine A, 1988. **57**(4): p. 605-620.
20. Ajayan, P.M. and L.D. Marks, *Quasimelting and phases of small particles*. Physical Review Letters, 1988. **60**(7): p. 585-587.
21. Kirkland, A.I., et al., *Chapter 8. The structure, characterization, and evolution of colloidal metals*. Annual Reports Section "C" (Physical Chemistry), 1990. **87**(0): p. 247-304.
22. Ajayan, P.M. and L.D. Marks, *Experimental evidence for quasimelting in small particles*. Physical Review Letters, 1989. **63**(3): p. 279-282.
23. Marks, L.D. and D.J. Smith, *High resolution studies of small particles of gold and silver*. Journal of Crystal Growth, 1981. **54**(3): p. 425-432.
24. Smith, D.J. and L.D. Marks, *High resolution studies of small particles of gold and silver*. Journal of Crystal Growth, 1981. **54**(3): p. 433-438.
25. Marks, L.D. and D.J. Smith, *Direct surface imaging in small metal particles*. Nature, 1983. **303**(5915): p. 316-317.
26. Lin, Y., et al., *Adhesion and Atomic Structures of Gold on Ceria Nanostructures: The Role of Surface Structure and Oxidation State of Ceria Supports*. Nano Letters, 2015. **15**(8): p. 5375-5381.
27. Park, N.-G., *Perovskite solar cells: an emerging photovoltaic technology*. Materials Today, 2015. **18**(2): p. 65-72.
28. Kneipp, K., et al., *Single Molecule Detection Using Surface-Enhanced Raman Scattering (SERS)*. Physical Review Letters, 1997. **78**(9): p. 1667-1670.

29. De Jong, W.H. and P.J.A. Borm, *Drug delivery and nanoparticles: Applications and hazards*. International Journal of Nanomedicine, 2008. **3**(2): p. 133-149.
30. Marks, L.D. and L. Peng, *Nanoparticle shape, thermodynamics and kinetics*. Journal of Physics: Condensed Matter, 2016. **28**(5): p. 053001.
31. Henry, A.-I., et al., *Correlated Structure and Optical Property Studies of Plasmonic Nanoparticles*. The Journal of Physical Chemistry C, 2011. **115**(19): p. 9291-9305.
32. Emilie, R., et al., *Correlating the structure and localized surface plasmon resonance of single silver right bipyramids*. Nanotechnology, 2012. **23**(44): p. 444005.
33. Ringe, E., et al., *Unraveling the Effects of Size, Composition, and Substrate on the Localized Surface Plasmon Resonance Frequencies of Gold and Silver Nanocubes: A Systematic Single-Particle Approach*. The Journal of Physical Chemistry C, 2010. **114**(29): p. 12511-12516.
34. Xia, Y., et al., *Shape-Controlled Synthesis of Metal Nanocrystals: Simple Chemistry Meets Complex Physics?* Angewandte Chemie International Edition, 2009. **48**(1): p. 60-103.
35. Motl, N.E., et al., *Au–Cu Alloy Nanoparticles with Tunable Compositions and Plasmonic Properties: Experimental Determination of Composition and Correlation with Theory*. J. Phys. Chem. C, 2010. **114**(45): p. 19263-19269.
36. Wilcoxon, J., *Optical Absorption Properties of Dispersed Gold and Silver Alloy Nanoparticles†*. The Journal of Physical Chemistry B, 2008. **113**(9): p. 2647-2656.
37. Murphy, C.J., et al., *Anisotropic Metal Nanoparticles: Synthesis, Assembly, and Optical Applications*. The Journal of Physical Chemistry B, 2005. **109**(29): p. 13857-13870.
38. Sankar, M., et al., *Designing bimetallic catalysts for a green and sustainable future*. Chem. Soc. Rev., 2012. **41**(24): p. 8099-139.
39. Bracey, C.L., P.R. Ellis, and G.J. Hutchings, *Application of copper-gold alloys in catalysis: current status and future perspectives*. Chemical Society Reviews, 2009. **38**(8): p. 2231-2243.
40. Sinfelt, J.H., *Catalysis by Alloys and Bimetallic Clusters*. Acc. Chem. Res., 1977. **10**(1): p. 15-20.
41. Singh, A.K. and Q. Xu, *Synergistic Catalysis over Bimetallic Alloy Nanoparticles*. Chem. Cat. Chem., 2013. **5**(3): p. 652-676.
42. Liu, X.W., D.S. Wang, and Y.D. Li, *Synthesis and catalytic properties of bimetallic nanomaterials with various architectures*. Nano Today, 2012. **7**(5): p. 448-466.

43. Wang, C., et al., *Correlation Between Surface Chemistry and Electrocatalytic Properties of Monodisperse Pt<sub>x</sub>Ni<sub>1-x</sub> Nanoparticles*. *Adv. Funct. Mater.*, 2011. **21**(1): p. 147-152.
44. Stamenkovic, V.R., et al., *Effect of Surface Composition on Electronic Structure, Stability, and Electrocatalytic Properties of Pt-Transition Metal Alloys: Pt-Skin versus Pt-Skeleton Surfaces*. *Journal of the American Chemical Society*, 2006. **128**(27): p. 8813-8819.
45. Suntivich, J., et al., *Surface Composition Tuning of Au–Pt Bimetallic Nanoparticles for Enhanced Carbon Monoxide and Methanol Electro-oxidation*. *Journal of the American Chemical Society*, 2013. **135**(21): p. 7985-7991.
46. Tan, L.F., et al., *Confining alloy or core-shell Au-Pd bimetallic nanocrystals in silica nanorattles for enhanced catalytic performance*. *J. Mater. Chem. A*, 2013. **1**(35): p. 10382-10388.
47. Cui, C., et al., *Octahedral PtNi Nanoparticle Catalysts: Exceptional Oxygen Reduction Activity by Tuning the Alloy Particle Surface Composition*. *Nano Letters*, 2012. **12**(11): p. 5885-5889.
48. Ma, J., et al., *Correlation between surface chemical composition with catalytic activity and selectivity of organic-solvent synthesized Pt-Ti nanoparticles*. *Journal of Materials Chemistry A*, 2013. **1**(31): p. 8798-8804.
49. Narayanan, R. and M.A. El-Sayed, *Shape-Dependent Catalytic Activity of Platinum Nanoparticles in Colloidal Solution*. *Nano Letters*, 2004. **4**(7): p. 1343-1348.
50. Tian, N., et al., *Synthesis of Tetrahedral Platinum Nanocrystals with High-Index Facets and High Electro-Oxidation Activity*. *Science*, 2007. **316**(5825): p. 732-735.
51. Bratlie, K.M., et al., *Platinum nanoparticle shape effects on benzene hydrogenation selectivity*. *Nano Lett.*, 2007. **7**(10): p. 3097-101.
52. Cleveland, C.L. and U. Landman, *The energetics and structure of nickel clusters: Size dependence*. *The Journal of Chemical Physics*, 1991. **94**(11): p. 7376-7396.
53. Hamilton, J.C., *Edge energies: Atomistic calculations of a continuum quantity*. *Phys. Rev. B*, 2006. **73**(12): p. 125447.
54. Ringe, E., R.P. Van Duyne, and L.D. Marks, *Kinetic and Thermodynamic Modified Wulff Constructions for Twinned Nanoparticles*. *The Journal of Physical Chemistry C*, 2013. **117**(31): p. 15859-15870.
55. Dinghas, A., *On Wulff's geometric theorem for the balanced form of crystals*. *Z. Kristallogr.*, 1944. **105**(4): p. 304-314.

56. Winterbottom, W.L., *Equilibrium Shape of a Small Particle in Contact with a Foreign Substrate*. Acta Metall. Mater., 1967. **15**(2): p. 303-310.
57. Peng, L., et al., *Segregation in bimetallic nanoparticles*. Physical Chemistry Chemical Physics, 2015. **17**(42): p. 27940-27951.
58. Zia, R.K.P., J.E. Avron, and J.E. Taylor, *The Summertop Construction - Crystals in a Corner*. J. Stat. Phys., 1988. **50**(3-4): p. 727-736.
59. Marks, L.D., *Surface structure and energetics of multiply twinned particles*. Philosophical Magazine A, 1984. **49**(1): p. 81-93.
60. Hamilton, D.R. and R.G. Seidensticker, *Propagation Mechanism of Germanium Dendrites*. Journal of Applied Physics, 1960. **31**(7): p. 1165-1168.
61. van de Waal, B.W., *Cross-twinning model of fcc crystal growth*. Journal of Crystal Growth, 1996. **158**(1): p. 153-165.
62. Berg, W.F., *Crystal growth from solutions*. Proceedings of the Royal Society of London Series a-Mathematical and Physical Sciences, 1938. **164**(A916): p. 0079-0095.
63. Røyne, A. and D.K. Dysthe, *Rim formation on crystal faces growing in confinement*. Journal of Crystal Growth, 2012. **346**(1): p. 89-100.
64. Alpay, D., L. Peng, and L.D. Marks, *Are Nanoparticle Corners Round?* The Journal of Physical Chemistry C, 2015. **119**(36): p. 21018-21023.
65. Bagley, B.G., *A Dense Packing of Hard Spheres with Five-fold Symmetry*. Nature, 1965. **208**(5011): p. 674-675.
66. Yang, C.Y., *Crystallography of decahedral and icosahedral particles: I. Geometry of twinning*. Journal of Crystal Growth, 1979. **47**(2): p. 274-282.
67. Volterra, V., Ann. Scient. Ec. Norm. Sup., 1907. **24**: p. 401.
68. Marks, L.D., *Surface-Structure and Energetics of Multiply Twinned Particles*. Philosophical Magazine A-Physics of Condensed Matter Structure Defects and Mechanical Properties, 1984. **49**(1): p. 81-93.
69. Patala, S., L.D. Marks, and M.O. de la Cruz, *Elastic Strain Energy Effects in Faceted Decahedral Nanoparticles*. Journal of Physical Chemistry C, 2013. **117**(3): p. 1485-1494.
70. Zhou, Y. and K.A. Fichthorn, *Internal Stress-Induced Orthorhombic Phase in 5-Fold-Twinned Noble Metal Nanowires*. The Journal of Physical Chemistry C, 2014. **118**(32): p. 18746-18755.

71. Marks, L.D., *Experimental studies of small particle structures*. Reports on Progress in Physics, 1994. **57**(6): p. 603.
72. Sumio, I., *Fine Particles of Silicon. II. Decahedral Multiply-Twinned Particles*. Japanese Journal of Applied Physics, 1987. **26**(3R): p. 365.
73. Goris, B., et al., *Measuring Lattice Strain in Three Dimensions through Electron Microscopy*. Nano Letters, 2015. **15**(10): p. 6996-7001.
74. Hofmeister, H., *Lattice defects in decahedral multiply twinned particles of palladium*. Zeitschrift für Physik D Atoms, Molecules and Clusters, 1991. **19**(4): p. 307-310.
75. Marks, L.D. and D.J. Smith, *HREM and STEM of defects in multiply-twinned particles*. Journal of Microscopy, 1983. **130**(2): p. 249-261.
76. Peng, L., R.P. Van Duyne, and L.D. Marks, *Strain-Induced Segregation in Bimetallic Multiply Twinned Particles*. The Journal of Physical Chemistry Letters, 2015. **6**(10): p. 1930-1934.
77. Riccardo, F., *Symmetry breaking and morphological instabilities in core-shell metallic nanoparticles*. Journal of Physics: Condensed Matter, 2015. **27**(1): p. 013003.
78. Bochicchio, D. and R. Ferrando, *Morphological instability of core-shell metallic nanoparticles*. Physical Review B, 2013. **87**(16): p. 165435.
79. Gryaznov, V.G., et al., *Pentagonal Symmetry and Disclinations in Small Particles*. Crystal Research and Technology, 1999. **34**(9): p. 1091-1119.
80. Gryaznov, V.G., et al., *Channels of Relaxation of Elastic Stresses in Pentagonal Nanoparticles*. physica status solidi (b), 1991. **167**(2): p. 441-450.
81. Polonsky, I.A., et al., *Disclination in an elastic sphere*. Philosophical Magazine A, 1991. **64**(2): p. 281-287.
82. Romanov, A.E. and A.L. Kolesnikova, *Application of disclination concept to solid structures*. Progress in Materials Science, 2009. **54**(6): p. 740-769.
83. Romanov, A.E., et al., *Structural transformations in nano- and microobjects triggered by disclinations*. Journal of Materials Research, 2011. **27**(03): p. 545-551.
84. Dorogin, L.M., et al., *Crystal mismatched layers in pentagonal nanorods and nanoparticles*. physica status solidi (b), 2010. **247**(2): p. 288-298.
85. Lu, J., et al., *Toward atomically-precise synthesis of supported bimetallic nanoparticles using atomic layer deposition*. Nat. Commun., 2014. **5**: p. 3264.

86. Serpell, C.J., et al., *Core@shell bimetallic nanoparticle synthesis via anion coordination*. Nat Chem, 2011. **3**(6): p. 478-83.
87. Chen, H.Y., et al., *Graphene supported Au-Pd bimetallic nanoparticles with core-shell structures and superior peroxidase-like activities*. J. Mater. Chem., 2011. **21**(44): p. 17658-17661.
88. Li, Z.A., et al., *Chemically ordered decahedral FePt nanocrystals observed by electron microscopy*. Phys. Rev. B, 2014. **89**(16): p. 161406.
89. Stappert, S., et al., *Gas-phase preparation of L10 ordered FePt nanoparticles*. J. Cryst. Growth, 2003. **252**(1-3): p. 440-450.
90. Wang, D., et al., *Structurally ordered intermetallic platinum-cobalt core-shell nanoparticles with enhanced activity and stability as oxygen reduction electrocatalysts*. Nat Mater, 2013. **12**(1): p. 81-87.
91. Langlois, C., et al., *Transition from core-shell to Janus chemical configuration for bimetallic nanoparticles*. Nanoscale, 2012. **4**(11): p. 3381-3388.
92. Song, Y., K. Liu, and S. Chen, *AgAu Bimetallic Janus Nanoparticles and Their Electrocatalytic Activity for Oxygen Reduction in Alkaline Media*. Langmuir, 2012. **28**(49): p. 17143-17152.
93. Herzing, A.A., et al., *Energy dispersive X-ray spectroscopy of bimetallic nanoparticles in an aberration corrected scanning transmission electron microscope*. Faraday Discussions, 2008. **138**(0): p. 337-351.
94. Cui, C., et al., *Compositional segregation in shaped Pt alloy nanoparticles and their structural behaviour during electrocatalysis*. Nat Mater, 2013. **12**(8): p. 765-771.
95. Chen, S., P.J. Ferreira, and Y. Shao-Horn, *Surface Segregation in Pt<sub>3</sub>Co Nanoparticles Characterized by Scanning Transmission Electron Microscopy*. Microscopy and Microanalysis, 2007. **13**(Supplement S02): p. 604-605.
96. Ringe, E., R.P. Van Duyne, and L.D. Marks, *Wulff construction for alloy nanoparticles*. Nano Lett., 2011. **11**(8): p. 3399-403.
97. Kristyan, S. and J. Giber, *Temperature-Dependence of the Surface Free-Energies of Solid Chemical-Elements*. Surf. Sci., 1988. **201**(3): p. L532-L538.
98. Ferrando, R., J. Jellinek, and R.L. Johnston, *Nanoalloys: from theory to applications of alloy clusters and nanoparticles*. Chem. Rev., 2008. **108**(3): p. 845-910.
99. Heiles, S. and R.L. Johnston, *Global optimization of clusters using electronic structure methods*. Int. J. Quantum Chem., 2013. **113**(18): p. 2091-2109.

100. Ferrando, R., A. Fortunelli, and R.L. Johnston, *Searching for the optimum structures of alloy nanoclusters*. Phys. Chem. Chem. Phys., 2008. **10**(5): p. 640-9.
101. Daw, M.S. and M.I. Baskes, *Embedded-Atom Method - Derivation and Application to Impurities, Surfaces, and Other Defects in Metals*. Phys. Rev. B, 1984. **29**(12): p. 6443-6453.
102. Sutton, A.P. and J. Chen, *Long-range Finnis–Sinclair potentials*. Philos. Mag. Lett., 1990. **61**(3): p. 139-146.
103. Gupta, R.P., *Lattice-Relaxation at a Metal-Surface*. Phys. Rev. B, 1981. **23**(12): p. 6265-6270.
104. López, M.J. and J. Jellinek, *On the problem of fitting many-body potentials. I. The minimal maximum error scheme and the paradigm of metal systems*. J. Chem. Phys., 1999. **110**(18): p. 8899.
105. Rosato, V., M. Guillope, and B. Legrand, *Thermodynamical and structural properties of f.c.c. transition metals using a simple tight-binding model*. Philos. Mag. A, 1989. **59**(2): p. 321-336.
106. Cleri, F. and V. Rosato, *Tight-binding potentials for transition metals and alloys*. Phys. Rev. B, 1993. **48**(1): p. 22-33.
107. Johnston, R.L., *Evolving better nanoparticles: Genetic algorithms for optimising cluster geometries*. Dalton Trans., 2003(22): p. 4193-4207.
108. Ringe, E., et al., *Plasmon Length: A Universal Parameter to Describe Size Effects in Gold Nanoparticles*. Journal of Physical Chemistry Letters, 2012. **3**(11): p. 1479-1483.
109. Ferrando, R., J. Jellinek, and R.L. Johnston, *Nanoalloys: From Theory to Applications of Alloy Clusters and Nanoparticles*. Chemical Reviews, 2008. **108**(3): p. 845-910.
110. Guisbiers, G., G. Abudukelimu, and D. Hourlier, *Size-dependent catalytic and melting properties of platinum-palladium nanoparticles*. Nanoscale Research Letters, 2011. **6**(1): p. 1-5.
111. Narayanan, R. and M.A. El-Sayed, *Shape-dependent catalytic activity of platinum nanoparticles in colloidal solution*. Nano Lett., 2004. **4**(7): p. 1343-1348.
112. Stamenkovic, V.R., et al., *Effect of surface composition on electronic structure, stability, and electrocatalytic properties of Pt-transition metal alloys: Pt-skin versus Pt-skeleton surfaces*. J. Am. Chem. Soc., 2006. **128**(27): p. 8813-9.

113. Suntivich, J., et al., *Surface composition tuning of Au-Pt bimetallic nanoparticles for enhanced carbon monoxide and methanol electro-oxidation*. J. Am. Chem. Soc., 2013. **135**(21): p. 7985-91.
114. Lim, B., et al., *Twin-Induced Growth of Palladium–Platinum Alloy Nanocrystals*. Angewandte Chemie International Edition, 2009. **48**(34): p. 6304-6308.
115. Seo, D., et al., *Shape Adjustment between Multiply Twinned and Single-Crystalline Polyhedral Gold Nanocrystals: Decahedra, Icosahedra, and Truncated Tetrahedra*. The Journal of Physical Chemistry C, 2008. **112**(7): p. 2469-2475.
116. Seo, D., et al., *Shape adjustment between multiply twinned and single-crystalline polyhedral gold nanocrystals: decahedra, icosahedra, and truncated tetrahedra*. J. Phys. Chem. C, 2008. **112**(7): p. 2469-2475.
117. Liao, H., A. Fisher, and Z.J. Xu, *Surface Segregation in Bimetallic Nanoparticles: A Critical Issue in Electrocatalyst Engineering*. Small, 2015. **11**(27): p. 3221-3246.
118. Williams, F.L. and D. Nason, *Binary alloy surface compositions from bulk alloy thermodynamic data*. Surface Science, 1974. **45**(2): p. 377-408.
119. Williams, F.L. and D. Nason, *Binary alloy surface compositions from bulk alloy thermodynamic data*. Surface Science, 1974. **45**.
120. Quinto, D.T., V.S. Sundaram, and W.D. Robertson, *Auger spectra of copper-nickel alloys*. Surface Science, 1971. **28**(2): p. 504-516.
121. Tarng, M.L. and G.K. Wehner, *Alloy Sputtering Studies with in situ Auger Electron Spectroscopy*. Journal of Applied Physics, 1971. **42**(6): p. 2449-2452.
122. Anderson, J.H., P.J. Conn, and S.G. Brandenberger, *Hydrogen chemisorption and surface composition of silica-supported platinum-copper alloys*. Journal of Catalysis, 1970. **16**(3): p. 326-331.
123. Guisbiers, G., et al., *Electrum, the Gold–Silver Alloy, from the Bulk Scale to the Nanoscale: Synthesis, Properties, and Segregation Rules*. ACS Nano, 2016. **10**(1): p. 188-198.
124. Tao, F., et al., *Reaction-Driven Restructuring of Rh-Pd and Pt-Pd Core-Shell Nanoparticles*. Science, 2008. **322**(5903): p. 932-934.
125. van den Oetelaar, L.C.A., et al., *Surface Segregation in Supported Pd–Pt Nanoclusters and Alloys*. The Journal of Physical Chemistry B, 1998. **102**(18): p. 3445-3455.
126. Li, T., et al., *Atomic engineering of platinum alloy surfaces*. Ultramicroscopy, 2013. **132**: p. 205-211.

127. Lloyd, L.D., et al., *Theoretical investigation of isomer stability in platinum-palladium nanoalloy clusters*. Journal of Materials Chemistry, 2004. **14**(11): p. 1691-1704.
128. Zhiyao, D. and W. Guofeng, *Monte Carlo simulation of surface segregation phenomena in extended and nanoparticle surfaces of Pt-Pd alloys*. Journal of Physics: Condensed Matter, 2011. **23**(47): p. 475301.
129. Fan, H.J., U. Gösele, and M. Zacharias, *Formation of Nanotubes and Hollow Nanoparticles Based on Kirkendall and Diffusion Processes: A Review*. Small, 2007. **3**(10): p. 1660-1671.
130. Lewis, E.A., et al., *Real-time imaging and elemental mapping of AgAu nanoparticle transformations*. Nanoscale, 2014. **6**(22): p. 13598-13605.
131. Crosby, L., et al., *Wulff shape of strontium titanate nanocuboids*. Surface Science, 2015. **632**: p. L22-L25.
132. Ahrenstorf, K., et al., *Nucleation and Growth Mechanism of NixPt1-x Nanoparticles*. Advanced Functional Materials, 2008. **18**(23): p. 3850-3856.
133. Choi, S.-I., et al., *Synthesis and Characterization of 9 nm Pt-Ni Octahedra with a Record High Activity of 3.3 A/mgPt for the Oxygen Reduction Reaction*. Nano Letters, 2013. **13**(7): p. 3420-3425.
134. Marks, L. and L. Peng, *Nanoparticle shape, thermodynamics and kinetics*. Journal of Physics: Condensed Matter, 2016. **28**(5): p. 053001.
135. McMahon, J.A., et al., *Correlating the Structure, Optical Spectra, and Electrodynamics of Single Silver Nanocubes*. J. Phys. Chem. C, 2009. **113**(7): p. 2731-2735.
136. Taylor, J.E., *Mean-Curvature And Weighted Mean-Curvature .2*. Acta Metall. Mater., 1992. **40**(7): p. 1475-1485.
137. Blaha, P., et al., *WIEN2k, An Augmented Plane Wave Plus Local Orbitals Program for Calculating Crystal Properties*. 2001, Vienna: Technical University of Vienna.
138. Wu, Z. and R.E. Cohen, *More accurate generalized gradient approximation for solids*. Phys. Rev. B, 2006. **73**(23): p. 235116-6.
139. Howie, A. and L.D. Marks, *Elastic Strains and the Energy-Balance for Multiply Twinned Particles*. Philos. Mag. A, 1984. **49**(1): p. 95-109.
140. Gamalski, A.D., et al., *Twin plane re-entrant mechanism for catalytic nanowire growth*. Nano Lett., 2014. **14**(3): p. 1288-92.

141. Allpress, J.G. and J.V. Sanders, *Structure And Orientation Of Crystals In Deposits Of Metals On Mica*. Surface Science, 1967. **7**(1): p. 1-25.
142. Choi, S.I., et al., *Controlling the Size and Composition of Nanosized Pt–Ni Octahedra to Optimize Their Catalytic Activities toward the Oxygen Reduction Reaction*. ChemSusChem, 2014. **7**(5): p. 1476-1483.
143. Mi, J.-L., et al., *The formation mechanism of bimetallic PtRu alloy nanoparticles in solvothermal synthesis*. Nanoscale, 2015. **7**(39): p. 16170-16174.
144. Yin, Z., et al., *Monodispersed bimetallic PdAg nanoparticles with twinned structures: Formation and enhancement for the methanol oxidation*. Scientific Reports, 2014. **4**: p. 4288.
145. Talapin, D.V., et al., *Prospects of Colloidal Nanocrystals for Electronic and Optoelectronic Applications*. Chemical Reviews, 2010. **110**(1): p. 389-458.
146. Wiley, B., Y. Sun, and Y. Xia, *Polyol Synthesis of Silver Nanostructures: Control of Product Morphology with Fe(II) or Fe(III) Species*. Langmuir, 2005. **21**(18): p. 8077-8080.
147. Xia, Y., et al., *Shape-Controlled Synthesis of Metal Nanocrystals: Simple Chemistry Meets Complex Physics?* Angewandte Chemie (International ed. in English), 2009. **48**(1): p. 60-103.
148. Marks, L.D., *Modified Wulff Constructions for Twinned Particles*. Journal of Crystal Growth, 1983. **61**(3): p. 556-566.
149. Lim, B., Y. Xiong, and Y. Xia, *A Water-Based Synthesis of Octahedral, Decahedral, and Icosahedral Pd Nanocrystals*. Angewandte Chemie International Edition, 2007. **46**(48): p. 9279-9282.
150. Patala, S., L.D. Marks, and M. Olvera de la Cruz, *Elastic Strain Energy Effects in Faceted Decahedral Nanoparticles*. The Journal of Physical Chemistry C, 2013. **117**(3): p. 1485-1494.
151. Wilcoxon, J., *Optical Absorption Properties of Dispersed Gold and Silver Alloy Nanoparticles*. The Journal of Physical Chemistry B, 2009. **113**(9): p. 2647-2656.
152. Motl, N.E., et al., *Au–Cu Alloy Nanoparticles with Tunable Compositions and Plasmonic Properties: Experimental Determination of Composition and Correlation with Theory*. The Journal of Physical Chemistry C, 2010. **114**(45): p. 19263-19269.
153. Link, S., Z.L. Wang, and M.A. El-Sayed, *Alloy Formation of Gold–Silver Nanoparticles and the Dependence of the Plasmon Absorption on Their Composition*. The Journal of Physical Chemistry B, 1999. **103**(18): p. 3529-3533.

154. Drube, W., et al., *Sublifetime-resolution Ag  $L_{3}$ -edge XANES studies of Ag-Au alloys*. Physical Review B, 1998. **58**(11): p. 6871-6876.
155. Wang, C., et al., *One-Pot Synthesis of Oleylamine Coated AuAg Alloy NPs and Their Catalysis for CO Oxidation*. Chemistry of Materials, 2009. **21**(3): p. 433-435.
156. Wilcoxon, J., *Optical absorption properties of dispersed gold and silver alloy nanoparticles*. J. Phys. Chem. B, 2009. **113**(9): p. 2647-56.
157. Sankar, M., et al., *Designing bimetallic catalysts for a green and sustainable future*. Chemical Society Reviews, 2012. **41**(24): p. 8099-8139.
158. Sinfelt, J.H., *Catalysis by alloys and bimetallic clusters*. Accounts of Chemical Research, 1977. **10**(1): p. 15-20.
159. Singh, A.K. and Q. Xu, *Synergistic Catalysis over Bimetallic Alloy Nanoparticles*. ChemCatChem, 2013. **5**(3): p. 652-676.
160. Scheidt, W.R., *Trends in metalloporphyrin stereochemistry*. Accounts of Chemical Research, 1977. **10**(9): p. 339-345.
161. Lu, J., et al., *Toward atomically-precise synthesis of supported bimetallic nanoparticles using atomic layer deposition*. Nat Commun, 2014. **5**: p. 3264.
162. Peng, L., R.P. Van Duyne, and L.D. Marks, *Compositional Inhomogeneity and Corner Enrichment of Pt in Pt/Pd Bimetallic Nanoparticles*. The Journal of Physical Chemistry C, 2016.
163. Baskes, M.I., *Modified embedded-atom potentials for cubic materials and impurities*. Physical Review B, 1992. **46**(5): p. 2727-2742.
164. Cleri, F. and V. Rosato, *Tight-binding potentials for transition metals and alloys*. Physical Review B, 1993. **48**(1): p. 22-33.
165. Rosato, V., M. Guillope, and B. Legrand, *Thermodynamical and structural properties of f.c.c. transition metals using a simple tight-binding model*. Philosophical Magazine A, 1989. **59**(2): p. 321-336.
166. Daw, M.S. and M.I. Baskes, *Embedded-atom method: Derivation and application to impurities, surfaces, and other defects in metals*. Physical Review B, 1984. **29**(12): p. 6443-6453.
167. Deng, L., et al., *Au-Ag Bimetallic Nanoparticles: Surface Segregation and Atomic-Scale Structure*. The Journal of Physical Chemistry C, 2011. **115**(23): p. 11355-11363.

168. Shan, B., et al., *First-principles-based embedded atom method for PdAu nanoparticles*. Physical Review B, 2009. **80**(3).
169. Duan, Z. and G. Wang, *Monte Carlo simulation of surface segregation phenomena in extended and nanoparticle surfaces of Pt-Pd alloys*. J Phys Condens Matter, 2011. **23**(47): p. 475301.
170. Deng, L., et al., *Surface Segregation and Structural Features of Bimetallic Au–Pt Nanoparticles*. The Journal of Physical Chemistry C, 2010. **114**(25): p. 11026-11032.
171. Yuge, K., *Segregation of Pt(28)Rh(27) bimetallic nanoparticles: a first-principles study*. J Phys Condens Matter, 2010. **22**(24): p. 245401.
172. Ringe, E., R.P. Van Duyne, and L.D. Marks, *Wulff Construction for Alloy Nanoparticles*. Nano Letters, 2011. **11**(8): p. 3399-3403.
173. Howie, A. and L.D. Marks, *Elastic strains and the energy balance for multiply twinned particles*. Philosophical Magazine A, 1984. **49**(1): p. 95-109.
174. Cottrell, A.H. and B.A. Bilby, *Dislocation Theory of Yielding and Strain Ageing of Iron*. Proceedings of the Physical Society. Section A, 1949. **62**(1): p. 49.
175. Patala, S., L.D. Marks, and M. Olvera de la Cruz, *Thermodynamic Analysis of Multiply Twinned Particles: Surface Stress Effects*. The Journal of Physical Chemistry Letters, 2013. **4**(18): p. 3089-3094.
176. Radwan, F.A. *Some Properties of Copper–Gold and Silver–Gold Alloys at Different% of Gold*. in *Proceedings of the International MultiConference of Engineers and Computer Scientists*. 2011.
177. Sasaki, K., et al., *Highly stable Pt monolayer on PdAu nanoparticle electrocatalysts for the oxygen reduction reaction*. Nat Commun, 2012. **3**: p. 1115.
178. Pasini, T., et al., *Selective oxidation of 5-hydroxymethyl-2-furfural using supported gold-copper nanoparticles*. Green Chemistry, 2011. **13**(8): p. 2091-2099.
179. Yin, A.-X., et al., *Multiply twinned Pt-Pd nanicosahedrons as highly active electrocatalysts for methanol oxidation*. Chemical Communications, 2012. **48**(4): p. 543-545.
180. Pohl, D., et al., *Near-Surface Strain in Icosahedra of Binary Metallic Alloys: Segregational versus Intrinsic Effects*. Nano Letters, 2014. **14**(4): p. 1776-1784.
181. Wang, R., et al., *Layer Resolved Structural Relaxation at the Surface of Magnetic FePt Icosahedral Nanoparticles*. Physical Review Letters, 2008. **100**(1).

182. Delalande, M., et al., *L10 Ordering of Ultrasmall FePt Nanoparticles Revealed by TEM In Situ Annealing*. The Journal of Physical Chemistry C, 2012. **116**(12): p. 6866-6872.
183. Gruner, M.E., et al., *Multiply Twinned Morphologies of FePt and CoPt Nanoparticles*. Physical Review Letters, 2008. **100**(8): p. 087203.
184. Yang, B., et al., *Equilibrium Monte Carlo simulations of A1-L10 ordering in FePt nanoparticles*. Scripta Materialia, 2005. **53**(4): p. 417-422.
185. Müller, M. and K. Albe, *Lattice Monte Carlo simulations of FePt nanoparticles: Influence of size, composition, and surface segregation on order-disorder phenomena*. Physical Review B, 2005. **72**(9): p. 094203.
186. Laasonen, K., et al., *Competition between Icosahedral Motifs in AgCu, AgNi, and AgCo Nanoalloys: A Combined Atomistic-DFT Study*. The Journal of Physical Chemistry C, 2013. **117**(49): p. 26405-26413.
187. Woehl, T.J., et al., *Direct Observation of Aggregative Nanoparticle Growth: Kinetic Modeling of the Size Distribution and Growth Rate*. Nano Letters, 2014. **14**(1): p. 373-378.
188. Grogan, J.M., L. Rotkina, and H.H. Bau, *In situ*. Physical Review E, 2011. **83**(6): p. 061405.
189. Evans, J.E., et al., *Controlled Growth of Nanoparticles from Solution with In Situ Liquid Transmission Electron Microscopy*. Nano Letters, 2011. **11**(7): p. 2809-2813.
190. Zheng, H., et al., *Observation of Single Colloidal Platinum Nanocrystal Growth Trajectories*. Science, 2009. **324**(5932): p. 1309-1312.
191. de Jonge, N. and F.M. Ross, *Electron microscopy of specimens in liquid*. Nat Nano, 2011. **6**(11): p. 695-704.
192. Sagle, L.B., et al., *Single Plasmonic Nanoparticle Tracking Studies of Solid Supported Bilayers with Ganglioside Lipids*. Journal of the American Chemical Society, 2012. **134**(38): p. 15832-15839.
193. Bingham, J.M., et al., *Localized Surface Plasmon Resonance Imaging: Simultaneous Single Nanoparticle Spectroscopy and Diffusional Dynamics*. The Journal of Physical Chemistry C, 2009. **113**(39): p. 16839-16842.
194. Xue, C., et al., *Mechanistic Study of Photomediated Triangular Silver Nanoprism Growth*. Journal of the American Chemical Society, 2008. **130**(26): p. 8337-8344.
195. Lok, C.-N., et al., *Silver nanoparticles: partial oxidation and antibacterial activities*. JBIC Journal of Biological Inorganic Chemistry, 2007. **12**(4): p. 527-534.

196. Henglein, A., *Colloidal Silver Nanoparticles: Photochemical Preparation and Interaction with O<sub>2</sub>, CCl<sub>4</sub>, and Some Metal Ions*. Chemistry of Materials, 1998. **10**(1): p. 444-450.
197. Han, Y., et al., *Effect of Oxidation on Surface-Enhanced Raman Scattering Activity of Silver Nanoparticles: A Quantitative Correlation*. Analytical Chemistry, 2011. **83**(15): p. 5873-5880.
198. Jana, N.R., L. Gearheart, and C.J. Murphy, *Wet chemical synthesis of silver nanorods and nanowires of controllable aspect ratio*. Chemical Communications, 2001(7): p. 617-618.
199. Pavani, S.R.P., et al., *Three-dimensional, single-molecule fluorescence imaging beyond the diffraction limit by using a double-helix point spread function*. Proceedings of the National Academy of Sciences, 2009. **106**(9): p. 2995-2999.
200. Aguado, A., *3 - Modeling the electronic and geometric structure of nanoalloys*, in *Nanoalloys*, F. Calvo, Editor. 2013, Elsevier: Oxford. p. 75-111.
201. Negreiros, F.R., et al., *Structures of AgPd nanoclusters adsorbed on MgO(100): A computational study*. Surface Science, 2011. **605**(5-6): p. 483-488.
202. Lin, Y., et al., *Synthesis-Dependent Atomic Surface Structures of Oxide Nanoparticles*. Physical Review Letters, 2013. **111**(15): p. 156101.
203. Crosby, L.A., et al., *Complex surface structure of (110) terminated strontium titanate nanododecahedra*. Nanoscale, 2016. **8**(37): p. 16606-16611.
204. Lin, J., et al., *Remarkable Performance of Ir1/FeOx Single-Atom Catalyst in Water Gas Shift Reaction*. Journal of the American Chemical Society, 2013. **135**(41): p. 15314-15317.
205. Liu, S., et al., *Stabilizing Single-Atom and Small-Domain Platinum via Combining Organometallic Chemisorption and Atomic Layer Deposition*. Organometallics, 2017. **36**(4): p. 818-828.
206. Ding, K., et al., *Identification of active sites in CO oxidation and water-gas shift over supported Pt catalysts*. Science, 2015. **350**(6257): p. 189-192.

## Appendix A

### MATLAB Codes of Surface Area and Volume Calculations of Asymmetric Dh Particles

#### Surface area of asymmetric Dh particles:

```
function [SA_100_open,SA_100_closed,SA_111_open,SA_111_closed]=SA(L,h,a,b,c)
% SA calculates the surface area of an asymmetric Dh with re-entrant level
% a,b and c. c being on the same axis as the mirror plane
% detailed explanation goes here
SA_100_1=(L-2*a)*(h-L); % SA_100_1 calculates the surface area of 100 in
segment 1
SA_100_2=(L-a-b)*(h-L); % SA_100_2 calculates the surface area of 100 in
segment 2
SA_100_3=(L-b-c)*(h-L); % SA_100_3 calculates the surface area of 100 in
segment 3
SA_111_1_f=sqrt(3)/2*(L^2-2*a^2)+sqrt(3)/2*((h-L+a)^2-(h-L)^2); % SA_111_1_f
calculates the surface area of 111 in segment 1 when a<=0.5L
SA_111_1_h=sqrt(3)/2*(L^2-2*a^2+(2*a-L)^2)+sqrt(3)/2*((h-L+a)^2-(h+2*a-
2*L)^2); % SA_111_1_h calculates the surface area of 111 in segment 1 when
a>0.5L
SA_111_2_f=sqrt(3)/2*(L^2-a^2-b^2)+sqrt(3)/4*((h-L+a)^2-(h-
L)^2)+sqrt(3)/4*((h-L+b)^2-(h-L)^2); % SA_111_2_f calculates the surface area
of 111 in segment 2 when a+b<=L
SA_111_2_h=sqrt(3)/2*(L^2-a^2-b^2+(a+b-L)^2)+sqrt(3)/4*((h-L+a)^2-(h-L+a+b-
L)^2)+sqrt(3)/4*((h-L+b)^2-(h-L+a+b-L)^2); % SA_111_2_f calculates the
surface area of 111 in segment 2 when a+b>L
SA_111_3_f=sqrt(3)/2*(L^2-b^2-c^2)+sqrt(3)/4*((h-L+b)^2-(h-
L)^2)+sqrt(3)/4*((h-L+c)^2-(h-L)^2); % SA_111_2_f calculates the surface area
of 111 in segment 3 when b+c<=L
SA_111_3_h=sqrt(3)/2*(L^2-b^2-c^2+(b+c-L)^2)+sqrt(3)/4*((h-L+b)^2-(h-L+b+c-
L)^2)+sqrt(3)/4*((h-L+c)^2-(h-L+b+c-L)^2); % SA_111_2_f calculates the
surface area of 111 in segment 3 when b+c>L
if a+b<=L && b+c<=L && a<=0.5*L % no sharp tips
    SA_100_open=SA_100_1+2*SA_100_2+2*SA_100_3;
    SA_111_open=SA_111_1_f+2*SA_111_2_f+2*SA_111_3_f;
elseif a+b<=L && b+c<=L && a>0.5*L % 1 sharp tip at a
    SA_100_open=2*SA_100_2+2*SA_100_3;
    SA_111_open=SA_111_1_h+2*SA_111_2_f+2*SA_111_3_f;
elseif a+b<=L && b+c>L && a<=0.5*L % 2 sharp tips at b&c
    SA_100_open=SA_100_1+2*SA_100_2;
    SA_111_open=SA_111_1_f+2*SA_111_2_f+2*SA_111_3_h;
elseif a+b<=L && b+c>L && a>0.5*L % 3 sharp corners, 2 at b&c, 1 at a
    SA_100_open=2*SA_100_2;
    SA_111_open=SA_111_1_h+2*SA_111_2_f+2*SA_111_3_h;
elseif a+b>L && b+c<=L && a<=0.5*L % 2 sharp tips at a&b
    SA_100_open=SA_100_1+2*SA_100_3;
    SA_111_open=SA_111_1_f+2*SA_111_2_h+2*SA_111_3_f;
elseif a+b>L && b+c<=L && a>0.5*L % 3 sharp corners, 2 at a&b, 1 at a
    SA_100_open=2*SA_100_3;
    SA_111_open=SA_111_1_h+2*SA_111_2_h+2*SA_111_3_f;
elseif a+b>L && b+c>L && a<=0.5*L % 4 sharp tips at a&b and b&c
    SA_100_open=SA_100_1;
    SA_111_open=SA_111_1_f+2*SA_111_2_h+2*SA_111_3_h;
else % 5 sharp tips
```

```

    SA_100_open=0;
    SA_111_open=SA_111_1_h+2*SA_111_2_h+2*SA_111_3_h;
end
SA_100_closed=SA_100_open*360/(360-22/7);
SA_111_closed=SA_111_open*360/(360-22/7);
end

```

### Volume of asymmetric Dh particles:

```

function [Vol_open,Vol_closed] = Volume(L,h,a,b,c)
%Volume calculates the volume of an asymmetric Dh with re-entrant level a,
%b, and c. c being on the same axis as the mirror plane
% Detailed explanation goes here
V_total=5*L^3/(6*sqrt(2))+5*L^2*(h-L)/(2*sqrt(2)); % The volume of a
segment of an Ino Dh is the sum of a tetrahedron and a prism with height of
(h-L) and base area L^2/(2*sqrt(2))
V_1=a^3/(6*sqrt(2))+a^2*(h-L)/(2*sqrt(2));
V_2=b^3/(6*sqrt(2))+b^2*(h-L)/(2*sqrt(2));
V_3=c^3/(6*sqrt(2))+c^2*(h-L)/(2*sqrt(2));
V_4=(b+c-L)^3/(6*sqrt(2))+(b+c-L)^2*(h-L)/(2*sqrt(2));
V_5=(b+a-L)^3/(6*sqrt(2))+(b+a-L)^2*(h-L)/(2*sqrt(2));
V_6=(2*a-L)^3/(6*sqrt(2))+(2*a-L)^2*(h-L)/(2*sqrt(2));
if a+b<=L && b+c<=L && a<=0.5*L % no sharp tips
    Vol_open=V_total-4*V_1-4*V_2-2*V_3;
elseif a+b<=L && b+c<=L && a>0.5*L % 1 sharp tip at a
    Vol_open=V_total-4*V_1-4*V_2-2*V_3+V_6;
elseif a+b<=L && b+c>L && a<=0.5*L % 2 sharp tips at b&c
    Vol_open=V_total-4*V_1-4*V_2-2*V_3+2*V_4;
elseif a+b<=L && b+c>L && a>0.5*L % 3 sharp corners, 2 at b&c, 1 at a
    Vol_open=V_total-4*V_1-4*V_2-2*V_3+2*V_4+V_6;
elseif a+b>L && b+c<=L && a<=0.5*L % 2 sharp tips at a&b
    Vol_open=V_total-4*V_1-4*V_2-2*V_3+2*V_5;
elseif a+b>L && b+c<=L && a>0.5*L % 3 sharp corners, 2 at a&b, 1 at a
    Vol_open=V_total-4*V_1-4*V_2-2*V_3+2*V_5+V_6;
elseif a+b>L && b+c>L && a<=0.5*L % 4 sharp tips at a&b and b&c
    Vol_open=V_total-4*V_1-4*V_2-2*V_3+2*V_5+2*V_4;
else % 5 sharp tips
    Vol_open=V_total-4*V_1-4*V_2-2*V_3+2*V_5+2*V_4+V_6;
end
Vol_closed=Vol_open*360/(360-22/7);
end

```